INTEGRATION OF OPTIMIZATION ALGORITHMS WITH SENSITIVITY ANALYSIS, WITH APPLICATION TO VOLCANIC REGIONS

Vom Fachbereich Bauingenieurwesen und Geodäsie
der Technischen Universität Darmstadt
zur Erlangung des akademischen Grades eines
Doktor-Ingenieurs (Dr.-Ing.)
genehmigte Dissertation von

Dipl.-Ing. Carola Tiede
aus
Bad Hersfeld

Referent:	Prof. Dr.-Ing. Carl Gerstenecker
Korreferent:	Prof. Dr. Kristy Tiampo
Tag der Einreichung:	25.04.2005
Tag der mündlichen Prüfung:	03.06.2005

Darmstadt im April 2005
D 17

Abstract

The purpose of this thesis is the generation of improved optimization approaches, applied to a volcanic modeling.

Neither local nor global optimization algorithms can guarantee the generation of a global optimization solution. Furthermore, the generated models have to be integrated into the physical context of other available observations and models in the specific volcanic region. A reliable optimization result can only be given by a model with significant determined parameters which can be seen on small dispersion if the optimization is carried out several times as well as considering the results of statistical tests about the model fit. In addition, this model has to be validated by additional information from other observation techniques and models. Different improvements of the optimization have been analyzed within this thesis:

- The first approach is given by the definition of physical constraints, which are implemented into the optimization approach by penalty terms. This approach shall lead to a decrease of possible solutions so the dispersion of the unknown parameters is decreased, which is equal to an increase of significance of these parameters.
- Another improvement is given by the implementation of the results from a global sensitivity analysis. A re-weighting factor is implemented into the optimization approach, so the weight of the observations is varied with respect to their sensitivity against changes in a specific unknown parameter.
- Last improvement approach is implemented as a fuzzy logic model. This model fuses physical plausibility checks as well as available density data of the volcanic region. The fuzzy logic model results in a physical reliability value for the model. This approach is implemented actively into the optimization approach by an addend to the objective function.

The generated models without any implementation improvements serve as reference.

Data collected at the high risk volcano Merapi at Central Java, Indonesia serve as a case study. The modeling is based on a non-linear inversion of gravity changes and three-dimensional displacements which were measured between the years 2000 and 2002 at Merapi. The physical based mathematical model is described by the generalized static Navier equations which are solved for the mathematical half-space where elastic and gravitational effects are coupled. The parameters which have to be determined are given by the point mass of source, its position, and an energy value, described by the product of pressure and cubed radius.

The improvement approaches have been implemented into two different optimization algorithms: A downhill simplex and a genetic algorithm. The best optimization approach has been determined by comparing the different optimization configurations. The comparison results in the definition of a recommended optimization approach concerning the model's significance and physical reliability. The approach given by the implementation of the sensitivity analysis results into the genetic algorithm determines the best elastic-gravitational source model concerning the dispersion of the unknown parameters and the fitness value of the result.

Finally, the application of the fuzzy logic is used to validate these results with respect to the physical reliability of the elastic-gravitational source's position. So the quality of the model can be described statistically as well as physically.

Nevertheless, all optimization configurations showed that a model which is solely based on a magmatic source is not feasible. All optimization results showed very shallow sources with small mass components and large energy values. These properties as well as the lack of ability to model the deformations lead to the assumption that another influence is acting. This effect is modelled by superposition of a local fault zone to the assumed magmatic source.

This final model results in statistical significant and physical reliable parameters for a volcanic source superimposed with the effects of a fault zone. The model is statistically significant with a larger significance level than the models which are based on a solely elastic-gravitational source. In addition, this combined model also fits into the prior anticipations about the structure of Merapi given in the literature.

Zusammenfassung

Das Ziel der vorliegenden Arbeit besteht in der Generierung von verbesserten Optimierungsansätzen, die im Rahmen vulkanologischer Studien benutzt werden.

Weder lokale noch globale Optimierungsverfahren können das Auffinden der globalen Lösung eines Optimierungsproblemes garantieren. Weiterhin müssen Modelle physikalischen Randbedingungen genügen sowie in den physikalischen Kontext anderer Messverfahren und die daraus resultierenden Modellierungen gebracht werden. Erst ein Modell, dessen Modellparameter statistisch signifikant bestimmt werden konnten, sowie die Validierung dieses Modelles durch Ergebnisse anderer Messverfahren, führt zu einem vertrauenswürdigen Optimierungsresultat. Es werden drei Verbesserungsansätze der Optimierung untersucht:

- Der erste Ansatz wird durch die Definition physikalischer Bedingungen beschrieben, die durch penalty Terme in die Optimierungen einfliessen. Dieser Ansatz hat zum Ziel, den Lösungsraum einzuschränken und somit die Signifikanz einzelner Unbekannten zu steigern.
- Mittels einer globalen Sensitivitätsanalyse werden die Beobachtungen regewichtet. Hierbei wird ein Regewichtungsansatz verfolgt, mit Hilfe dessen die Gewichtung von Beobachtungen in Abhängigkeit ihrer Sensitivität auf Änderungen eines unbekannten Parameters variiert wird.
- In einem letzten Ansatz wird ein Fuzzy Logic Regler entworfen. Dieser fusioniert physikalische Plausibilitätstests mit Dichtedaten, die für das Untersuchungsgebiet zur Verfügung stehen und liefert ein physikalisches Vertrautheitsmass für das Modell. Dieser Ansatz wird aktiv als Additionsterm in die zu maximierende Zielfunktion eingefügt.

Die Modelle, die mit dem Optimierungsalgorithmus ohne jegliche Implementation von Verbesserungen generiert worden sind, werden als Referenzergebnisse genutzt. Als Anwendungsfall dient der Hochrisikovulkan Merapi auf Java, Indonesien. Die Modellierung gründet sich hierbei auf die nicht lineare Inversion von Schwereänderungen sowie dreidimensionalen Deformationen, die zwischen den Jahren 2000 und 2002 gemessen worden sind. Das zugrundeliegende mathematische Modell basiert auf den generalisierten, statischen Navier Gleichungen, die für den mathematischen Halbraum gelöst sind und Elastizitäts- und Gravitationseffekte koppeln. Die zu modellierenden Parameter der Quelle sind durch Punktmasse, dessen Position sowie einer Energieform gegeben.

Die verschiedenen Ansätze werden in einen downhill simplex und einem genetischen Algorithmus implementiert und bezüglich der Streuung und des physikalischen Vertrautheitsmasses der Ergebnisse getestet. Die beste Konfiguration wird durch den Einsatz des genetischen Algorithmus mit der Implementation der Resultate, die aus der globalen Sensitivitätsanalyse gewonnen wurden, erreicht. Die Ergebnisse werden letztendlich durch den Fuzzy Logic Regler mit einem physikalischen Vertrautheitsmass versehen, so dass die Qualität der Ergebnisse sowohl statistisch als auch physikalisch definiert ist.

Optimierungsansätze, die nur eine magmatische Quelle betrachten, lieferten für den Vulkan Merapi keine plausiblen Ergebnisse. Die Teststatitik zeigte, dass diese Modelle zwar statistisch signifikant sind, jedoch die Modellanpassung an die Daten sehr gering ist. Alle Ansätze zeigten oberflächennahe Quellen mit sehr kleinen Massen jedoch zu grossen Energiewerten. Diese Eigenschaften und die schlechte Modellierbarkeit der Deformationen durch das physikalische Modell lassen einen weiteren Einfluss vermuten, der hauptverantwortlich für die grossen Deformationen, vor allem im Kraterbereich, ist. Dieser Einfluss wird durch Superposition einer Störzone und dem elastisch-gravitativen Modell erfasst.

Die entgültige Modellierung liefert statistisch signifikante und physikalisch plausible Ergebnisse. Verglichen mit den Modellierungen, die sich einzig auf eine elastisch-gravitative Quelle stützen, zeichnet sich dieses Modell durch eine höhere statistische Signifikanz aus und ist konform zu publizierten Annahmen über die Struktur des Merapis im Kraterbereich.

Contents

List of Figures

List of Tables

SHORTCUTS AND ACRONYMS

BCFAG	Bouguer Corrected Free Air Gradient
DC	Direct Current
DFG	Deutsche Forschungsgemeinschaft
EGM96	Earth Gravitational Model, 1996
FAG	Free Air Gradient
FAST	Fourier Amplitude Sensitivity Test
GA	Genetic Algorithm
GFZ	Geoforschungszentrum Potsdam
GLUE	Generalized Likelihood Uncertainty Estimation
GPS	Global Positioning System
IAVCEI	International Association of Volcanology and Chemistry of the Earth's Interior
IDNDR	International Decade for Natural Disaster Reduction Program
IGS	International GPS System
ITRF2000	International Terrestric Reference Frame, 2000
LOTEM	Long Offset Transient Electromagnetics
MERAPI	Mechanism Evaluation, Risk Assessment, Prediction Improvement
MISO	Multiple-Input, Single-Output system
MF	Membership Function
MVO	Merapi Volcano Observatory
NanoTEM	Nano Transient Electromagnetics
NE	North-East
NW	North-West
OAT	One-at-a-time
pdf	Probability density function
rms	Root mean square
RSA	Regionalized Sensitivity Analysis
SA	Sensitivity Analysis
SE	South-East
SW	South-West
smf	S-shape membership function
TSI	Total Sensitivity Index
USGS	US Geological Survey
UTM	Universal Transverse Mercator projection
VSI	Volcanological Survey of Indonesia
WGS84	World Geodetic System, 1984
zmf	Z-shape membership function

SCALARS

D	Distance between X_1 axis and end of dip-slip/strike-slip fault
d	Distance between X_1 axis and beginning of dip-slip/strike-slip fault
dg	Gravity change [mGal]
E	Mathematical expectation
E	Young modulus
G	Gravitational constant, $6.67422 \cdot 10^{-11} \frac{m^3}{kg \cdot sec^2}$
h	ellipsoidal height
k	Fourier wave number
L	L-norm describing the metric of solution space in optimization

L	Semi length of strike-slip/dip-slip fault model
m	Mass of the elastic-gravitational source in $[10^{12}kg]$
n	Number of observations
P_1	Point with the highest function value (downhill simplex)
P_2	Point with the second highest function value (downhill simplex)
P_c	Centroid point computed (downhill simplex)
P_C	Contracted point (downhill simplex)
P_E	Expanded point (downhill simplex)
P_I	Contracted point around the low vertex (downhill simplex)
P_L	Point with the lowest function value (downhill simplex)
P_R	Reflected point (downhill simplex)
p	Pressure of the elastic-gravitational source $[10^5 Pa]$
$q_0^1(0)$	kernel function (elastic-gravitational model)
r	Radius of the elastic-gravitational source $[10^3 m]$
r	Degrees of freedom
r_1	Radius of the cylindrical polar coordinate system (elastic-gravitational model)
$S()_i$	First order index of the values given in brackets, concerning changes in the unknown parameter i, given in the subfix
$S()_{n,i}$	Normalized first order index of the values given in brackets, concerning changes in the unknown parameter i, given in the subfix
$TSI()_i$	Total sensitivity index of the values given in brackets, concerning changes in the unknown parameter i, given in the subfix
$TSI()_{n,i}$	Normalized total sensitivity index of the values given in brackets, concerning changes in the unknown parameter i, given in the subfix
U_2	Dip slip of U down fault slip (dip-slip/strike-slip model)
U_1	Magnitude of strike slip in X_1-direction (dip-slip/strike-slip model)
u	Number of unknown parameters
ux	Horizontal displacement in east direction [cm]
uy	Horizontal displacement in north direction [cm]
uz	Vertical displacement [cm]
V	Physical reliability value (output of fuzzy logic model)
x	Coordinate measured positive downwards the fault dip (dip-slip/strike-slip model)
$x_0^1(0)$	kernel function (elastic-gravitational model)
x_1	Density value (input of fuzzy logic model)
x_2	Depth value (input of fuzzy logic model)
x_3	Distance to top value (input of fuzzy logic model)
$y_0^1(0)$	kernel function (elastic-gravitational model)

$p \cdot r^3$	Product of pressure and cubed radius of the elastic-gravitational source model $[kg \cdot m^2/sec^2]$

$1/\chi(comp)^2$	Objective function, taking all kind of changes into account
$1/\chi(dg)^2$	Objective function, taking gravity changes dg into account
$1/\chi(ux)^2$	Objective function, taking east displacements ux into account
$1/\chi(uy)^2$	Objective function, taking north displacements uy into account
$1/\chi(uz)^2$	Objective function, taking height displacements uz into account

α	Significance level of statistical tests (probability to commit error of first kind)
β_1	One-dimensional contraction factor (downhill simplex)
β_2	Full contraction factor (downhill simplex)
γ	Expansion factor (downhill simplex)
Δm	Anomalous mass [kg]
δ	Reflection factor (downhill simplex)
λ	Lame parameter

λ	Geographical longitude
ν	Poisson ratio
μ	Lame parameter
ρ	Undisturbed density
σ	standard deviation
θ	Dip angle (dip-slip/strike-slip model)
Φ	Perturbation potential
ϕ	Geographical latitude
ξ	East coordinate of the elastic-gravitational source $[10^3 m]$
ψ	North coordinate of the elastic-gravitational source $[10^3 m]$
ζ	Depth of the elastic-gravitational source $[10^3 m]$

VECTORS AND MATRICES

$\mathbf{b_0}$	Vector given in terms of Bessel function (elastic-gravitational model)
$\mathbf{c_i}$	Vector of unknown parameter i (sample set)
$\mathbf{d}$	Jump discontinuity vector (elastic-gravitational model)
$\mathbf{f}$	Product of layer matrices and **d** (elastic-gravitational model)
$\mathbf{e}$	Unit vector
$\mathbf{l}$	Vector of observed values
$\mathbf{p_0}$	Vector given in terms of Bessel function (elastic-gravitational model)
S1	First sample set for the regionalized sensitivity analysis
S2	Second sample set for the regionalized sensitivity analysis
S3	Third sample set for the regionalized sensitivity analysis
$\mathbf{u}$	vector of displacements
u1	Three dimensional displacements of strike-slip fault
u2	Three dimensional displacements of dip-slip fault
$\mathbf{v}$	Vector of residuals between observed and modeled values
$\mathbf{x}$	Three dimensional coordinates of point force with unit magnitude of dip-slip/strike-slip model
$\mathbf{E}$	Matrix including characteristics of layer medium
$\mathbf{Q_{ll}}$	Cofactor matrix of **l** with **l** as observations
$\mathbf{Q_{ll}}(\mathbf{r})$	Re-weighted cofactor matrix concerning the radius

UNITS

mGal	1 mGal = 1000 $\mu gal = 1 \cdot 10^{-5} m/s^2$
km	1 km = 1000 m

Acknowledgements

This thesis was carried out at the Department of Physical Geodesy, Darmstadt University of Technology and at University of Western Ontario, London, Canada. There are many people I would like to thank for a huge variety of reasons.

Firstly, I would like to thank my supervisor, Prof. Dr. Carl Gerstenecker. He always tried to make everything possible and could give me always practical advice concerning the arrangements of the dissertation. His knowledge, common-sense, perceptiveness and ideas helped me to finish this sometimes endless seeming thesis. Thank you a lot for the permission to study a certain time in Madrid as well as the time in Canada. I really could not have imagined to have a better advisor and mentor for my thesis.

I want to thank Prof. Dr. Kristy Tiampo who invited me to University of Western Ontario, Canada in order to work with her at the inversion via genetic algorithms. Her friendly comments and constructive criticism on my work as well as many noteworthy and fascinating ideas for further research subjects were invaluable. Beside this I spent a perfect time in London and will never forget her great help and hospitality.

Great thanks to Pepe (Prof. Dr. José Fernández) for all his help during the last years. He gave me a lot of new ideas and encouraged me to work on the topic of elastic-gravitational modeling. Especially the time which we could work together in Madrid at University of Mathematics and Sciences as well as various workshops have been great and very productive. Thank you a lot for proof-reading of this thesis.

Thanks to all my friends in Germany, Canada and Spain, for their support in difficult moments. I want to thank especially Astrid for all the time which she spent with listening to occuring problems during my thesis.

Thanks to Daniel, for all the help during the thesis, for his patience and his belief in finishing the thesis.

Finally, thanks to my parents for their understanding, endless patience and encouragement.

Chapter 1

Introduction

1.1 Motivation

The determination of model parameters from observed data is known as an indirect problem. The solution for the indirect problem is determined by inversion of the observed data, anticipating a certain mathematical model. The objective function which has to be optimized in an inversion problem is based on a certain L-norm minimizing the residuals between observed and modeled values. If the underlying model has a non-linear characteristic and the objective function is multimodal, a global optimization approach becomes indispensable. By applying local optimization approaches in such cases will only lead to local solutions.

Nevertheless, no optimization approach, neither local, nor global ones, can guarantee to find the global optimum for sure. Furthermore, due to small sensitivities of the observed data concerning changes in certain unknown parameters, these parameters can be determined with a large dispersion only. Another problem which occurs in physical applications is that the optimal solution might be not reliable physically. To proof the physical reliability of a model, further observation and modeling results can help to qualify the optimization's result.

The application of an optimization without integrating the results in existing modelings or without testing the model with physical plausibility checks can lead to a completely wrong result. Also the computation of an optimization without any knowledge about the sensitivities of the observed data concerning changes in the unknown parameters can lead to unstable, insignificant results.

This thesis is dealing with different improvement approaches of optimization algorithms, applied to a volcanic modeling. The aim is given by the determination of a statistically significant model which is physically feasible and can be integrated into former modeling approaches. Furthermore, improvement approaches are investigated in order to determine the unknown parameters with only small dispersions which is equivalent to the determination of significant and reliable unknown parameters within a statistically proven model.

The permanent active volcano Merapi in Indonesia serves as an application case. Till now, the structure of this volcano is only partly known. Especially the location of a potential magma chamber is very vague but of great interest for hazard mitigation and eruption prediction.

In this thesis the determination of statistically significant and physical reliable model parameters of a volcanic source leads to an improvement of understanding the permanent active volcano Merapi.

1.2 Structure of Thesis

The thesis is structured into six Chapters:

1. Chapter 2 describes the underlying physical based mathematical models. The elastic-gravitational modeling of a point source with an energy value described by the product of pressure and cubed radius as well as the modeling of a combined strike-slip/dip-slip fault is introduced. Both models are computed in a mathematical half-space.

2. Chapter 3 describes, in general, optimization algorithms, concentrated on the two applied approaches: A downhill simplex and a genetic algorithm.

3. Chapter 4 deals with the theory of uncertainty and sensitivity analyses with a main focus on the applied Sobol' sensitivity analysis and the regionalized sensitivity analysis.

4. In Chapter 5 three different aproaches are described to improve optimization algorithms.

    - The first improvement approach consists of physical constraints between the unknown parameters which are added into the optimization as penalty terms.
    - The second improvement approach is described by the implementation of the results from the Sobol' sensitivity analysis described in Chapter 4.
    - The third improvement attempt is investigated by the development of a fuzzy logic controller. Plausibility checks as well as additional available data from the region of interest are fused within the fuzzy logic. The output of the fuzzy logic controller is defined by a physical reliability value of the underlying source model's position.

5. Chapter 6 is focusing on the application of the described techniques. The optimization approaches are applied to Merapi volcano, a continuously active andesitic stratovolcano at Central Java, Indonesia. It belongs, due to its densely populated surrounding area, in the category of the most hazardous volcanoes worldwide. A detailed overview about the region of study as well as measurements, modeling and interpretation results which are of interest for this thesis are given. Sobol' and a regionalized sensitivity analysis are applied according to Chapter 4 to the observed data and lead to precise knowledge about the behavior of the system, given by the observed data, the underlying elastic-gravitational model, described in Chapter 2 and the unknown input parameters which are defined in certain ranges. In the next step, the application and results of the optimization algorithms and the optimization with implied improvement approaches from Chapter 5 are described. All approaches are compared and analyzed. They result in a recommended optimization approach for the observed data and the underlying elastic-gravitational model. Finally, a more complex model is computed which consists of a combined strike slip/dip-slip fault which is added by linear superposition to the elastic-gravitational model.

6. Chapter 7 draws out the main studied aspects of the thesis as well as its benefit for further research.

Chapter 2

Modeling

This Chapter consists of a short description of the applied modeling approaches: The first model is based on an elastic-gravitational source. The aim of this model is to localize a potential magmatic chamber. The second approach is given by a fault model whose effects are superposed to the first model in order to get a better fit between observed data and model. Different analyses of input data allow the choice of the applied modeling approach. These analyses are summarized in the following list:

- The volcano under investigation is permanently active. A dome is formed of highly viscous magma. The magma has to originate from a magma chamber below the volcano and should cause significant observed gravity changes and deformations. The observations show significant changes in the summit region, both in gravity and position.
- The significance of analysed data is decreasing with increasing distance to the summit of the volcano. At the top of the volcano, significant gravity changes and deformations (horizontal as well as vertical) are observed. This leads to the assumption that a local effect has to be modeled. The effect can be modeled by a chamber with a certain energy and mass or a fracture zone which is causing the measured changes.
- Significant deformations are only in some cases accompanied by significant gravity changes and vice versa. A correlation between deformation and gravity change cannot be found in all observation points.

Due to the fact that the knowledge of the position as well as mass and energy term of a magmatic source is of great interest for hazard mitigation, this study focuses on the modeling of a magmatic source.

The basic model for the computation of volcanic loading is given by MOGI (1958). In his model pressurization creating ground inflation/deflation could be attributed to injected mass in the chamber cavity which is embedded in an elastic homogeneous and isotropic half-space. The measured gravity changes are therefore modeled due to uplift. Although this model can explain measured deformation in many volcanic applications, the model involves difficulties in modeling horizontal displacements and gravity changes, RYMER (1994). Furthermore, this approach seems to be too simple due to its difference to the real geology of volcanic regions, since the crust is not homogeneous and magma chambers also cannot be anticipated as spheres, BATTAGLIA and SEGALL (2004). A variety of other models have been derived, e.g. MCTIGUE (1987) for a spherical or DAVIS (1986) for an ellipsoidal body.

In many cases the elastic models are unable to reproduce the observed uplifts without anticipating an unrealistic overpressure. Furthermore, they are unable to explain observed gravity changes as well as corresponding deformations, Berrino *et al.* (1984), Jentzsch *et al.* (2001).

In Rundle (1980) and Rundle (1982) self-gravitation effects are taken into account in an elastic-gravitational model that considers a stratified half-space of homogeneous layers. It has been shown that considering the self-gravitation of the medium can be fundamental for the interpretation and explanation of gravity changes which are measured in active volcanoes (e.g. Fernández *et al.* (1997), Fernández *et al.* (2001a), Fernández *et al.* (2001b)). Furthermore, according to Fernández *et al.* (1997), Bonafede and Mazzanti (1998) vertical discontinuities in the earth's density and elastic parameters can play an important role when modeling gravity changes induced by deformation which is one reason for anticipating a layered medium with different elastic parameters. This model showed in various applications good results for the modeling of volcanic sources. Examples for model applications are given for Mayon, Philippines, Fernández *et al.* (2001b), Tiampo *et al.* (2004b), Lanzarote, Canary islands, Fernández and Rundle (1994), Long Valley Caldera, California, Fernández *et al.* (2001a), Charco *et al.* (2004) or for Campi Flegrei in Italy, Fernández *et al.* (2001c).

In contrary, Battaglia and Segall (2004) could only find minor differences between the model which is based on a point source in an elastic homogeneous half-space compared to a point source in an elastic-gravitational, layered half-space. They also showed that self-gravitation effects are second order over the distance and time scales normally associated with volcano monitoring.

Nevertheless, the main advantage in using the full elastic-gravitational model according to Rundle (1980), Rundle (1982) is that it gives accurate results for all elastic structures as described in Charco *et al.* (2004). Furthermore, the model is very useful for the interpretation of all combinations of gravity change and deformation so that also significant gravity changes without any corresponding deformation or vice versa can be modeled, Fernández *et al.* (2001c).

Due to the reason that on the one hand the gravity changes are in some points accompanied by significant deformation and on the other hand there are also gravity changes without any deformation, an elastic-gravitational modeling is applied and shortly introduced in Chapter 2.1.

2.1 Elastic-Gravitational Modeling

The generalized static Navier equations couple elastic and gravitational effects. They are satisfied by the three-dimensional displacement vector **u**=(ux,uy,uz) and the perturbation potential ϕ, both produced by an magmatic intrusion in an elastic, self-gravitating uniform, infinite medium, Love (1911),

$$0 = \nabla^2\mathbf{u} + \frac{1}{1-2\nu}\nabla\nabla\cdot\mathbf{u} + \frac{\rho_0 g}{\mu}\nabla(\boldsymbol{u}\cdot\mathbf{e}_z) - \frac{\rho_0}{\mu}\nabla\phi - \frac{\rho_0 g}{\mu}\mathbf{e}_z\nabla\cdot\mathbf{u} \tag{2.1}$$

$$\nabla^2\phi = 4\pi\rho_0 G\nabla\cdot\mathbf{u} \tag{2.2}$$

g = unperturbed surface gravity, $\nu = \frac{\lambda}{2(\mu+\lambda)}$ = Poisson ratio with λ, μ =Lamé parameters, ρ_0 = undisturbed density, G = gravitational constant, **e** = unit vector. The displacement and perturbation potential which satisfy Equation 2.1 and Equation 2.2 for a layered, homogeneous half-space are solved by Rundle (1980), RUNDLE (1982), FERNÁNDEZ and RUNDLE (2004) and leads at $z = 0$ to

$$\mathbf{u} = \quad m \int_0^\infty [x_0^1(0)\mathbf{p}_0 + y_0^1(0)\mathbf{b}_0] k dk \tag{2.3}$$

$$dg = \frac{d\phi}{dz} = \quad m \int_0^\infty q_0^1(0) J_0(kr_1) k dk + 4\pi G \rho_0 uz \tag{2.4}$$

where m = mass of the magmatic point source, $\mathbf{p_0}, \mathbf{b_0}$ = vectors given in terms of Bessel function $J_0(kr)$ of the first kind of order zero with r_1 = radius of the cylindrical polar coordinate system, ρ_0 = density of the layer, $x_0^1(0)$, $y_0^1(0)$, $q_0^1(0)$ = kernel functions, depending on Fourier wave number k and given as a function of the characteristics of the mediums's layers, FERNÁNDEZ and RUNDLE (1994). They consist of two terms, first a matrix $\mathbf{E}$ (dimension 6x6) which includes the characteristics of the layer medium and second, a vector $\mathbf{f}$ (dimension 6x1)which shows the product of layer matrices with the jump discontinuity vector $\mathbf{d}$ (dimension 6x1), described in RUNDLE (1980).

For a magmatic intrusion which is considered as a point mass m at a depth ζ, the jump discontinuities result from the interaction between the mass m and the ambient gravity field

$$d_3 = \frac{-m \cdot g}{4\pi k} \tag{2.5}$$

$$d_6 = 2G \cdot m \tag{2.6}$$

and effects caused by the pressurization of the magmatic chamber due to overfilling or temperature changes.

$$d_1 = \frac{2p \cdot r^3 (1-\sigma)\delta}{\mu(1+\delta)} \tag{2.7}$$

$$d_4 = \frac{2p \cdot r^3 (1-\sigma)\delta}{1+\delta} \tag{2.8}$$

and $d_2 = d_5 = 0$ with p = pressure of the chamber, r = radius of the chamber and $\delta = 1/(3-4\nu)$. Note: The product $p \cdot r^3$ has the dimension of work (energy) [kg$\cdot$ m^2/sec^2]. The model is computed with the program GRAVW, FERNÁNDEZ *et al.* (1997). Figure 2.1 describes the model, whereby the unknown input parameters are given by

- ξ - East coordinate of intrusion $[10^3 m]$
- ψ - North coordinate of intrusion $[10^3 m]$
- ζ - Depth of intrusion $[10^3 m]$
- p - Pressure of intrusion $[10^5 Pa]$
- r - Radius of intrusion $[10^3 m]$
- m - Mass of intrusion $[10^{12} kg]$

The values to be modeled are given by

- dg - gravity change [mGal]
- ux - displacement in east direction [cm]
- uy - displacement in north direction [cm]
- uz - displacement in vertical direction [cm], positive definition for increasing depth

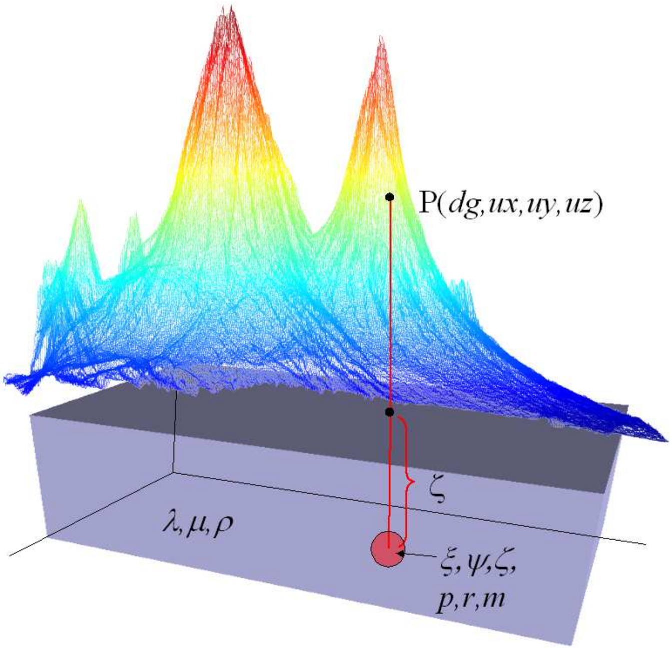

Figure 2.1: Elastic-gravitational model.

2.2 Strike-Slip and Dip-Slip Fault Modeling

Faults differ in the following way: Strike-slip faults are characterized by a horizontal movement of the blocks along the fault. This movement is caused by shearing forces. Dip-slip faults are inclined fractures where the blocks shift vertically. If the rock mass above an inclined fault moves down, the fault is termed normal, whereas if the rock above the fault moves up, the fault is termed reverse. A thrust fault is a reverse fault with a dip angle of 45°or less.

Mansinha *et al.* (1971) computed the displacements according to strike-slip and dip-slip faults. They derived the closed analytical expressions for the displacement fields. The expressions are derived from Volterra's formula, which describe the displacement field produced by a dislocation across a surface in a uniform elastic half-space.

The displacements $u1_i$, $i = 1...3$ resulting from a strike-slip fault (slip of magnitude U_1 in X_1-direction) fault are given by

$$u1_i = \mu U_1 \int_d^D \int_{-L}^L [(\frac{\partial u1_i^1}{\partial x_2} + \frac{\partial u1_i^2}{\partial x_1}) sin(\theta) - (\frac{\partial u1_i^1}{\partial x_3} + \frac{\partial u1_i^3}{\partial x_1}) cos(\theta)] dx_1 dx \qquad (2.9)$$

with $-L \leq x_1 \leq L$ and $d \leq x \leq D$, μ = Lamé parameter, θ = dip angle, x = coordinate measured positive downwards the fault dip, (see Figure 2.2), $u1_i^j$ as i-th component of the displacement at (X_1, X_2, X_3) due to a point force with unit magnitude at (x_1, x_2, x_3) acting in the j-th direction.

Effects $u2_i$ resulting from a dip-slip fault (slip of U_2 down fault slip) are described by

$$u2_i = \mu U_2 \int_d^D \int_{-L}^L [2(\frac{\partial u2_i^2}{\partial x} sin(\theta) - \frac{\partial u2_i^3}{\partial x} cos(\theta)) + \frac{\partial u2_i^3}{\partial x_2} - \frac{\partial u2_i^2}{\partial x_3}] dx_1 dx \qquad (2.10)$$

The gravity changes caused by the faults are anticipated by free air gradients. In

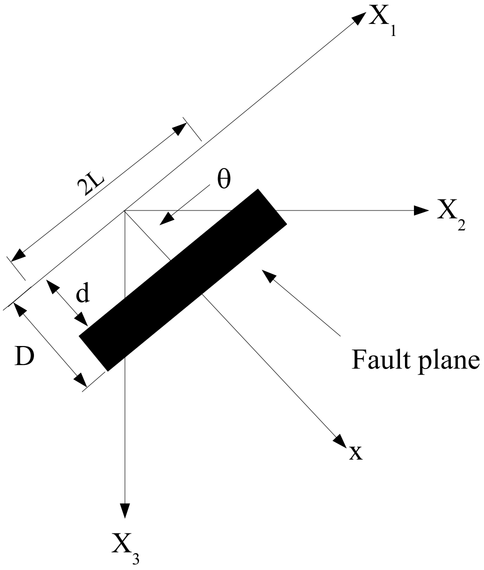

Figure 2.2: Fault geometry.

the modeling both effects are superimposed and result in the modeled displacements in east ux, north uy, height uz as well as in the modeled gravity change dg:

$$\begin{aligned} ux &= u_1 = u1_1 + u2_1 \\ uy &= u_2 = u1_2 + u2_2 \\ uz &= u_3 = u1_3 + u2_3 \\ dg &= (u1_3 + u2_3) \cdot 0.30877 \cdot (1 - 0.00142 \cdot sin^2\varphi) \end{aligned} \tag{2.11}$$

with φ = geographical latitude of the observation point in degree. For the modeling the unknown input parameters for the combined strike-slip/dip-slip fault are given by

- (1) - East coordinate of midpoint [m]
- (2) - North coordinate of midpoint [m]
- (3) - Dip slip [m]
- (4) - Semi length [m]
- (5) - Maximum depth from the top [m]
- (6) - Dip angle [rad]
- (7) - Strike angle [rad]
- (8) - Strike slip [m]

Chapter 3

Optimization

Optimization can be defined as the process of trying to find the best possible solution to an optimization problem within a given time limit, PRICE (1999), whereby all possible solutions are accompanied by a clear quality definition.

Generally optimization algorithms can be divided into two different classes depending on the number of minima which an objective function has. Hereby, every objective function maps an u-dimensional hyperplane into an one-dimensional area with u = number of unknown parameters. For every vector of unknowns, a function value of the objective function can be computed which is called fitness or quality of unknowns and describes the quality of the model fit to the observed data. Objective functions can be distinguished according to their number of optima, see Figure 3.1:

- If there exists only one optimum, the local and global optimum becomes the same. In this case the objective function is called unimodal.
- Multimodal objective functions consist of a number of local optima where one of them is also the global one.

A multimodal objective function makes the use of global optimization tools indispensable, whereby global optimization tools always contain of a probabilistic mechanism (MAUTZ (2001)) so that the possibility is given, to leave a reached local optimum in order to find the global one. Nevertheless, generally there is no guarantee that the global optimum is always reached by any optimization.

Generally all optimization approaches should focus on the minimization of the residuals v_i between the observed and the modeled values. Therefore, different norm parameters are defined, describing the metric of the given solution space. They can be written as

$$L \equiv f(v_i) \longrightarrow min \tag{3.1}$$

whereby the value of the objective function to be maximized (equivalent to the fitness of the function), is given by $1/L$. The most common norm values are

$$L_\infty - Norm \equiv |v_{max}| \longrightarrow min \tag{3.2}$$

which minimizes the absolute value of the maximal residual v_{max},

$$L_1 - Norm \equiv \sum_{i=1}^{n} |v_i| \longrightarrow min \tag{3.3}$$

which minimizes the sum of the absolute values of v_i, so it is robust concerning outliers in a data set. The norm on which most optimization strategies are based,

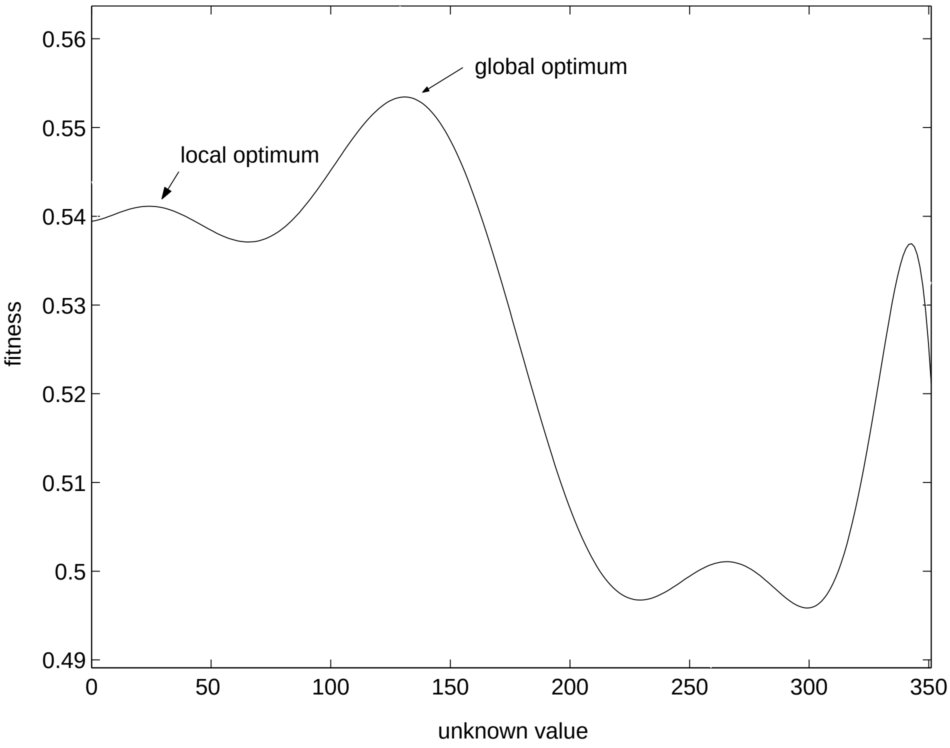

Figure 3.1: Local and global optimum of an objective function.

is

$$L_2 - Norm \equiv \sqrt{\sum_{i=1}^{n} v_i^2} \longrightarrow min \tag{3.4}$$

which minimizes the sum of squared v_i. Beside this, also fractal norms exist which are used in multidimensional spaces, Aggarwal *et al.* (2001). Figure (3.2) gives an overview about the different kind of norms and their objective functions concerning the computation of a mean value of the input values given by $\mathbf{x} = (1, 1, 2, 4)$. The fractal norm is given by LFrac, L_∞ by LInf. The choice of the appropriate norm is related to the task of its application and the dimension of the space (e.g. robust modeling which is insensitive against outliers in the data or application in multidimensional spaces). In this study the L_2-norm is used and the objective function $1/\chi()^2$ is given as,

$$1/\chi(comp)^2 = \frac{n-u}{\mathbf{v}^T \mathbf{Q_{ll}}^{-1} \mathbf{v}} \tag{3.5}$$

with $n - u$ = degrees of freedom (n = number of observations, u = number of unknown parameters), $\mathbf{v}$ = residuals, defined between all observed and modeled values, specified by (*comp*), $\mathbf{Q_{ll}}$ = cofactor matrix, with the variances of each observation on its diagonal, anticipating uncorrelated data. (Note: Usually geodetic data like they are used in the thesis are correlated. The correlation of the observed values results of the common adjustment but is neglected in the thesis.)

For the computation of uncertainty and sensitivity analysis, Chapter 6.3, the objective functions $1/\chi(dg)^2$ (concerning observed gravity changes), $1/\chi(uz)^2$ (concerning observed height changes), $1/\chi(ux)^2$ (concerning observed changes in east)

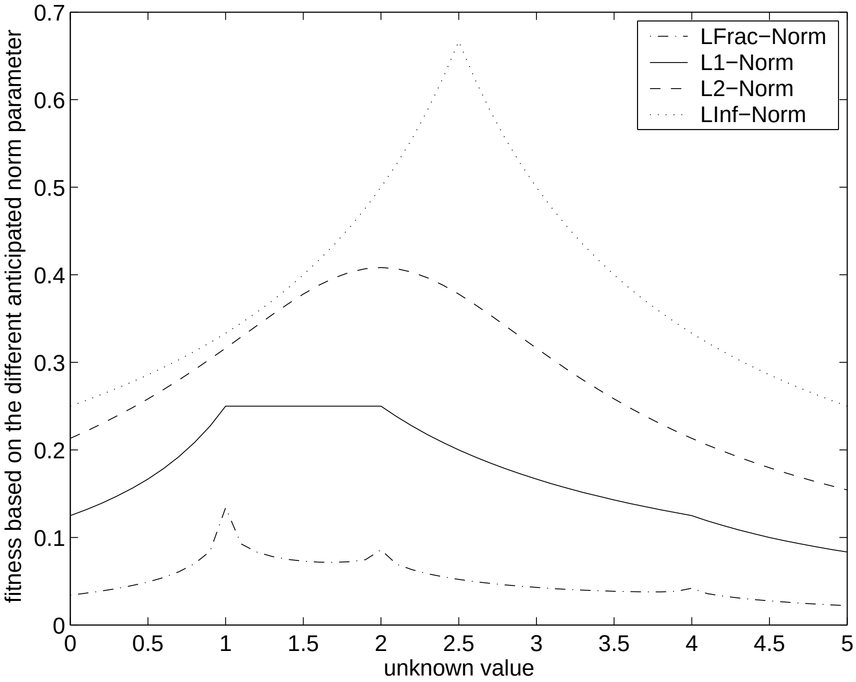

Figure 3.2: Objective functions resulting of the computation of the mean of $\mathbf{x}$=(1,1,2,4).

and $1/\chi(uy)^2$ (concerning observed changes in the north) are defined. These values are computed with respect to the kind of observation given in brackets.

The choice of the optimization algorithm is highly dependent on certain model characteristics. Generally, problem specific heuristics are the first choice in a difficult optimization task and show superior performance by implying expert knowledge compared with evolutionary processes like genetic algorithms, Price (1999). If the objective function is linear, polynomial efficient methods provide good solutions. If the objective function is non-linear but differentiable, gradient based methods can be used. If the derivatives of the objective functions cannot be computed, direct search methods which do not use any derivatives like the downhill simplex algorithm can be applied and can provide good solutions. All these mentioned approaches only determine a local optimum. Multimodality, non-linearity, non-differentiability of the objective function, noise, high-dimensionality, parameter interactions, constraints and the flatness of the objective function are reasons why all the mentioned algorithms can fail, Price (1999). Evolutionary processes as one kind of global optimization approaches have the appeal that they can cope with many of these problems.

The common inversion of gravity changes and displacements is a problem with a non-linear characteristic. The underlying physical based mathematical model which is based on the generalized static Navier equations, Chapter 2.1, shows a non-differentiability, possible parameter interactions, noise and a multimodal objective function, so the application makes the use of a global optimization approach and an independence of differentiability indispensable. Therefore, this study concentrates on two different approaches: The first one reflects the (normally) local downhill simplex approach which is working with the direct function values. This algorithm is restarted several times with randomly generated initial values, so a probabilistic part is added to the algorithm in order to increase the possibility to run into the global optimum. The second approach is based on the globally operating genetic algorithm.

These two applied algorithms are described in detail in Chapter 3.1.1, Chapter 3.2.1 respectively, whereby other global and local methods are referred to in literature, e.g. TARANTOLA (1987), GRAY *et al.* (1997), MAUTZ (2001) or PRESS *et al.* (2002).

3.1 Local Optimization

Local optimization methods use local information, such as gradients and Hessian matrices, to generate iterative points and attempt to locate a local optimum of the objective function. They cannot guarantee to find the global optimum because the solution depends strongly on the initial values of the unknown input parameters. Examples for local optimization methods are given by gradient methods like steepest descent, Newton-Raphson or Gauss-Newton which depend on the existence of the derivative and numerical approximations of the derivative, and by direct optimization approaches.

3.1.1 Downhill Simplex

The downhill simplex algorithm according to NELDER and MEAD (1965) is a multidimensional direct optimization algorithm which only requires the function values and not its derivatives. Therefore it can be easily applied to the non-linear model which is given in this thesis.

The purpose of the downhill simplex method is the minimization of the volume of a simplex, which is a geometrical construct, consisting of u+1 points in an u-dimensional space, with u = number of unknown input parameters. The selection of points can be specified or set randomly, allowing a better search in the whole space. The simplex is created by one point defining the origin and another u points, that define the vector directions to span the u-dimensional vector space. The points with the low P_L, high P_1 and second high P_2 function values are determined as well as the centroid P_c which is computed of all points except P_1. In each iteration the simplex can be reflected, contracted in one dimension, contracted around the low vertex (multiple contraction), or expanded. The reflected point P_R is computed by the reflection of P_1 through P_c

$$P_R = (1 + \delta)P_c - \delta P_1 \tag{3.6}$$

with δ = reflection factor. P_1 is replaced by P_R, if $f(P_L) < f(P_R) < f(P_1)$. In the case that $f(P_R) < f(P_L)$, the simplex is expanded along the centroid direction, so the new point P_E is defined as

$$P_E = (1 - \gamma)P_c + \gamma P_R \tag{3.7}$$

with γ = expansion factor. P_1 is replaced by P_E if $f(P_E) < f(P_L)$. If $f(P_R) > f(P_2)$ the simplex is contracted along the centroid direction (one-dimensional contraction),

$$P_C = (1 - \beta_1)P_c + \beta_1 min(f(P_1), f(P_R)) \tag{3.8}$$

with β_1 = one-dimensional contraction factor. P_C is replacing P_1 if $f(P_C) < min(f(P_1), f(P_R))$. In the case that $f(P_C) > min(f(P_1), f(P_R))$ instead of the one-dimensional contraction the whole simplex is contracted along P_L,

$$P_i = (1 - \beta_2)P_L + \beta_2 P_i \tag{3.9}$$

with β_2 = full contraction factor and P_i represents all points except P_L. After NELDER and MEAD (1965), $\delta = 1$, $\gamma = 2$ and $\beta_{1,2} = 0.5$. If a new generated point replaces P_1, the current iteration step is completed, if the termination condition is not reached yet, the next iteration is started. Termination conditions can be defined e.g. by the fit of the model or a certain number of iterations.

The standard downhill simplex approach uses arbitrary control factors for the reflection, contraction and expansion. By optimizing these control parameters the speed of convergence can be increased, e.g. KOSHEL (2002).

If the downhill simplex algorithm is applied several times by restarting the process with randomly generated initial unknown input parameters, the algorithm gets global optimization properties; the more the process is restarted, the higher the possibility that the process is running into the global optimum. The drawback of the restarting process is that the downhill simplex approach, which is itself faster than the global genetic algorithm, becomes slower with the increase of the number of restarts.

3.2 Global Optimization

The main feature of a global optimization tool, which is also the difference from the local approaches, is the implementation of a probabilistic part in the algorithm. The probabilistic part allows the process to exit from a local optimum to which it might run incorrectly.

Due to the limited amount of observation data as well as the need to implement constraints, (see Chapter 5.1) into the optimization, many global optimization algorithms run into difficulties while searching for the optimal solution.

The limited data source causes problems for running optimization with hidden Markov models or neural networks because they need a large amount of input data to get reliable results. On the other hand, simulated annealing, PRESS *et al.* (2002), runs into problems by solving constrained optimization problems. Therefore, the problem has to be transformed into an unconstrained one by formulating penalties. The simulated annealing has then to overcome infeasible regions with large increases in the values of its penalty functions. This makes it difficult for the algorithm to move from one feasible region to another or escape from local minima, especially when the temperature is low (equivalent to a small variation of the unknown parameters) WANG (2001).

Therefore, a genetic algorithm (GA) approach has been applied, due to its good performance with only a small amount of data as well as the possibility to define penalty terms which describe the defined constraints.

Furthermore, the genetic algorithm does not use derivatives to detect a descent in its optimization steps, so it is a good choice for non-linear parameter inversion. Therefore, in several recent studies in volcanology the GA has been applied successfully to determine magmatic sources, see TIAMPO *et al.* (2000), FERNÁNDEZ *et al.* (2001b), TIAMPO *et al.* (2004a), TIAMPO *et al.* (2004b), CHARCO *et al.* (2004).

In Chapter 3.2.1 the GA approach is discussed in detail, whereby it is focused on the special peculiarity of the applied algorithm, which is given by a modified approach of MICHALEWICZ (1992). (Note: Although the GA categorized as global optimization algorithm, the guarantee is not given that the GA finds always the global optimum. The likelihood to find the global optimum is larger for global than for local optimization algorithms.)

3.2.1 Genetic Algorithm

The genetic algorithm is a global optimization tool which is based on the natural selection of the biological evolution, inspired by Darwin's theory of evolution, Darwin (1859). GAs generate results of the optimization by taking biological selection and reproduction into account and are known to explore domains in relatively short time periods with giving good estimates of the solution, see Holland (1975), Goldberg (1989), Forrest (1993), Mitchell (1996) or Vose (1999) for general overview. The main properties of GAs according to Goldberg (1989) are described by four points:

- The algorithm works with coded parameter sets and not with the parameters themselves.
- The result of the optimization is evaluated through population sets and not only through one single solution as the downhill simplex approach is working, Chapter 3.1.1.
- The search is based on the objective function, not on derivatives.
- Probabilistic transition rules are used instead of deterministic ones which gives the possibility to reach the global optimum.

Every GA consists of

- a population size of individuals which are called chromosomes, whereby each chromosome is built of a sequence of genes by binary or real coding. The performance of both is highly problem dependent, Mitchell (1996), whereby the real coding approach is proved to be faster and more consistent from run to run, Bäck (1996). Moreover, it provides a higher precision especially for large domains. Binary coding also requires very large representations, Michalewicz (1992).
- a selection process in which chromosomes of the current generation's population are chosen for inclusion into the next generation. This selection has to be balanced with a variation of mutation and crossover because a too high selection creates suboptimal highly fit individuals, which dominate the population and would cause a reduction in diversity which is needed for further change and progress. In comparison, a too weak selection results in a very slow evolution, Mitchell (1996).

  Most common methods use fitness proportional selections like the Roulette wheel selection in which each individual is assigned a piece of a Roulette wheel proportional to its fitness. By randomly chosen individuals, the ones with the higher fitness have a higher likelihood to become a member in the group of selected individuals. The drawback is given in using small population sizes, because in this case, the likelihoods cannot be reproduced well by the population. Therefore, a stochastic sampling approach has been investigated, related to Baker (1987) who determined once at a time all selected members instead of repeating the choice of one member at each time, so each member is guaranteed to reproduce at least one time. Nevertheless, the main problem of fitness proportional selection cannot be solved with this selection. In the beginning of the algorithm, a small number of members is much fitter than the others and will be reproduced quickly by these selection schemes. Due to this effect the algorithm cannot explore the search space any more, which is called premature stagnation. Later in the search, no real differences in the fitness (which is used as selection criteria) occur, so the rate of evolution strongly depends on the variance of fitness in between the population.

These problems can be avoided by scaling methods of the fitness such as linear or sigma scaling. Other selections are based on the sorted population, like tournament or rank selection.

All mentioned selection schemes produce the offspring entirely out of the previous generation, whereby the steady state selection only replaces a few individuals in each generation, which is based on the Elitism scheme.

Elitism, according to JONG (1975) retains a number of best individuals at each generation in order not to lose them, so that they are not not-selected or destroyed by crossover or mutation. These kind of selection schemes are mostly used in evolving rule based systems with an incremental learning, HOLLAND (1975).

- crossover to produce new offspring which is, according to MITCHELL (1996), the main distinguishing feature of the GA. Generally, no kind of crossover can combine all possible schemes. Various kinds of crossover are given, whereby it can be distinguished between arithmetic and heuristic operators which use the fitness of the chromosomes. Arithmetic ones combine linearly two chromosome vectors; one example is given by the single point crossover, Figure 3.3a, where a position in the chromosome is chosen randomly and the two parts between the parents are exchanged in order to build two new offsprings. In particular, schemes with long defining lengths are likely destroyed by the single point crossover, which is known as positional bias. This kind of crossover forces that the segments which contains the endpoints of the strings are exchanged.

  Two point crossover reduces the positional bias and endpoint effect by choosing two positions and exchange the segment in between them.

  Another kind of crossover is given by the parameterized uniform type, where positional bias is completely avoided by the exchange at every bit with a given probability greater than 0, but it can be highly disruptive of any schema. Generally, the probability of crossover shall be large, whereby the computation cost increases with increasing crossover values but also improves the capability of the algorithm to reach the global optimum.

- random mutation of new offspring, Figure 3.3b. The operator flips randomly some genes in a chromosome and helps to prevent the population from stagnating at any local optimum. One main problem in GAs is given by the premature stagnation of the search, which is caused by the lack of population diversity. The mutation factor is the responsible factor for the generation of diversity, MICHALEWICZ (1992), whereby diversity can be ensured by large mutation factors corresponding to the chosen population size, RAMILIEN (2001). The determination of an effective mutation factor leads to various adaptive approaches for this parameter, e.g. HERRERA and LOZANO (2000), BÄCK *et al.* (2000), HANSEN (2000).

Generally, the GA generates populations consisting of several chromosomes at each iteration. Therefore, the initial population of chromosomes is generated randomly and is modified repeatedly by the GA algorithm. At each step, it selects the most valuable individuals out of the current population by the applied selection scheme, and uses them to produce the offspring for the next generation. This implies that the GA progressively changes from an initial completely random to a more deterministic sampling of the parameter space. The result of the GA can be improved by increasing the population size in order to avoid the lack of diversity, tune the mutation and crossover parameter or to rerun the GA with the last population from the first sampling approach, RAMILIEN (2001). The most important points in the optimization with a GA are given by the population diversity and the selective

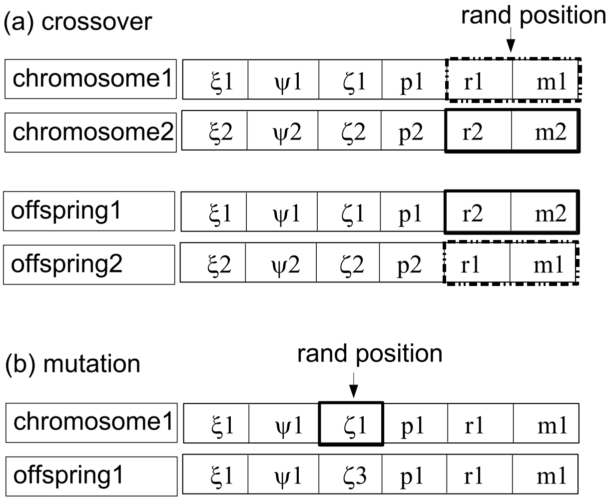

Figure 3.3: (a) Crossover with two chromosomes at randomly chosen position (rand position). (b) Mutation of a randomly chosen gene in the chromosome signed by the rectangle. The new gene is randomly new coded.

pressure, which are both influenced by the interplay between population size and mutation, MICHALEWICZ (1992).

The implementation of constraints into the GA can be carried out by formulating penalty terms which has been used several times in GA whereby they can be divided into the following methods:

- Death penalty method rejects infeasible solutions from the population. This rejection takes place in the selection step and can be seen as a method with infinite penalty, BÄCK *et al.* (1991). This method can get into difficulties to find the first feasible point.
- Static penalty methods are defined by certain coefficient values whereby difficulties occur by defining the right values, HAMIDA and SCHOENAUER (2000).
- Dynamic methods are working like static ones but the penalty coefficients change during the GA according to an user defined schedule.
- Adaptive penalty methods are described by the update of their values according to the certain population. Different approaches exist, whereby most rely on the best individuals on the past population to adjust the adapted penalty of the actual population, HAMIDA and SCHOENAUER (2000).

There exist various algorithm packages for the application of GA, RAMILIEN (2001), however in this study a GA approach is applied which is based on a modification of MICHALEWICZ (1992) and is described in detail in TIAMPO *et al.* (2000), TIAMPO *et al.* (2004a). A summary of the main properties leads to the use of the real coding of the chromosomes which are formed of the six unknown input parameters of the elastic-gravitational model (ξ, ψ, ζ, p, r and m). The selection scheme is chosen fitness proportional and is based on rank selection including the Elitism principle. The probability of mutation is set to a fixed, large value in order to avoid the mentioned premature stagnation of the GA. Proportional single point crossover is applied whereby the point of crossover in the individuals is chosen randomly between 0 and 1, see Figure 3.3a. The used single point crossover computes all genes in the offsprings after the randomly chosen point by a randomly chosen combination of chromosome1 and chromosome2.

Furthermore, a window function is used in case the search is stagnating. This technique narrows the difference between successive generations and increases the pressure to convergence by subtracting the fitness of the worst chromosome of the last generation from all individuals in the present generation. Generally crossover, mutation rate and population size typically interact in a non-linear way, so their determination in one step is not possible. Therefore these values have been anticipated as in previous and similar GA approaches, Tiampo *et al.* (2000) and Tiampo *et al.* (2004a). The mutation probability is set to 45%, probability of crossover is 95%, and the population size is set to 100 chromosomes. For the optimization configuration which implies constraints, a penalty term has been implied into the algorithm.

Chapter 4

Uncertainty and Sensitivity Analysis

Mathematical models are characterized by a certain degree of uncertainty which results of the uncertainty in modeled processes and observation errors as well as structural and numerical errors of the mathematical model. The confidence in the model prediction can be highly increased by applying uncertainty and sensitivity analyses.

The following list shortly describes the basic definition of uncertainty and sensitivity analyses.

- Uncertainty: The uncertainty of measurement is a parameter, associated with the result of a measurement, that characterises the dispersion of the values that could reasonably be attributed to the measurand, EA (1999). The purpose of an uncertainty analysis (UA) is the determination of the uncertainty in the estimates for the dependent output values. Normally, the uncertainty analysis is the first step and should be computed before the sensitivity analysis. If the uncertainty in the dependent output values is in a certain user defined range, there is no need for the performance of a sensitivity analysis. The model uncertainty can be determined by the application of parameter uncertainty approaches as well as model predictions for the observations. The uncertainty analysis describes uncertainties associated with the unknown input parameters, the observed data and the model structure.

- Based on WELSCH (1983) and PELZER (1985) the sensitivity analysis (SA) in geodesy is related to the sensitivity of monitoring networks which is given by the possibility to detect an expected movement in the network. The sensitivity analysis is carried out by hypothesis tests within a linear model. The sensitivity analysis as used in this study can be described more globally after SALTELLI *et al.* (2000) as "the study of relationships between information flowing in and out of the model". It can be seen as a tool for validating and optimizing a model due to the determination of the sensitivities of the different output values concerning changes in the unknown input parameters. This knowledge results in the quantification as well as the qualification of the unknown input parameters, so it can be derived which parameter has to be known best in order to reduce the variance of a certain output value.

4.1 Bayesian Uncertainty Analysis

For the uncertainty analysis the Generalized Likelihood Uncertainty Estimation (GLUE) has been chosen which is based on the concept of Bayesian inference. Bayesian inference is characterized by a number of advantages such as providing a confidence interval on the parameters as well as providing a way of formalizing the data's learning process in order to update beliefs in data.

Furthermore, the combined use of the Bayesian uncertainty estimation technique which was first used in hydrology, and of global sensitivity analysis techniques is the most effective approach, since it performs an uncertainty-sensitivity analysis based model assessment, in which all information (including observed trends of natural systems) can be used, Beven and Binley (1992). It is particularly applicable to large, over-parameterized models without any inverse solution, Ratto *et al.* (2001).

Bayesian uncertainty analysis is based on the estimation of probabilistic weights associated with each set of input parameter and the derivation of a posterior probability distribution function using the Bayes theorem, Equation 4.1. This distribution function is then used to derive the predictive probability of the output values. A large advantage of this method is due to the fact that the interactions between the input parameters are implicitly given by the likelihood of the samples: So that no hypothesis about the correlation structure is necessary in defining the prior distribution of the model parameters, Ratto *et al.* (2001) which is one of the reasons for its application in this thesis. Furthermore, the likelihoods, which are given as weight coefficients, can be taken for bootstrapping techniques in order to generate Monte Carlo samples by a resampling and replacement of model runs. So the input parameters are resampled with respect to the weight and a bootstrap sample of the posterior distribution can be obtained.

Generally GLUE works with a multiple sampling of the unknown input parameters which are given with a prior probability distribution. For each sample the model outputs are generated and weighted according to their fitness so that input parameters are never considered independently but as a set of parameters. The uncertainty prediction of the model is strongly dependent on these likelihoods. The fit (given as $1/\chi(comp)^2$) of each model is computed by the L_2-Norm, Chapter 3, Equation 3.4.

The Bayes theorem on which the uncertainty analysis is based describes the proportionality $P(A|BC) \propto P(A|C) \cdot P(B|AC)$: The posterior distribution $P(A|BC)$ of a parameter A is proportional to the product of its prior distribution $P(A|C)$ and the likelihood $P(B|AC)$. The theorem is given by Koch (2000),

$$P(A|BC) = \frac{P(A|C) \cdot P(B|AC)}{P(B|C)} \tag{4.1}$$

with $P(A|BC)$ = updated posterior probability of an unknown parameter, model or hypothesis A, $P(A|C)$ = prior probability of A, $P(B|AC)$ = likelihood, $P(B|C)$ = probability of an information B about the unknown A and C as further knowledge. The theorem can be applied to the unknown input parameters and also to the defined objective functions.

Anticipating A_i = unknown input parameters $\mathbf{X_i} = [\xi_i, \psi_i, \zeta_i, p_i, r_i, m_i]$ of the i-th sample, with $i = 1...N$ number of sample, $P(A_i|C)$ = prior probability of the sampled input parameter set i, given by an anticipated distribution, $P(B|A_iC)$ = likelihood of the sample i, given by $1/\chi(comp)_i^2$, $P(B|C)$ = prior probability of the objective function, the posterior probability of X_j ($j = 1...6$) is given by

$$P(X_j|1/\chi(comp)^2) = \frac{\sum_{i=1}^{N}(X_{i,j}) \cdot 1/\chi(comp)_i^2}{\sum_{i=1}^{N} 1/\chi(comp)_i^2} \tag{4.2}$$

The computation for A_i = objective functions $1/\chi(dg)_i^2$, $1/\chi(uz)_i^2$, $1/\chi(ux)_i^2$, $1/\chi(uy)_i^2$, $1/\chi(comp)_i^2$ is straightforward.

4.2 Sensitivity Analysis

Sensitivity analysis are applied in order to determine

- how each unknown input parameter (ξ, ψ, ζ, p, r, m) influences a certain kind of output value ($1/\chi(dg)^2$, $1/\chi(uz)^2$, $1/\chi(ux)^2$, $1/\chi(uy)^2$, $1/\chi(comp)^2$) qualitatively and also quantitatively.
- if and which of the unknown input parameters interact with each other.
- additional information for improvement approaches of the optimization, Chapter 5.2.
- which of the unknown input parameters (ξ, ψ, ζ, p, r, m) have to be known more accurate to reduce the variance of the output values.

According to Saltelli *et al.* (2000) sensitivity analyses can be categorized into

- quantitative or qualitative,
- model characteristics (e.g. additivity, linearity, monotonicity or interactions between the unknown input parameters) dependent or independent,
- local or global

methods. The choice of the kind of applied sensitivity analysis is dependent on the model of investigation, the number and nature of the unknown input parameters and the purpose of the analysis. Sensitivity analysis might have a diagnostic or prognostic, estimating character. The output value of the sensitivity analysis should be in the form of a single quantity, whose value is taken as the most valuable information that the model is supposed to provide.

In quantitative analyses the influence of the unknown parameters can be ranked in relation to their relative importance in the model. In qualitative analyses the influence of the unknown input parameters can be evaluated but they cannot be compared with each other.

Furthermore, it can be distinguished, if an analysis is capable to determine only the main or first order effect concerning an unknown input parameter or also all its interactions involving this unknown input parameter. The sum of the first order effects and all interactions caused by a certain unknown input parameter is known as the total sensitivity index (TSI).

Local sensitivity analyses are usually based on differential analyses like partial derivatives of the output functions with respect to the unknown input parameters or a finite-difference approximation. The input variables vary within a small interval around their nominal values. These can be interpreted as one-at-a-time experiments (OAT). In general, local methods are dependent on the model characteristics; the relation between input and output is assumed to be linear. One drawback of OAT techniques is that they are only able to compute the main or first order effects without the interactions between the unknown input parameters. These techniques tend to evaluate qualitative but not quantitative sensitivity results, Saltelli *et al.* (2004).

If the model is non-linear, a global sensitivity analysis with the aim to apportion the uncertainty in the output values due to the unknown input parameters should be used. Usually a global sensitivity analysis is described by the simultaneous variation of all input parameters, the computation over the whole range of each input value and the form of the probability density function (pdf) of each unknown input parameter. One example of global methods is given by variance-based techniques which are based on Monte Carlo sampling, Saltelli *et al.* (2000).

The main idea of this type of sensitivity analyses is based on the idea that one can determine the nature of the sensitivity through the variance σ^2 and then evaluate how the input variance contributes to the output variance. By setting $(X_1, ..., X_u)$ as the vector of independent unknown input parameters and $Y = f(X_1, ..., X_u)$ as the output value, with f as model function, an indicator for the importance of an input X_i can be set by evaluating the variance of the output Y $\sigma^2(Y|X_i)$. This is done by fixing X_i to its true value x_i. $\sigma^2(Y|X_i)$ is called the conditional variance of Y with $X_i = x_i$. The true value of x_i is not known, so instead of $\sigma^2(Y|X_i)$ the mathematical expectation of the conditional variance, noted as $E[\sigma^2(Y|X_i)]$ is studied, whereby it is built into all possible values of x_i.

The variance of Y is given by

$$\sigma^2(Y) = \sigma^2(E[Y|X_i]) + E[\sigma^2(Y|X_i)] \tag{4.3}$$

The first addend is called the variance of the conditional expectation and describes the importance of X_i on the variance Y, which is equivalent to the sensitivity of Y to X_i. Normalizing the sensitivity value S_i as the ratio between the variance of the expectation value and the variance of the output value leads to

$$S_i = \frac{\sigma^2(E[Y|X_i])}{\sigma^2(Y)} \tag{4.4}$$

and is called the first order sensitivity index, correlation ratio or importance measure. It describes the main effect of the unknown parameter X_i on the output value Y.

For an additive model the summation over the ratios of the unknown parameters results in 1. If interactions between the unknown input parameters exist, the entire decomposition of the objective function must be evaluated.

By propagating the variances of the unknown input parameters through the model, which determines the influence of this unknown parameter on the model output variance, some of the variance-based techniques can deliver quantitative as well as model independent sensitivity results.

The general procedure to carry out the variance-based sensitivity analysis is described by the definition of the pdfs for the unknown input parameters $\mathbf{X} = (X_1...X_u)$, the generation of Monte Carlo samples for $\mathbf{X}$ as well as the computation of the results of the physical underlying model using these samples, the analysis of the output variance and the sensitivity analysis of the output variance in relation to the variation in $\mathbf{X}$, Schwieger (2004).

Sobol' as well as a Fourier amplitude sensitivity test (FAST) show examples of variance-based sensitivity tests and they are according to Chan *et al.* (1997) the two only global methods which can deliver quantitative and model independent results, all alternative ones can at best offer a qualitative information about the model sensitivity. They can give information about the main effect of the unknown input parameter to the output variance $\sigma^2(Y)$, but for a quantitative sensitivity analysis the computation of the TSIs is indispensable. The categorization of these two methods is given as global, model independent and quantitative. FAST is, up to now, due to its more rapid convergence, more efficient, which is an important aspect for analyzing large data sets. Furthermore, Chan *et al.* (1997) stated that the computation of TSIs as well as the first order indices, is the only way to perform a rigorous quantitative, sensitivity analysis, in which the predominance of lower or higher order terms can be evaluated.

Due to the lack of knowledge if the underlying physical based mathematical model is additive or not, and its non-linear behavior, a variance-based, global sensitivity analysis which can also compute the interactions between the unknown parameters has been chosen. Because the number of unknown input parameters is very small with an amount of six ($\mathbf{X} = [\xi, \psi, \zeta, p, r, m]$), the aspect of computation time for the analysis is negligible for the choice of the method. From the two variance-based global techniques which allow the computation of TSIs, Sobol' has been applied.

4.2.1 Variance-Based Sobol' Sensitivity Analysis

The variance-based Sobol' sensitivity method is exploring the multidimensional space of the unknown input parameters $\mathbf{X}$ by a certain number of Monte Carlo samples. The evaluation of the equation is according to Saltelli *et al.* (2000). The sensitivity indices, first order (Equation 4.4) and also the higher interactions between the unknown input parameters, related to Sobol' (1993), are generated by a decomposition of the model function f in an u-dimensional factor space Ω^u into summands of increasing dimensionality,

$$\begin{aligned} f(X_1, ..., X_u) &= f_0 + \sum_{i=1}^{u} f_i(X_i) + \sum_{1 \leq i < j \leq u} f_{ij}(X_i, X_j) \\ &+ \quad ... + f_{1,...,u}(X_1, ..., X_u) \end{aligned} \tag{4.5}$$

with $X_1, ..., X_u$ = unknown input parameters and f_0 = const. The integrals of every summand over any of its own variables are zero and they are orthogonal. (Note: This constraint has to be satisfied by the sampling approach in order to apply the given formulas. If the sampling is non-orthogonal the formulas increase in their complexity). All terms in $f(X_1, ..., X_u)$ can be evaluated by multidimensional integrals. Squaring and integrating Equation 4.5 over Ω^u leads to the decomposition of the variance $\sigma^2(Y)$ of the output value $Y = f(X_1, ..., X_u)$:

$$\sigma^2(Y) = \sum_{i=1}^{u} \sigma_i^2 + \sum_{1 \leq i < j \leq u} \sigma_{ij}^2 + ... + \sigma_{1,...,u}^2 \tag{4.6}$$

with

$$\begin{aligned} \sigma_i^2 &= \sigma^2(E[Y|X_i]) \qquad (4.7) \\ \sigma_{ij}^2 &= \sigma^2(E[Y|X_i, X_j] - \sigma^2(E[Y|X_i]) - \sigma^2(E[Y|X_j]) \end{aligned}$$

The first order sensitivity indices are given by $S_i = \sigma_i^2 / \sigma^2(Y)$, higher order indices by $S_{i_1,...,i_s} = \sigma_{i_1,...,i_s}^2 / \sigma^2(Y)$.

First order sensitivity indices S_i measure the main effect of the certain unknown parameter X_i on the output and are quantitative sensitivity results for additive models. They represent the average variance reduction of the output which can be achieved if the certain unknown would be known and fixed. The higher order indices $S_{i_1,...,i_s}$ describe the interaction effects between the unknown input parameters $X_{i_1}, ..., X_{i_s}$ on the output value. These effects are not included in the individual effects of $X_{i_1}, ..., X_{i_s}$. The TSI_i of an unknown input parameter X_i is defined as the sum of all sensitivity indices, its main order effect as well as all the higher order effects in which this value appears. According to Saltelli *et al.* (2000) TSIs are quantitative sensitivity analysis results for all kind of models independent of their model characteristics.

The closed second order S_{ij}^c is defined by the sum of second order effect S_{ij} and first order effects S_i, S_j.

4.2.2 Regionalized Sensitivity Analysis

For the regionalized sensitivity analysis (RSA) Saltelli *et al.* (2000) a qualitative definition of the system behavior has to be given which serves as a binary classification of the model outputs. The unknown input parameter samples $\mathbf{c_i}$ with $i = 1....u$ and $u =$ number of unknown input parameters are classified according to the specified behavior definition related to the model outputs. If an input parameter of a sample can be classified as behavioral $\mathbf{c_i} : \mathbf{c_i}|B$, its model output lies in between the defined constraints. Otherwise the input parameter of the sample is classified as non-behaviorable $\mathbf{c_i} : \mathbf{c_i}|\bar{B}$, Hornberger and Spear (1981), Osidele (2001). In this way two sub samples for each unknown input parameter are created and the Kolmogorov-Smirnov two-sample test is applied to them. The test compares the distributions of values in $\mathbf{c_i}|B$ and $\mathbf{c_i}\bar{B}$. The null hypothesis H_0 and H_1 respectively are given with

$$\begin{aligned} H_0 &\quad : f(\mathbf{c_i}|B) = f(\mathbf{c_i}|\bar{B}) \\ H_1 &\quad : f(\mathbf{c_i}|B) \neq f(\mathbf{c_i}|\bar{B}) \end{aligned} \tag{4.8}$$

with f as probability density functions. The test statistics is then given by

$$T(\mathbf{c_i}) = max|F(\mathbf{c_i}|B) - F(\mathbf{c_i}|\bar{B})| \tag{4.9}$$

with $F =$ marginal cumulative probability function. If $T(\mathbf{c_i}) > F(f, \alpha)$, H_0 is rejected at the significance level α. The significance level α can be categorized after Saltelli *et al.* (2004) into three groups

- critical with $\alpha < 1\%$. It implies that the two sub samples differ significantly from each other, so that the unknown parameter of $\mathbf{c_i}$ is defined as a key factor in producing the defined behavior for the model.
- important with $1\% \leq \alpha \leq 10\%$
- insignificant with $\alpha > 10\%$. A high α value implies that any value in between the defined range of $\mathbf{c_i}$ is likely to fall in B or $\bar{B}$. Such input parameters are unimportant for the defined behavior of the model.

The RSA classification is related to main effects of variance-based global methods, see Chapter 4.2.1, higher order effects cannot be carried out. Nevertheless, the technique has many points in common with global sensitivity analyses like the variation of all unknown input parameters to the same time and its variation over the whole range in which they are defined. The advantage of this technique is that the samples must not have orthogonal properties. In addition, the Kolmogorov-Smirnov test assumes any continous distribution of data. Drawbacks of the RSA method are mentioned in the literature, Beck (1987), Saltelli *et al.* (2004): A lack of statistical power is appearing if the fraction of $\mathbf{c_i}|B$ is small and the number of unknown input parameters becomes large. The Kolmogorov-Smirnov test can only qualify an unknown input parameter as an important one to reflect the defined behavior, if H_0 is rejected. The reverse is not valid. Covariance structures in between the classifications cannot be detected and influence due to combined factors can compensate itselves. Furthermore, it is not possible to detect variations within the two sub samples. Nevertheless RSA can be used in order to study the variation of sensitivity. By defining the constraint as certain fitness classes (Equation 6.8 and 6.9), the RSA can give information if the sensitivity against certain unknown input parameter change by increasing or decreasing the fitness.

Chapter 5

Improvement of Optimization

Different improvement approaches of the optimization algorithm have been investigated in order to evaluate the most physical and statistical reliable model which is based on the non-linear inversion of the generalized static Navier equations, Chapter 2.1. Although a global optimization can find the global optimum of an objective function, the guarantee is not given; furthermore, a solution which reflects the global optimum might be physically not reliable. Due to these uncertainties in the optimization step, attempts to determine a better solution of the optimization problem are investigated in this chapter.

Initial results computed by a GA approach, TIEDE *et al.* (2004) showed that the unknown parameter ξ, ψ, ζ and m of the unknown source could be computed with only small dispersion values. But the samples show a large dispersion over the whole definition range for radius r and pressure p, see Table 5.1, with the total range as difference between maximum and minimum of the limitation range values.

parameter	minimal range	maximal range	% of total range
ξ [10^3 m]	439.354	439.487	6.68
ψ [10^3 m]	9166.045	9166.191	3.63
ζ [10^3 m]	0.018	0.226	20.93
p [10^5 Pa]	9.075	88.591	72.29
r [10^3 m]	0.382	1.036	43.67
m [10^{12} kg]	-0.01371	0.0686	8.24

Table 5.1: Variation in the parameters of the modeled source.

The sensitivity analyses showed larger sensitivity of all kind of observations against changes in the radius component compared to the sensitivity against changes in the pressure component of the unknown source. The RSA also states that the classification power of the radius component with increasing fitness of the objective function is rising, whereby it stays small for the pressure component, see Chapter 6.3.2. These results have been expected due to the defined energy form which is acting in the physical based mathematical model and which is defined by $p \cdot r^3$, see Chapter 2.1. Therefore, the improvement approaches mainly focus on the reduction of the dispersion in the determination of radius r and not of the pressure p.

Different attempts of improving the optimization approach are investigated. Generally the approaches can be categorized into the following two: One shall decrease the dispersion of r, the other approach shall verify the relevance of the determined models by additional observations from the area of interest. This is performed as follows:

- A decrease of the large dispersion, given in Table 5.1 of r is investigated in order to validate if the optimization algorithm can be modified so that the dispersion can be reduced for unknown parameters which are not easy to determine. This attempt is investigated in two different ways.
  - Implementation of physical constraints between the unknown input parameters in order to reduce the solution space of the unknown parameters. The constraints are implemented by penalty terms into the optimization algorithms and shall decrease the dispersion of the radius and pressure component of the unknown source.
  - Implementation of sensitivity analysis results concerning the radius component in order to increase the weight of these observations which are most sensitive against changes in the radius with the aim to decrease the dispersion of the radius component. Therefore the results determined by the Sobol' sensitivity analysis, Chapter 6.3.1 are taken into account.
- The computation of a physical reliability value for the position of the modeled source. In order to prove and interpret the results of the optimization, all available geophysical but also chemical and geological data have to be taken into account in order to allow a comprehensive evaluation of the model and its relevance to the assessment of volcanic risk. The reliability value is computed by a fuzzy logic controller which is implemented into the optimization. So the optimization can be improved with respect to the physical reliability of the source's position.

The following chapter describes the three mentioned implementations in more detail.

5.1 Definition of Constraints

For the downhill simplex as well as for the GA approach penalty terms are added to the algorithm in order to investigate an improved determination of the radius as well as the pressure component of the source. The penalties are set in that way, that the following physical constraints are satisfied,

- in the underlying physical based mathematical model, described in Chapter 2.1, the radius r and pressure p define an energy form $p \cdot r^3$. This energy form is not coupled with a certain shape, so the computed models cannot be interpreted by spherical sources. By anticipating a spherical shape of the source, a constraint can be defined which is implemented into the optimization as penalty term. By the anticipation of a spherical shape of the source the radius component is constrained by $r \leq \zeta$, so the source is completely within the mathematical half-space. This penalty also has to affect the determination of p directly, so the dispersion of the pressure must also be reduced.

- To interpret the mass of the point source as a medium with homogeneous density which fills this fixed spherical body, the relation between the mass m and the radius r of the unknown source has to be constrained, so the value cannot result in a physical non reliable density change $\delta\rho$. The relation between m, r and $\delta\rho$ is given by

$$m = \frac{4}{3} \cdot \pi \cdot r^3 \cdot \delta\rho \tag{5.1}$$

> For the computation of this constraint, the density model described in Chapter 6.2.2 has been used, so the computed densities described by Equation 5.1 satisfy $-\rho_{(\xi,\psi,\zeta)} \leq \delta\rho \leq 2670 - \rho_{(\xi,\psi,\zeta)}$ with $\rho_{(\xi,\psi,\zeta)}$ = density at the position (ξ, ψ, ζ) of the source.

Due to the implementation of penalty terms, which constrain the whole optimization concerning ζ, m, r and p, it may be possible to improve the determination of the radius component and, as a result, the pressure component. Furthermore, the penalties are chosen as large, so that the affected parameter set is rejected in the optimization which is equivalent to a death penalty term, Chapter 3.2.1.

5.2 Inclusion of Sensitivity Analysis Results

A second approach has been used in order to improve the optimization concerning the determination of the radius component. Therefore, the results of Sobol' sensitivity analysis, see Chapter 6.3.1, are taken for an improvement approach of the optimization, Tiede *et al.* (2005b). The approach consists of a re-weighting scheme of the cofactor matrix $\mathbf{Q_{ll}}$ of the objective function $1/\chi(comp)^2$. The normalized TSIs concerning the radius component $TSI()_{n,r}$ are implied, so the re-weighted $\mathbf{Q_{ll}}(\mathbf{r})$ is given by

$$\begin{aligned}
\mathbf{Q_{ll}}(\mathbf{r}) &= diag((\sigma_{dg_i} \cdot \frac{TSI(r)}{TSI(dg)_{n,r}})^2, (\sigma_{uz_i} \cdot \frac{TSI(r)}{TSI(uz)_{n,r}})^2, \\
& \quad (\sigma_{ux_i} \cdot \frac{TSI(r)}{TSI(ux)_{n,r}})^2, (\sigma_{uy_i} \cdot \frac{TSI(r)}{TSI(uy)_{n,r}})^2) \qquad (5.2) \\
TSI(r) &= TSI(dg)_{n,r} + TSI(uz)_{n,r} \\
& + TSI(ux)_{n,r} + TSI(uy)_{n,r} \qquad (5.3)
\end{aligned}$$

with $i = 1...20$, σ_{dg_i}, σ_{uz_i}, σ_{ux_i} and σ_{uy_i} = standard deviation of gravity change (dg), change in height (uz), east (ux) and north (uy) component of the i-th observation point.

5.3 Fuzzy Logic Controller

For the determination of the physical reliability of the models a fuzzy logic controller, described in Tiede *et al.* (2005c), has been developed due to the parallel of the earth behavior and fuzzy logic. Additionally the classical logic is mostly too rigid for mapping the nature's behavior. Fuzzy logic has been already applied successfully in various fields in geophysics, Gvishiani and Dubois (2002), An *et al.* (1991), Moon and An (2003). According to Cagnoli (1998) fuzzy logic gives an easy to use, mathematical tool for modelings in volcanology in order to define a vague and fuzzy system which is built of multiple sets of spatial data of the region of interest.

In fuzzy logic the mapping of an input to an output space is investigated by taking into account gradations between the two possible boolean outputs TRUE and FALSE. Fuzzy systems work with fuzzy sets instead of numbers whereby the fuzzy sets are characterized by a higher expressional power and permits a generalization of the information by implying imprecision.

Fuzzy logic is based on the ideas of Zadeh (1965), who established fuzzy logic in order to model the indefiniteness of the human language. The set of rules which connects the input with the output represents hereby the physical relation in analogy to an equational relation between in- and output values. A fuzzy set is an extension of a classical mathematical set A which is described by any collection of objects which can be treated as a whole. For an indefinite set A the members of the set can be described by an either-or predicate

$$A = \{x|x \in X\} \tag{5.4}$$

The fuzzy logic set is a further evaluation from this set by implementing a grade of membership in the way

$$A = \{x, B_i(x)|x \in X\} \tag{5.5}$$

with B_i = membership function of x in A which maps every element of X to a membership value.

Generally fuzzy controllers can be divided, according to their representation of information, into two categories. They mainly differ in the way the output membership function is defined.

The first kind of model, which is based on the Takagi-Sugeno-Kang method, Takagi and Sugeno (1985), is described by logical rules, consisting of a fuzzy part followed by a functional consequent (linear or constant). They are defined by a combination of fuzzy and non-fuzzy, and general conditions on the physical structure of the system can be implied. These models are able to give qualitative knowledge representations as well as quantitative information, Yager and Filev (1994). The technique uses a single spike as output membership function instead of a distributed fuzzy set (singleton output membership function).

The second kind is given by linguistic models which are based on IF-THEN rules and a fuzzy reasoning, generally known as Mamdani style inference, Mamdani and Assilian (1975). This type of models can be seen as an expert system, which describes linguistically the properties of the complex object. This style expects the output membership functions to be fuzzy sets, which have to be defuzzified. This step is related to a cost intensive computation of the output value compared to the computation in the Takagi-Sugeno-Kang model. A further drawback of these models is, that constraints which might be implied into the model (like energy conservation, etc.) cannot be modeled, so in this case the Takagi-Sugeno-Kang method should be used. Nevertheless the Mamdani method is more intuitive.

The construction of the fuzzy logic consists of the following four steps:

- Fuzzification of the input variables: For the input variables x_i the degree to which they belong to each of the appropriate fuzzy sets has to be determined via the membership functions B_{ji}. The function itself might have various shapes, Gaussian, triangle, trapezoid etc. and has to be chosen according to its assimilation to the property of the membership.
- Aggregation of fuzzy sets via fuzzy operators:
  If more than one antecedent builds a rule, the antecedents are aggregated to one output by aggregation operators. Generally, these operators are defined by the operator T of the t-norm and S of the t-conorm, which define the general class of intersection $(B_{i1}(x_1) \wedge B_{i2}(x_2))$ and union $(B_{i1}(x_1) \vee B_{i2}(x_2))$. These two norms are described by commutativity, associativity, monotonicity and one identity, zero identity respectively. The most common forms are given by the $min(B_{i1}(x_1), B_{i2}(x_2))$ for the intersection and $max(B_{i1}(x_1), B_{i2}(x_2))$ for the union, whereby a various amount of other definitions for the intersection and union exist (e.g. weighting, parameterized, compensatory or non monotonic approaches).
- Aggregation of the consequents across the rules: In Mamdani type models, which are known as constructive models, the output is constructed by superimposing the outputs of the rules, so the aggregation is investigated by a union of the individual fuzzy relations. In other types of models, called destructive

models, the output is determined by removing possibilities, which are not acceptable to the rules. This aggregation is described by an intersection.

- Defuzzification: The defuzzification processes a single number (e.g. a physical reliability of the position of a source) out of the fuzzy set, which consists of a range of output values. The used defuzzification methods is the centroid calculation, which returns the center of area under the curve. Beside this, a number of other methods exists like bisector, largest of maximum, smallest of maximum or weighted average of the centroids.

The developed fuzzy controller is based on a Mamdani-style inference, due to the fact, that no conditions have to be modeled by functional physical consequences. Furthermore, the model shall be set up highly intuitive due to the lack of input data, which can describe the reliability of the elastic-gravitational source position. Also, the vague anticipations which can be drawn regarding the relation of the position of the source and its reliability are a reason for choosing this kind of model. The model is designed as a multiple-input, single-output (MISO) fuzzy logic controller.

The following information has been used as input variables for the fuzzy logic controller:

- Density of the source's position:

  The density model, described in Chapter 6.2.2 is used. Magma sources are anticipated as more physical reliable, if they are located in loose material, due to magma building funnels through the rocks and should use the way of the smallest energy effort. The denser the material is getting, the less reliable is the position for a potential magma source anticipated.

- Depth of the source:

  The source is anticipated to be shallow according to RATDOMOPURBO and POUPINET (2000), KÖRNER (2000) and CAMUS *et al.* (2000). CAMUS *et al.* (2000) propose two reasons. First, the more or less continuous growth of summit domes, which are interrupted by collapses and phases of quiescence, would match the idea of a continuously depleted and refilled magma reservoir at a small depth and second, the absence of large ignimbrite[1]eruptions. Also COMMER (2003) argues that due to the constant activity of Merapi, it is likely that regions of partial melts exist below the summit. Tilt and GPS data give no evidence for a large magma chamber in a depth larger than 1000 m below Merapi's surface, REBSCHER *et al.* (2000). According to former research, magma sources were located in a depth of 6000 and 9000 m according to BEAUDUCEL and CORNET (1999). These models could not be testified by the observed gravity changes and displacements, see Chapter 6.3, Figure 6.11 and 6.12, so this information has been neglected in the definition of the fuzzy rule.

- Distance between the modeled source and the summit of the volcano:

  Since the significance of the measured changes in gravity as well as in displacements is decreasing with increasing distance to the summit, see Chapter 6.2.1, influences which are caused by the volcano, are supposed to originate from the vicinity to the summit. The physical reliability of a source is decreasing with an increasing distance to the summit of the volcano larger than 1000 m, GERSTENECKER(2005, personal communication).

---

[1] The rock formed by the widespread deposition and consolidation of ash flows and nuées ardentes. It is characterized by an inhomogeneous composition in terms of the grain size of its constituents, MATTHES (1990).

For the fuzzification of the variables different membership function are applied. The asymmetrical polynomial curve (smf) is open to the right and is described by its two extreme values a and b of the slope portion of the curve,

$$y = \begin{cases} 0 & : \quad x \leq a \\ 2((x-a)/(b-a))^2 & : \quad a < x; x \leq (a+b)/2 \\ 1 - 2((b-x)/(b-a))^2 & : \quad (a+b)/2 < x; x \leq b \\ 1 & : \quad b \leq x \end{cases}$$

with $x_{min} \leq x \leq x_{max}$ as the input variable defined between its lower x_{min} and upper x_{max} bound. The mirror-image function (zmf) is open to the left and is described by the same values a and b. The fuzzy rules result of the physical information about density, depth and distance to the summit of the source which are mentioned before. They are given in Table 5.2.

MF concerning	name of MF	a	b	property
density $[kg/m^3](x_1)$	small density (B_{21})	-222	100	zmf
	large density(B_{11})	-100	224	smf
depth $[m](x_2)$	shallow depth (B_{22})	0	4000	zmf
	large depth (B_{12})	2000	8000	smf
distance to top $[m](x_3)$	near distance (B_{23})	0	2000	zmf
	far distance(B_{13})	1500	3500	smf
reliability [%](V)	bad reliability (D_1)	0	0.5	zmf
	large reliability (D_2)	0.5	0.9	smf

Table 5.2: Fuzzy Membership functions (MF).

The whole fuzzy system is shown in the flow chart, Figure 5.1.

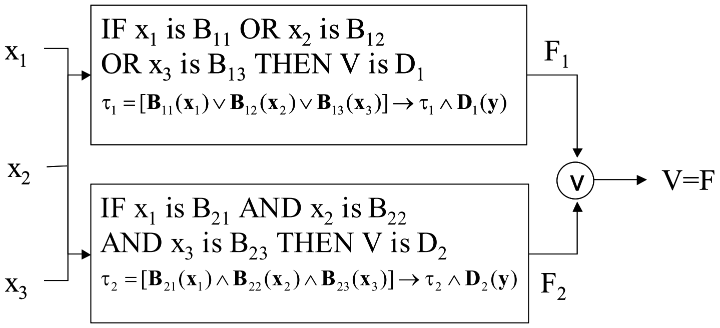

Figure 5.1: Flow chart, displaying the created fuzzy logic controller.

The rules were aggregated by the computation of the maximum of the three input values (density, depth and distance to the top). The defuzzification of the final output fuzzy set for the physical reliability of a source's position has been computed with the centroid method.

The output reliability V for each location which is generated by the optimization approaches is added with a multiplication factor λ to the value of the objective function $1/\chi(comp)^2$

$$1/\chi(comp)^2_{fuzzy} = 1/(\chi(comp)^2 + \lambda \cdot (1 - V)) \tag{5.6}$$

whereby λ has been anticipated as 10 for the first configuration approaches. Further results with $\lambda = 100$ are given in TIEDE *et al.* (2005c).

Chapter 6

Application Case - Merapi

6.1 Prior Information

Merapi volcano, located on Central Java, Indonesia, is one of the most active and hazardous volcanoes worldwide.

Around two million people are living in the surrounding area of the volcano; the Merapi Volcano Observatory (MVO) counts 70000 people even staying in the so called forbidden zone of the volcano, which is characterized as the zone where pyroclastic flows, ash falls, volcanic bombs and lava flows are causing the primary dangers. Approximately 30 km south of Merapi, the capital Yokyakarta is located with about 500000 inhabitants. This population is permanently threatened by the volcano, so Merapi has been classified as a high-risk volcano. It has been chosen as one of 16 global Decade Volcanoes by the International Association of Volcanology and Chemistry of the Earth's Interior (IAVCEI), IAVCEI (1994).

The aim of the Decade Vocanoes project is to direct attention to a number of selected, active volcanoes worldwide in order to enhance an understanding of the volcanoes and the hazards posed by them by research and public awareness. It represents the primary contribution of IAVCEI to the "International Decade for Natural Disaster Reduction Program" (IDNDR). IDNDR has been initiated by UNESCO with the target to get more knowledge about the structure, the temporal behavior of volcanoes as well as about prediction capabilities.

The project "Untersuchungen säkularer Schwereänderungen am Merapi, Java: Ursachen und Wirkungen", Ge 381/12 1-4, had been a part of an interdisciplinary research cooperation called MERAPI (Mechanism Evaluation, Risk Assessment, Prediction Improvement) between the Geoforschungszentrum Potsdam (GFZ) and the Volcanological Survey of Indonesia (VSI) as coordinating parties. The project had been financed by the Deutsche Forschungsgemeinschaft (DFG).

The project parts of MERAPI can be distinguished concerning their different targets:

- Monitoring: Continuous measurements of seismology, gas analysis and deformation for monitoring purposes.
- Geological work for magma evolution and eruption history.
- Structure analysis: Geophysical measurements of DC geoelectrics, gravity, Long Offset Transient Electromagnetics (LOTEM), magnetotellurics and seismics for exploration of the structure of the volcano.

An overview about all 13 projects of MERAPI is given by Zschau *et al.* (1998).

Merapi volcano (ϕ = -7°32′25.64″, λ = 110°26′47.88″, h = 2969 m (ellipsoidal height referenced to WGS84)) is located near the subduction zone, which forms the 6000 to 7000 m deep Java trench approximately 250 km south of the coastline of Indonesia, where the Indo-Australian plate is moving toward the Eurasian one and is subducted below it. The convergence of the plates in Java is frontal with an average velocity of 0.065 m per year, Mets *et al.* (1990). This subduction zone is responsible for the high volcanism and seismic activity along the Sunda arc between Sumatra till Flores, Gertisser (2002). In all the Indonesian islands there exists more than 129 active volcanoes, 76 of them showing historical activity, Simkin and Siebert (1994). According to Gertisser (2002) the geology of Central Java is divided in several structural units; the south coast including the Karangbolong mountains, the south Seraju chains and the west Progo mountains, the south mountains, the west foothills of the Solo zone, the north Seraju and the north coastline. Merapi, a volcano of the late Pleistocene - Early Holocene, is located at the intersection of two quaternary fault zones, the N-S striking Semarang fault and the E-W located Solo fault. It is the youngest volcano situated at the intersection of two volcanic alignments, a volcanic chain beginning in the north with Ungaran and continuing southwards with Telemoyo, Merbabu and Merapi, Figure 6.1 and the E-W located volcanic alignment consisting of Lawu, Merapi, Sumbing, Sindoro and Selamet. The N-S located volcanic chain is the continuation of the N-NW to S-SE striking fault zone, Bemmelen (1949). The topography of the volcano is bell shaped with a mean dip angle of 5°up to 1300 m, 15°up to 1700 m and 26°up to the summit, Berthommier (1990). In the lower part of Merapi until an altitude of 2500 m above sea level, the volcano is covered with dense vegetation.

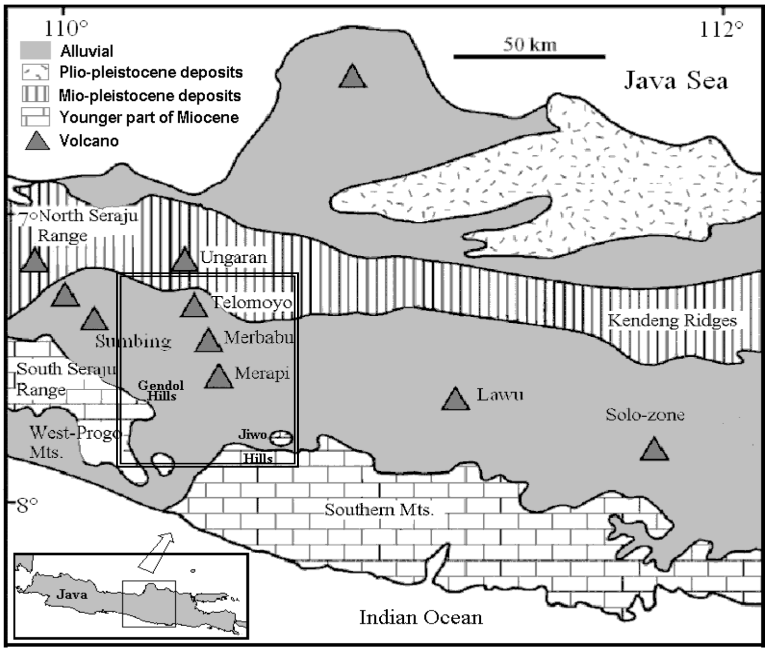

Figure 6.1: Geology of Java, Indonesia after Bemmelen (1956). Double square shows the area of observed data, Chapter 6.2.

Bemmelen (1949) points out that the area around Merapi consists of two different materials: The basic material is alluvial with a lower density, whereas the volcanoes themselves consist of Holocene volcanic material.

The volcano itself is formed according to Gertisser (2002) by four stratigraphical units called Pre- (Gunung Bibi), Proto-, Old- and New-Merapi.

The summit structure of Merapi itself is characterized by a crater which has moved westwards in recent years and is occupied by an unstable lava dome that is built out of the very viscous lava. The Merapi andesites typically contain 30-50% phenocrysts and are as much as 75% crystalline; the high crystallinity together with the rhyolitic composition of groundmass glasses accounts for this high viscosity, VOIGHT *et al.* (2000). The summit structure is essentially formed by unpacked rock as well as fractured lava blocks and ash matrix breccia, BEAUDUCEL *et al.* (2000). The base of Merapi consists of a sequence of basaltic andesite lavas and pyroclastic deposits of the Old-Merapi which is an eroded older volcanic edifice, NEWHALL *et al.* (2000). Old-Merapi itself is covered by the deposits of New-Merapi.

The slipping of the older part of the volcano to the west is assumed by BEMMELEN (1949) but not yet verified. Rocks of Merapi show densities between 2000 $\leq \rho \leq$ 2400 kg/m^3 up to a depth of about 2000 m, UNTUNG and SATO (1978). At larger depths, a denser material of 2660 kg/m^3 is anticipated. From seismological studies the lava density is determined as 2400 kg/m^3, JOUSSET *et al.* (2000). The study of gravity inversion in the area of Merapi and Merbabu leads to a mean density of 2242 kg/m^3 and variations between 2000 kg/m^3 $\leq \rho \leq$ 2504 kg/m^3 in the region around Merapi and Merbabu, TIEDE *et al.* (2005a), see Chapter 6.2.2.

Estimations of the porosity of the material reflects values of about 10 - 20% suggested by results of gravity observations, SETIAWAN (2002) and gravity inversion, TIEDE *et al.* (2005a). These values are assumed by MÜLLER *et al.* (2002) to explain fluid resistivities of 0.2-1 Ωm, values which also result from the study of magnetotelluric observations.

The activity of Merapi is characterized by frequent eruptions within one to five year intervals, with weak explosions and low gas pressure. The system is open due to the small pressure which is only necessary to carry material; therefore, measured deformation at the flanks of Merapi are small, see Chapter 6.2.1.

Pyroclastic flows which accompany volcanic eruptions can be divided into flows which are caused due to a dome collapse and flows which are caused by debris erupting vertically. The run out distance of these flows is usually about 6000-7000 m from the summit with velocities up to 110 km/h and a temperature about $300 - 400$ °C, SCHWARZKOPF *et al.* (2005). The following list (modified after VSI) gives an overview about the main volcanic events between 2000 and 2002 for which all modeling approaches are investigated in this study.

- 08-10/2000: Increase of volcanic and seismic activity.
- 12/2000: Eruptive activity increased between 12/26/2000 until 02/05/2001. Ongoing lava avalanches, pyroclastic flows, ash eruptions with an average interval of 0.5-1 hour. Dome collapse around 01/16/2001. New growing dome collapsed at 01/28/2001.
- 02/10/2001: Major eruption, high seismicity, decreasing magnetic intensity near the summit, indicating high heat and magma near the surface.
- until 07/2001: Volcanic activity continued but with a decreasing intensity. High fumarole temperatures around the summit indicated that magma remained near the surface. In 03/2001 high pressure fumaroles appeared on most of the dome's surface.
- 08/17/2001: Eruption at 08/19/2001. 25 lava dome collapses, lava extruded from the dome vertically.
- 08/2001-02/2002: Avalanche earthquakes dominate seismic activity, minor pyroclastic flows occurred. Heavy rainfalls in 11/2001.

- 06/02/2002: Lava avalanches and minor pyroclastic flows. The seismicity was dominated by avalanche earthquakes. Activity decreased to the end of 06/2002.

- 07-09/2002: Seismicity was dominated by avalanche earthquakes and frequent lava avalanches.

Detailed activity events are given in Figure 6.2 showing data collected by the MVO for the time period between 08/01/2000 and 08/22/2002. The first half of the period is dominated by frequent shallow and deep seismic events (VTA and VTB, Ratdomopurbo and Poupinet (1995) or Brodscholl *et al.* (2000)) as well as multiphase events and nuée ardentes. The second half is dominated by low frequency events and rockfalls. Seismic measurements show several local events for the area of Merapi and provide some information on the internal structure of Merapi: Seismic active experiments in a radius of 5000 m from the active dome show similar characteristics to natural seismic signals on the moon, Wegler and Lühr (2001). The measurements concentrate on the examination of the shallow structure of the volcano. From this study it turned out that scattering (related to the inhomogeneous shallow structure of the volcano) has an important influence on the observed seismograms. Measurements by Ratdomopurbo and Poupinet (2000) reveal a zone with anomalous high attenuation of seismic waves in a depth about 1500 - 2500 m below the summit, which has been interpreted as a shallow magma reservoir. According to Camus *et al.* (2000), the eruption history of the period starting at the end of the 18th century also suggests such a reservoir. Seismic data from Ohrnberger *et al.* (2000) do not show clear indications for an aseismic zone. Also LOTEM observations neither support a vertically extended conduit nor a shallow or deep magma reservoir, which would explain a very low resistivity, Commer (2003).

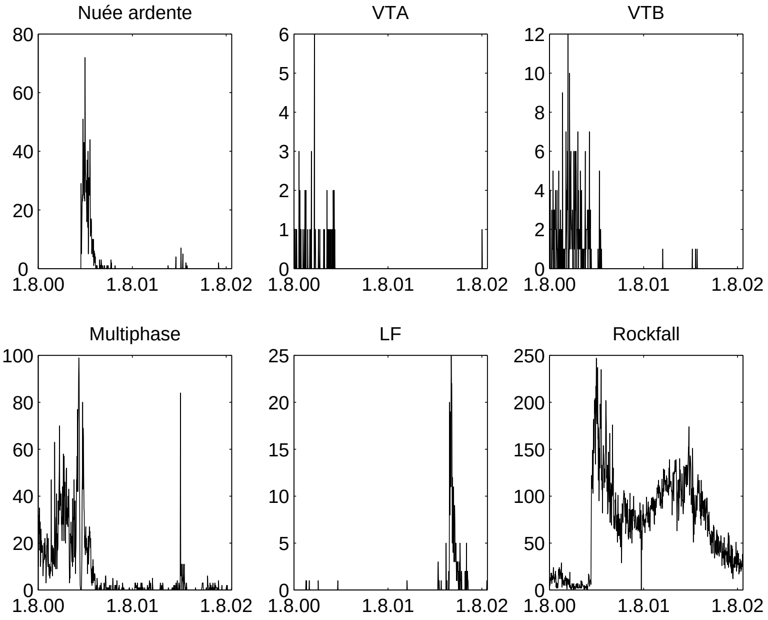

Figure 6.2: Activity at Merapi between 08/01/2000 and 08/22/2002.

On the basis of GPS and tilt data, Beauducel and Cornet (1999) modeled magma sources located 6000 and 9000 m below the summit. This result does not confirm the anticipated shallow magma source of Ratdomopurbo and Poupinet (2000). Körner (2000) modeled shallow magma chambers with different shapes on the basis of GPS and tilt data whereby a definite geometry and pressure could not be evaluated. He assumes pressure between $30 - 40 \cdot 10^5$ Pa for a magmatic source located only a few hundred meters below the surface. Furthermore, the dome weight approximations lead to the assumption that the pressure for the transport of magmatic material has to be smaller than $30 \cdot 10^5$ Pa, whereby magmatic masses are anticipated as too small to influence the deformation field at all. According to Friedel and Jacobs (2004) overpressure around several 10 MPa can be anticipated in the shallow subsurface.

Setiawan (2002) computed magma chamber and conduit models in order to explain measured gravity changes between 1997 and 2000. The volume of magma in the conduit is modeled. The conduit system is modeled by a cylinder, the magma chamber by a sphere or ellipsoid. The magma chamber has been located at a depth of 8000 m, 2000 m SE of the summit. The observed gravity changes at points near the crater rim could be explained by the flow of the magma in the conduit, whereby gravity changes far away from the summit are explained by changes in the hydrothermal system. Furthermore, it turned out that Merapi must be an open system due to the small deformation and gravity changes which could be measured around Merapi.

Also Jentzsch *et al.* (2004) analyzed these gravity changes and deformation observed between 1997 and 2000 but put the observed changes down to a water saturated layer in a depth of 1000 m with varying density, anticipating a two-dimensional model. The reason for rejecting the classical Mogi model for a shallow extending magma reservoir has been that the observed gravity changes between 1997 and 2000 are not accompanied by significant elevation changes, so that the internal pressure variations do not lead to significant deformation at the surface.

Gas emission monitoring was measured by Zimmer and Erzinger (2003) between 2000 and 2001 at two fumarolic fields, Gendol and Woro, near the summit. The purpose of this study had been the determination of the fumarole temperature as well as the study of water vapor and carbon dioxide contents. Gendol, with temperatures >800°C, is located 150 m SE from the summit, and Woro, with temperatures $>600\ ^{\circ}C$, 250 m SE of the summit, Figure 6.3. Results show that gas concentrations and temperatures in the fumaroles change relatively fast, whereby the possibility is discussed that the periodic changes of carbon dioxide, water vapor and the temperature are related to the regularly fluctuating input of meteoric or hydrothermal water to the fumaroles. Allard (1982) stated that the source of water vapor in Merapi gas might be related to the surface and not to deeper seeds, whereby the correlation between rainfall, gas temperature and seismicity also points to an impact of cool water in deeper and seismic active zones.

Figure 6.3 gives an overview about the summit region with local fracture zones as well as the mentioned fumarole fields Gendol and Woro.

Resistivity contrasts at volcanoes are mainly caused due to the difference between cold, dry and non conductive host rock and the hot, wet and conductive magma, or respectively, its hydrothermal system.

LOTEM observations focus on the detection of the conductivity structures below the summit region. Derived results show a strong monotonous resistivity decrease with increasing depth, Commer (2003). This result coincides with conclusions drawn from DC resistivity imaging along the volcano's flanks, Friedel *et al.* (2000), that observed a successive resistivity decrease with depth, with resistivity values below 30Ωm in a depth below 500-1000 m from the surface. Furthermore, a high conductive layer dislocation of about 7700 m south of the summit has been observed by LOTEM measurements, Müller *et al.* (2002), Kalscheuer (2004) and NanoTEM, Koch (2003).

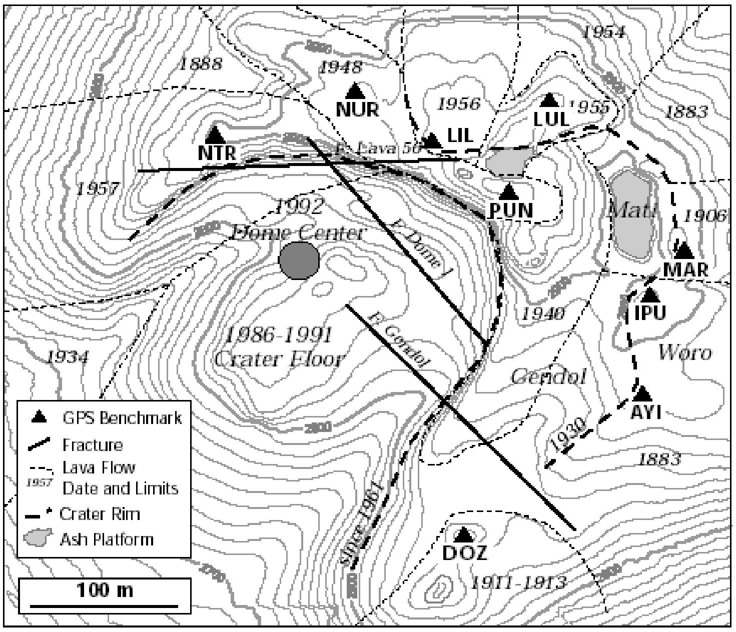

Figure 6.3: Structural map of the summit region from Beauducel *et al.* (2000).

Commer (2003) confirms the existence of an extensive conductive zone below the volcanic edifice which was found by three-dimensional forward modeling of LOTEM data. Also a conductivity structure which is following the topography and an upwelling of conductivity sources below the summit would confirm the idea of a vertical fluid transport as postulated by Commer (2003).

At greater distances from the summit, fluids neither directly related to the hydrothermal system of the volcano nor enriched by hydrated minerals may be the most likely cause for the shallow conductivity in these regions.

According to Commer (2003) LOTEM results provide the existence of a hydrothermal system. Fluids seem to be the main reason for the extensive region of high conductivity but not for high conductivities below depths of 900 m. This would require higher porosities, Commer (2003), and the resistivity should increase by going downwards due to the bulk porosity decreasing with depth by compression of cracks and pores, Ryan (1987).

Results from magnetotellurics are given by Müller (2000b) and Müller (2000a) as well as Müller and Haak (2004). Results of three-dimensional magnetotellurics forward modeling including topography are given in Figure 6.4.

- (A) upper layer with a resistivity of 100 Ωm.
- (B) 10 Ωm conductive layer, whereby the layering itself might be a simplification of a more continuous resistivity decrease with depth, Müller and Haak (2004).
- (C) extended conductive layer with a resistivity of 1 Ωm in a depth between 400 to 1800 m below sea level.
- (D) radial symmetric conductor with a resistivity of 10 Ωm and follows approximately the topography with its upper boundary between 1000 to 1600 m.

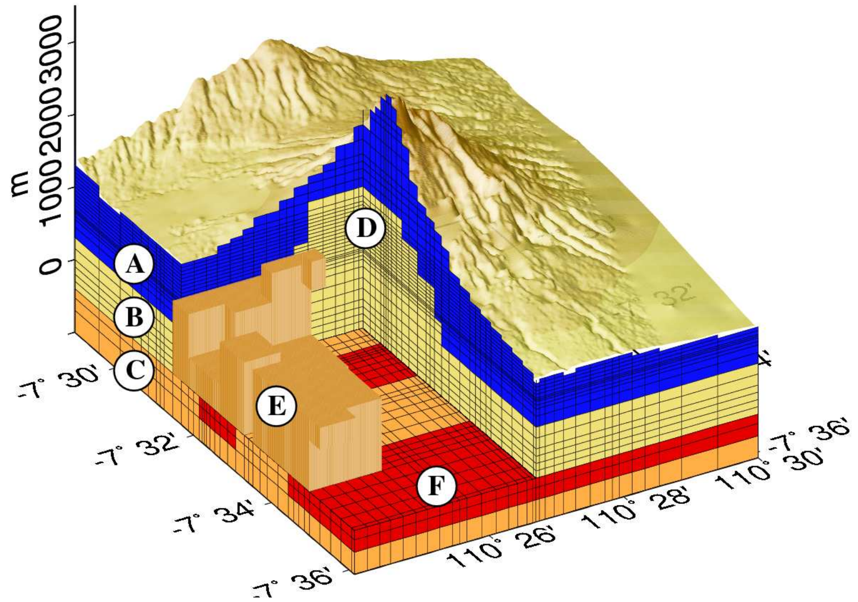

Figure 6.4: Three-dimensional model of the electric resistivity distribution under Merapi volcano from Müller and Haak (2004).

- (E) high conductive SW anomaly with a resistivity of <1 Ωm. It is located about four km SW of the summit, 300 m below the surface. The outline of the conductor coincides with regions of young volcanic deposits, its approximate volume is given by 20 km^3.
- (F) two two-dimensional regional structures extending beyond the volcano with a resistivity of 0.1 Ωm.

The high conductivity of the conductors is caused by saline fluids rather than by clays or melts, Müller and Haak (2004), which originate from meteoric water that is flowing through young volcanic deposits at the surface and accumulates in the SW anomaly (E).

Beside this complete three-dimensional conductivity model, several regional results exist, Hoffmann-Rothe *et al.* (1998), Ritter *et al.* (1998).

The possible explanation of high conductivity by the intrusion of seawater is neither supported by magnetotelluric results, Ritter *et al.* (1998), Müller and Haak (2004) nor from results of LOTEM, Commer (2003).

6.2 Data Sources

6.2.1 Combined Gravity and GPS Network

This chapter introduces the gravity changes as well as the vertical and horizontal displacements, observed between 2000 and 2002, in more detail, because they form the input of the modeling approaches in the next sections.

In 1997, a combined GPS and gravity network was established, which initially consisted of 18 gravity and GPS points, arranged in three loops and one profile. The profile is connecting the loops at the north flank of Merapi. The loop configuration was chosen in order to minimize the scale factor errors of the gravimeters. In 1998 the network was enlarged by five more observation points. The first loop was installed in an altitude of 130 to 650 m, the second 850 till 1500 m and the third loop with an altitude more than 2900 m. The measurements were carried out in four to six week long campaigns in 08/1997, 08/1998, 08/1999, 08/2000 and 08/2002 during the dry season as well as one campaign in the rainy season, in 02/1998. The repetition network covers a whole gravity range about 751 mGal and a height range of 2837 m.

Figure 6.5 displays 20 observation points of the repetition network at which gravity and GPS were measured in the year 2000 as well as 2002. GPS data were measured with up to 11 dual frequency Trimble GPS receivers, whereby five were installed permanently and the other six served as rover and reference stations.

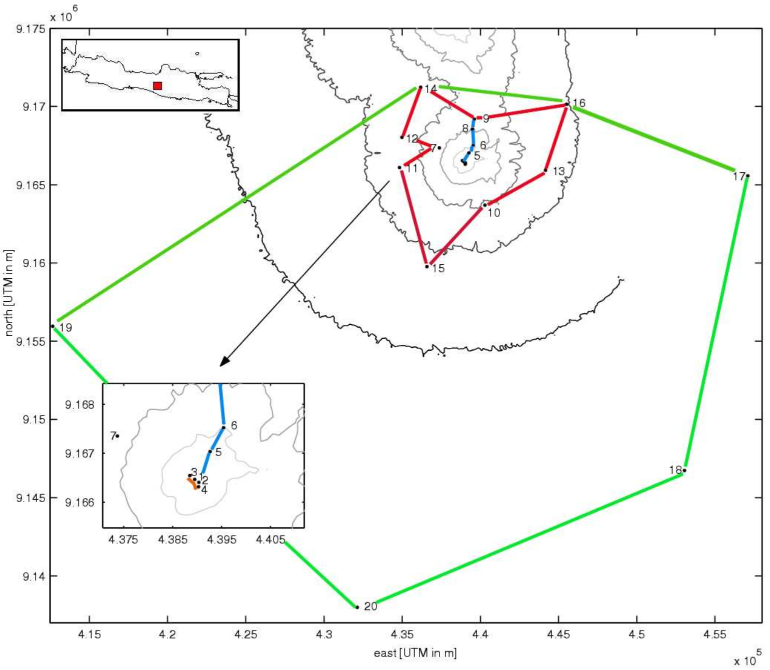

Figure 6.5: Repetition Network showing the observation points and the loop construction, installed in 1997.

The baselines of the GPS measurements have a range up to 30 km. The network is connected to the International GPS Service stations (IGS, HTTP1 (2005)) COCO, DARW, and NTUS (see also Table 6.3), Götz (2003).

The mean standard deviations of the GPS measurements in east, north and height are given in Table 6.1.

observation	08/2000	08/2002
east [m]	0.004	0.002
north [m]	0.003	0.003
height [m]	0.019	0.013
gravity [mGal]	0.0077	0.0067

Table 6.1: Mean standard deviations of GPS observations.

For each campaign four Lacoste&Romberg relative gravimeters had been used simultaneously in order to minimize systematic errors of the instruments. The data were processed with the Feldgrav software, GERSTENECKER (1990), in which a free least squares adjustment has been implemented. The accuracy of the adjusted gravity data is given in Table 6.1.

From the gravity observations the anomalous mass Δm between each two consecutive measurement periods had been computed via the Gauss theorem, Equation 6.1 which leads to very small mass changes between the epochs, given in Table 6.2 with Δm_{surf} = anomalous mass computed by surface gravity residuals, Δm_{FA} = anomalous mass computed by free air gravity residuals, Δm_{BCFAG} = anomalous mass computed by Bouguer corrected free air gravity residuals.

$$\Delta M = \frac{1}{2\pi G} \int \int dg dS \tag{6.1}$$

with dg = gravity residual between two epochs at a surface element and dS = surface element. The quadratic surface elements have a length of 500 m. The masses are computed in between the area given by $435 \cdot 10^3 \leq$ east $\leq 441 \cdot 10^3$ m and $9160 \cdot 10^3 \leq$ north $\leq 9170 \cdot 10^3$ m.

epoch	ΔM_{surf} [10^{10} kg]	σ [10^8 kg]	ΔM_{FA} [10^{10} kg]	σ [10^8 kg]	ΔM_{BCFAG} [10^{10} kg]	σ [10^8 kg]
8/00-8/02	-0.558	0.294	0.452	0.364	0.144	0.3302

Table 6.2: Anomalous masses computed for the given measurement epochs.

From this mass the magnitude and intensity is computed according to SIGURDSSON (2000). The mass which is ejected between 08/2000 and 08/2002 defines the magnitude = 2. The intensity which defines the eruption rate (kg/s) is given by 4.3 which is a typical value for the continuation of dome forming eruptions, SIGURDSSON (2000). Magnitude as well as intensity show very small values which point out the gentle eruption activity of Merapi during the given time period.

The observed gravity changes and the vertical as well as horizontal displacements which were split in east and north component including 1σ-error bars of these stations are shown in Figure 6.6. Table 6.3 and Table 6.4 show the location of the points in east, north and height and the observed changes in gravity dg, height uz, east ux and north uy, including their standard deviations σ and sorted by increasing distance to the summit. The summit of the volcano is given by the UTM-coordinates east$_{top}$ = 438952.35 m and north$_{top}$ = 9166465.95 m.

Gravity changes between 2000 and 2002 lead to a mean standard deviation of $\sigma_{\overline{dg}} = \pm 0.012$ mGal. Vertical displacements could be measured with $\sigma_{\overline{uz}} = \pm 0.024$ m as well as east displacements with $\sigma_{\overline{ux}} = \pm 0.004$, north displacements with $\sigma_{\overline{uy}} = \pm 0.003$ m respectively.

The significance of the data has been tested by applying t-test statistics

$$T = \frac{\mathbf{l}}{\sqrt{\mathbf{Q_{ll}}}} \sim F(t, r, 1-\alpha) \tag{6.2}$$

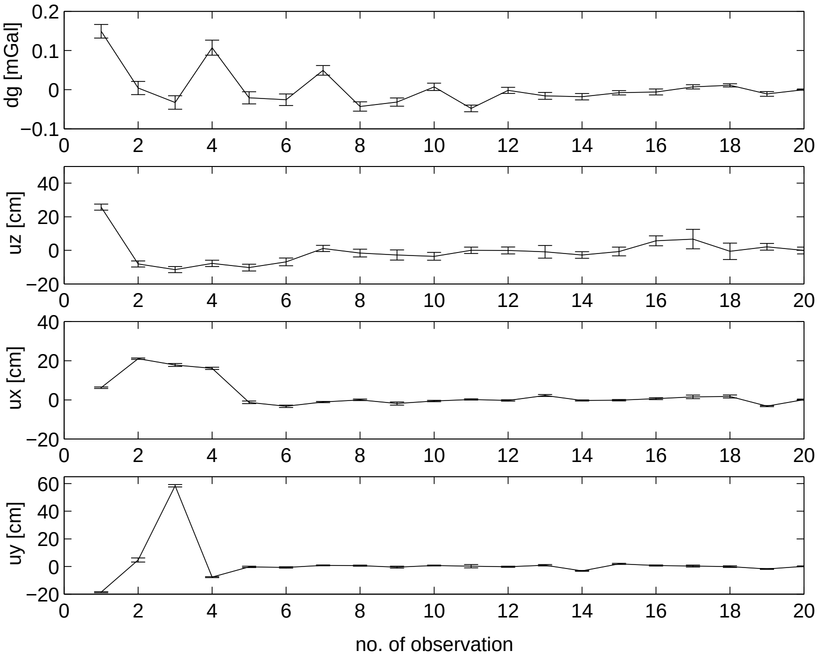

Figure 6.6: Gravity changes dg, vertical displacements uz, horizontal displacements ux, uy including 1σ-error bars, observed between 2000 and 2002 at Merapi volcano.

Point No.	distance to top [m]	name	east [m]	north [m]	height [m]
1	0.2	JRA13	438952.288	9166466.136	2969.059
2	103.2	IPU0	439035.976	9166405.401	2932.310
3	128.6	JRA15	438851.075	9166545.225	2935.814
4	168.7	JRA100	439028.176	9166315.200	2910.503
5	648.8	JRA9	439265.509	9167034.188	2699.309
6	1210.2	JRA6	439539.879	9167523.988	2551.654
7	1812.2	KLAK	437372.090	9167353.043	1924.344
8	2151.5	SELO	439486.574	9168550.110	2045.780
9	2803.2	JRA1	439616.761	9169189.224	1810.590
10	3070.5	KEND	440284.748	9163699.632	1469.757
11	4141.1	GMRR	434827.574	9166099.182	1266.923
12	4266.3	BABA	434984.170	9168032.665	1304.214
13	5242.9	MRIY	444167.534	9165927.230	1208.900
14	5514.9	JRA0	436176.438	9171231.310	1318.130
15	7104.0	KALI	436584.977	9159767.987	878.695
16	7519.6	CEPO	445514.541	9170137.637	1033.781
17	18163.5	BOYO	457093.430	9165563.077	390.740
18	24242.6	KLAT	453043.566	9146739.300	190.197
19	28313.5	BUTU	412663.263	9155952.170	648.854
20	29275.8	MVOY	432125.132	9137997.341	139.467

Table 6.3: Observation points used for the modeling.

no.	dg [mGal]	σ_{dg} [mGal]	uz [cm]	σ_{uz} [cm]	ux [cm]	σ_{ux} [cm]	uy [cm]	σ_{uy} [cm]
1	0.149	0.017	25.7	1.8	6.2	0.4	-18.6	0.4
2	0.004	0.017	-8.1	1.8	21.9	0.4	4.7	1.5
3	-0.033	0.017	-11.5	1.8	17.8	0.7	58.4	0.8
4	0.107	0.019	-7.8	1.9	16.1	0.5	-7.7	0.4
5	-0.021	0.016	-10.3	2.0	-1.3	0.7	-0.3	0.5
6	-0.026	0.015	-6.9	2.3	-3.3	0.6	-0.7	0.5
7	0.049	0.012	1.0	1.8	-1.1	0.3	0.8	0.3
8	-0.043	0.012	-1.6	2.3	0.0	0.4	0.6	0.4
9	-0.032	0.011	-2.8	3.1	-1.9	0.8	-0.5	0.7
10	0.007	0.009	-3.6	2.3	-0.6	0.4	0.7	0.3
11	-0.048	0.008	0.0	1.9	0.2	0.3	0.2	1.2
12	-0.002	0.008	-0.1	2.1	-0.3	0.4	-0.2	0.4
13	-0.016	0.009	-0.9	3.7	2.2	0.5	0.9	0.5
14	-0.018	0.008	-2.8	2.0	-0.3	0.3	-3.2	0.3
15	-0.008	0.005	-0.7	2.6	-0.2	0.4	1.9	0.3
16	-0.006	0.007	5.7	3.0	0.6	0.5	0.7	0.4
17	0.007	0.006	6.7	5.8	1.5	0.9	0.3	0.7
18	0.011	0.004	-0.6	4.9	1.7	0.8	-0.1	0.6
19	-0.011	0.006	2.1	2.0	-3.2	0.3	-1.8	0.3
20	0.000	0.001	-0.1	2.0	0.1	0.3	0.1	0.3

Table 6.4: Observation changes of the points between epoch 2000 and 2002 including standard deviations.

with $\mathbf{l}$ = observed value, $\mathbf{Q_{ll}}$ = cofactor matrix, r = degrees of freedom, α = significance level and H_0-hypothesis: $E(\mathbf{l}) = 0$. For $\alpha = 0.05$ and degrees of freedom $r_g = 2599$ for gravity observations, the inverse of the Student's cumulative distribution function $F(t, 2599, 0.95)$ results in a value of 1.645; for $r_{GPS} = 407$ the inverse results in a value of 1.649 for the GPS observations. The significant observations verified by the t-test are given in Table 6.5. The locations of these points are given in Figure 6.5. These results show that most of the significant observations, especially concerning the height changes uz, were only measured near the crater rim; with increasing distance to the top of the volcano, the displacements and gravity changes are getting less significant.

Observation	Significant value in point no.
dg	1, 3, 4, 6, 7, 8, 9, 11, 13, 14, 18, 19
uz	1, 2, 3, 4, 5, 6, 16
ux	1, 2, 3, 4, 5, 6, 7, 9, 10, 13, 17, 18, 19
uy	1, 2, 3, 4, 7, 8, 10, 13, 14, 15, 16, 19

Table 6.5: Significance of observed gravity changes and displacements between 2000 and 2002, using t-test.

6.2.2 Density Model

A density model had been generated by inversion of 443 gravity observations; at each point gravity and GPS had been measured. The three-dimensional inversion technique is based on a growing process of bodies according to CAMACHO *et al.* (2000), CAMACHO *et al.* (2002) and described in TIEDE *et al.* (2005a). An exploratory approach permits the construction of the anomalous bodies as step-by-step aggregation of prismatic cells, in which the gravity attraction of each cell is computed. The mean density has been determined by a least squares adjustment with a value of 2242 ± 29 kg/m^3.

The inversion shows areas with clear positive (Figure 6.7) or respectively negative (Figure 6.8) density contrasts in the region of Merapi and Merbabu. Positive as well as negative bodies are shown in Figure 6.9 and are referenced to the mean density of 2242 kg/m^3. The inversion of the gravity data produces a three-dimensional model with the geometrical distribution of anomalous structures with prior adopted density contrasts between -300 kg/m^3 and 300 kg/m^3 and resulting mean anomalous densities of -242 kg/m^3 and 262 kg/m^3. 19972 cells have been computed, whereby 3881 cells were filled with negative density contrast (Δm=-7.64·10^{14} kg) and 5319 cells were filled with positive density (Δm=+1.31·10^{15} kg).

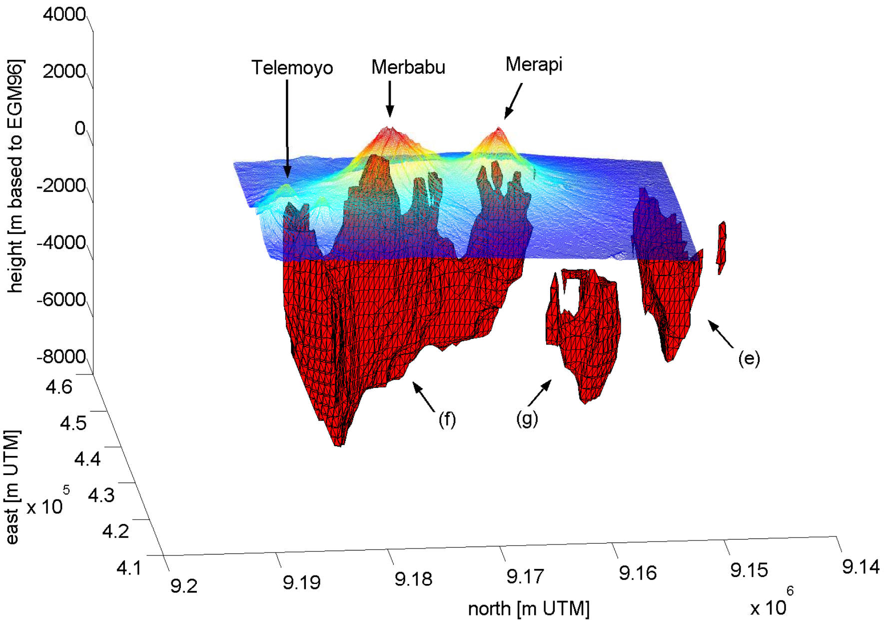

Figure 6.7: Positive density anomalies ≥ 200 kg/m^3.

The fit of the model is given by the histogram showing the residuals **v**, Figure 6.10 and the weighted root mean square (rms). The posterior rms is 0.046 mGal, compared to a prior rms about 0.504 mGal. The following list gives the most interesting areas described by the letters (a) to (g) with the resulting large anomalous density contrasts, see Figure 6.7, Figure 6.8 and Figure 6.9. Coordinates of their expansion are based on UTM and the depth on EGM96 geoid.

- (a) Body with a low density contrast: East (417000-434500 m), north (9162000-9176500 m), depth between -9000 and 0 m, the two-dimensional location is in agreement with the high conductive body (E) found by magnetotellurics, Figure 6.4.

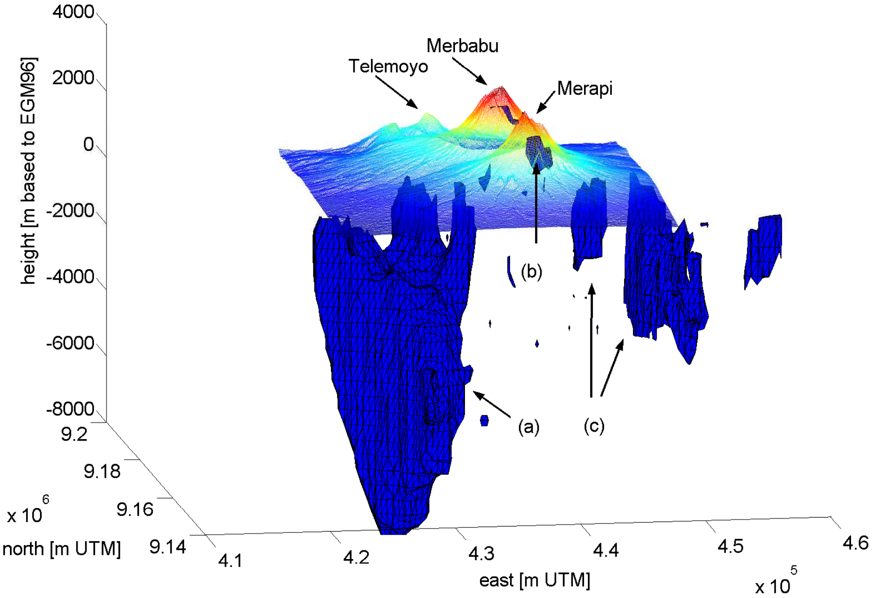

Figure 6.8: Negative density anomalies ≤ -200 kg/m^3.

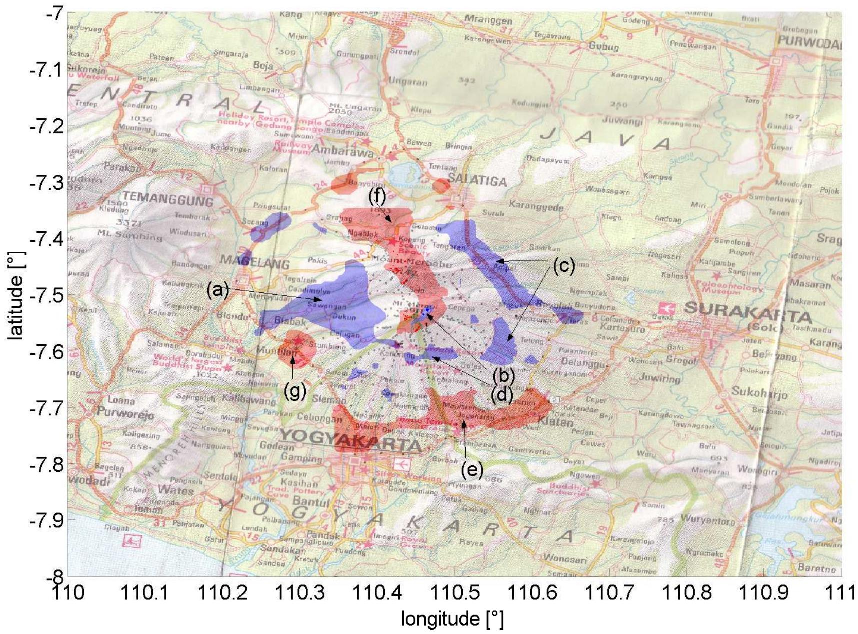

Figure 6.9: Position of density anomalies around Merapi and Merbabu. Negative density anomalies ≤ -200 kg/m^3 are shown in blue. Positive density anomalies ≥ +200 kg/m^3 are shown in red. Points give position of gravity points

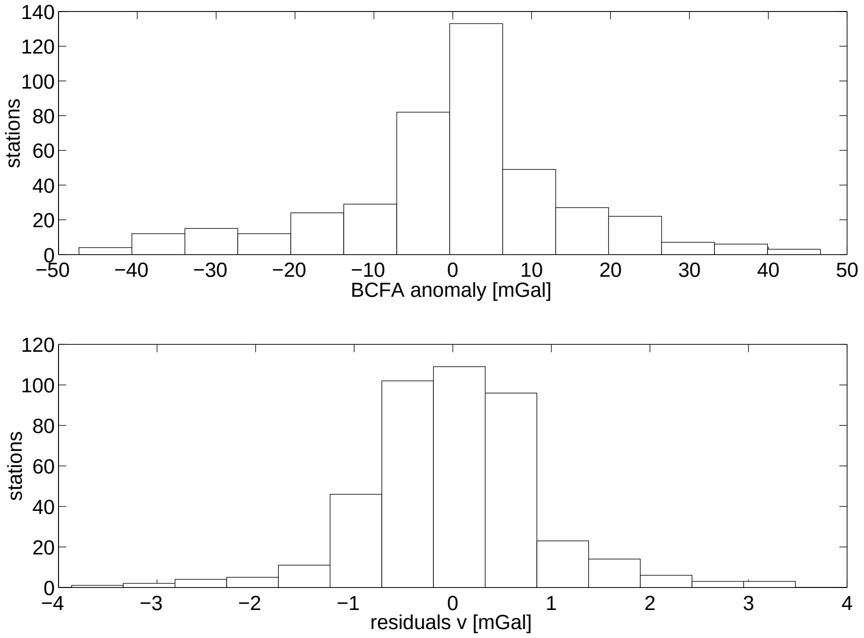

Figure 6.10: Histogram showing the prior distribution of Bouguer corrected gravity anomalies and the posterior residuals **v** resulting from the modeling.

- (b) Low density body below Merapi at a depth of approximately +1100 to +2100 m. East (439000-441500 m) and north (9165500-9168500 m). The body coincides in east as well as north coordinate with the results according to Müller and Haak (2004), body (D) in Figure 6.4, whereby the height is determined more shallow for this body by the gravity inversion.

- (c) Low density bodies east of Merapi arranged in an arc with a concave shape to Merapi. East (444500-454000 m), north (9157000-9185500 m), depth between -6000 and 0 m . It is touching an area of negative Bouguer corrected free air anomalies, which are equivalent to low densities, described in Untung and Sato (1978).

- (d) Small low density body with WE extension southwards of Merapi in a distance of about 8000 m, striking from west to east. East (438000-445000 m), north (9157000-9160500 m), depth between -4000 and -1500 m. This body coincides in its location with the high conductive body found by LOTEM observations, Müller *et al.* (2002), Kalscheuer (2004) and NanoTEM Koch (2003). The large depth extension of the body would confirm the anticipation of a vertical fault structure, anticipated in Kalscheuer (2004) and Commer *et al.* (2005) to explain the LOTEM measurements whereby former LOTEM models do not take this fault structure into account and result in vertical extention of conductivity of only a few hundred meters.

- (e) Positive density contrast chain. East (428000-460000 m), north (9140000-9153000 m) and a depth between -6000 and 0 m. The location of the high density chain can be correlated with a longitudinal fault system which is originating between the Solo zone and the Southern Mountains as well as with a part of the central depression zone of Java, Bemmelen (1949). Furthermore, this region covers also the Jiwo Hills, a fossiliferous marine bed, discordantly overlying strongly folded pre-Tertiary schists.

- (f) Arc along volcanoes with a positive density contrast: East (429000-444000 m), north (9167000-9188000 m), depth between -7000 and +2000 m showing the connection of the volcanoes and the continuation of the NS striking transverse fault zone which is stated by BEMMELEN (1949). This connection of the volcanoes Merapi, Merbabu and Telemoyo in the north underlines the historical development of the volcanoes. The morphology given by the adjusted model suggests an intrusive fissural complex starting from the large positive body on the NW border, and running with direction 152°N towards SE across the volcanoes and with a mean depth of -2000 m. Across the elongated body several transversal nodes are identified shallower, for instance that connecting the main course with the location of Merapi in a SE margin.

- (g) Positive density contrast, east (418500-425000 m), north (9156000-9163500 m) and a depth between -4000 m and 0 m in the region where the Gendol hills are located. These hills are described as the folded foot of the old Merapi, BEMMELEN (1949).

Generally porosity values derived from the density contrasts are about 21% for the bodies (a)-(d): To compute a porosity value for these bodies, the pores are filled completely with saline fluids of a density of 1090 kg/m^3. Such high porosities for the whole volcanic region are also assumed for gravity modeling SETIAWAN (2002).

6.3 Application of Uncertainty and Sensitivity Analysis

In this Chapter two different analyses are carried out, both consisting of an uncertainty as well as a sensitivity analysis. The uncertainty and sensitivity analysis is computed with the software GLUEWIN which can operate together with Simlab, version 2.2, SALTELLI *et al.* (2004). The computation is investigated for the $1/\chi()^2$ output values computed by observed and modeled gravity changes $1/\chi(dg)^2$, height $1/\chi(uz)^2$, east $1/\chi(ux)^2$ and north $1/\chi(uy)^2$ displacements as well as for the $1/\chi(comp)^2$ value which is computed over all observations. Likelihoods for the analyses are given by $1/\chi(comp)^2$ values.

Generally two different kind of uncertainty combined with sensitivity analyses are investigated in this study:

- Bayesian uncertainty combined with a Sobol' sensitivity analysis, described in Chapter 4.2.1. To avoid time consuming computation expenses the input sample set is required to be orthogonal, SALTELLI *et al.* (2000), SALTELLI *et al.* (2004). A Monte Carlo sampling over the defined range of the unknown input parameters has been investigated.

- Uncertainty analysis with RSA, described in Chapter 4.2.2. Due to the reason that the orthogonal Monte Carlo sample set does not fit the optimum of the multimodal objective functions, a second sampling approach has been investigated which is related to filter techniques. The purpose of that computation has been, to compute the samples in more likely regions, with larger values of $1/\chi()^2$ respectively.

For both computations of input samples the ranges for the unknown input parameters have been chosen according to Table 6.6. They are anticipated according to initial results of a genetic algorithm optimization, TIEDE *et al.* (2004) where the ranges had been so large that the computed results do not reach the limits. Furthermore, the following information is implied in the choice of the ranges:

Parameter	lower bound	upper bound
$\xi[10^3$ m$]$	435	441
$\psi[10^3$ m$]$	9160	9170
$\zeta[10^3$ m$]$	0.01	3
$p[10^5$ Pa$]$	-10	100
$r[10^3$ m$]$	0.001	2
$m[10^{12}$ kg$]$	-1	2

Table 6.6: Parameter limits for the uncertainty and sensitivity analysis.

According to Chapter 6.1, Merapi is said to be an open low pressure system, so the limitation range for the pressure p is set to $p \leq 100 \cdot 10^5$ Pa.

By analyzing the results of active seismic measurements, Chapter 6.1, an a-seismic zone at an approximate depth of about 1500 - 2500 m below the summit is stated to be a probable magma chamber.

Two different magmatic source models taken from the literature whose location, mass and radius components were computed by BEAUDUCEL and CORNET (1999) are tested in order to verify the ranges of the unknown parameters. The values of the first model were computed by a forward modeling approach, anticipating a Mogi point source, MOGI (1958) in an elastic half-space, and the second values for a sphere source using a mixed boundary element model approach. Both models are results of an inversion of GPS and tilt data. The necessary mass and radius component for the computation of the elastic-gravitational model were determined by the given volume changes, anticipating a mean density of 2242 kg/m^3, Chapter 6.2.2. The pressure has been anticipated as $100 \cdot 10^5$ Pa. The parameters of the two described sources are summarized in Table 6.7. The layer thickness is anticipated as 8000 m. The Lamé parameters for the layer and the underlying homogeneous half-space are computed via the Young-modulus E which is anticipated as 30 GPa, Beauducel *et al.* (2000) and the Poisson ratio $\nu = 0.25$ for an elastic material. E and ν are converted into λ and μ with

source parameter	Mogi point source	sphere source
ξ ref. to summit [10^3m]	4.4	2
ψ ref. to summit [10^3m]	0.4	0
ζ [10^3m]	9	6
p [10^5 Pa]	100	100
r [10^3m]	0.18	0.14
m [10^{12}kg]	-0.05	-0.02
$p \cdot r^3$ [$10^{14} N \cdot m$]	0.5832	0.2744
$1/\chi(comp)^2$	0.00520	0.00520
T(80,74)	10839.64048	18200.62075

Table 6.7: Parameters of the two anticipated sources.

$$\lambda = \frac{E \cdot \nu}{(1+\nu)(1-2\nu)} \tag{6.3}$$

$$\mu = \frac{E}{2(1+\nu)} \tag{6.4}$$

The assimilation of these models to the observed data are given by applying Fisher's F-test. The H_0-hypothesis states that the variance of the modeled values is equal to the variance of the observed ones.

$$T = \frac{\mathbf{v1}^T \mathbf{Q_{ll}}^{-1} \mathbf{v1} \cdot r2}{\mathbf{v2}^T \mathbf{Q_{ll}}^{-1} \mathbf{v2} \cdot r1} \sim F(1-\alpha, r1, r2) \tag{6.5}$$

with $r1, r2$ = degrees of freedom of $\mathbf{v1}, \mathbf{v2}$, $\mathbf{Q_{ll}}$ = cofactor matrix. $\mathbf{v1}$ and $\mathbf{v2}$ indicate the modeled and observed values respectively, whereby the larger squared sum is set as numerator.

The results show that the assimilation of these models to the observed data in gravity change as well as to vertical and horizontal displacement in east and north component is quite bad, which is reflected by the results of the F-test
$T_{model1} = 10839.64048 > F(0.9999, 80, 74) = 2.38549$,
$T_{model2} = 18200.62075 > F(0.9999, 80, 74) = 2.38549$
respectively, see Figure 6.11, Figure 6.12. Both models fail to fit the observed values. More valuable results can be determined by increasing the pressure which leads to values that are not physical reliable any more. The decreasing of the source's depth results in an increasing fitness of the model and reflects more reliable values than the increase in pressure, so the limitation of the depth component of the unknown source is set shallow as proposed by Ratdomopurbo and Poupinet (2000).

Initial results of the genetic algorithm optimization for the observed gravity changes, vertical and horizontal displacements show a mass component of the unknown source which is very small with only a small dispersion of the value, Tiede *et al.* (2004). According to these results, the limitation of the mass was set to small values which is also confirmed by an approximation of the anomalous mass,

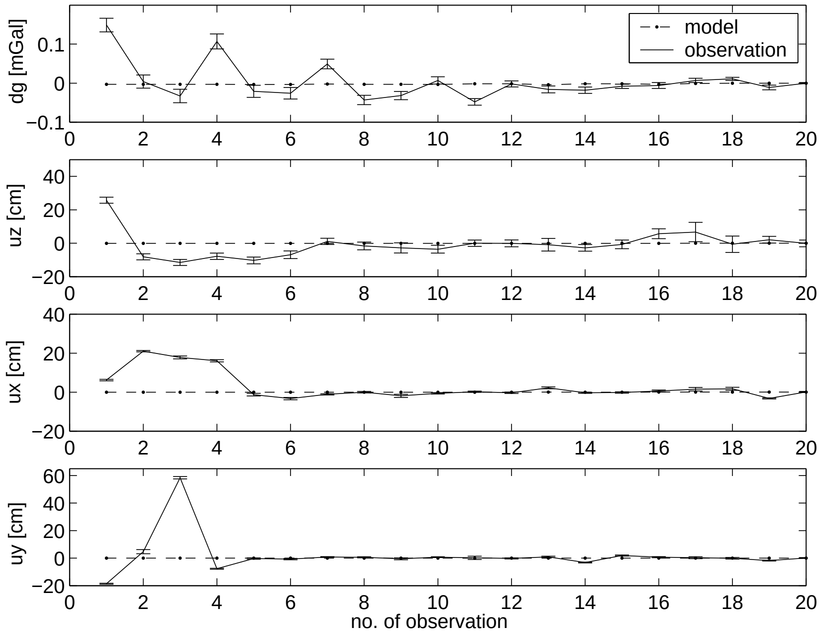

Figure 6.11: Modeled (Mogi source) and observed gravity changes dg, vertical displacements uz and horizontal displacements ux and uy with 1σ-error bars.

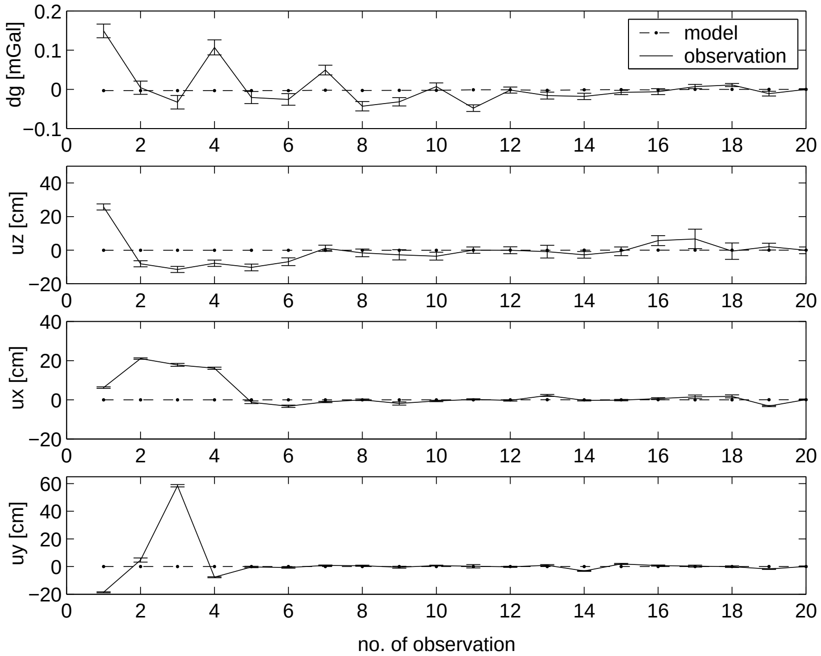

Figure 6.12: Modeled (sphere source) and observed gravity changes dg, vertical displacements uz and horizontal displacements ux and uy with 1σ-error bars.

Chapter 6.2.1, Table 6.2. The shallow depth of the magma chamber as well as the pressure are also set with respect to former modelings by KÖRNER (2000), who anticipated shallow chambers within a depth smaller than 500 m, and vertical extensions between 100-200 m as well as horizontal extensions between 200-600 m, and a pressure between $30 - 40 \cdot 10^5$ Pa. Anticipating the radius $r = 275$ m and by expressing these chambers as an energy form $p \cdot r^3$ would result in values smaller than $0.624 - 0.832 \cdot 10^{14}$kg·m^2/sec^2.

Two sets of samples are used to determine both, the uncertainty in the model predictions and the unknown input parameters, that give rise to the uncertainty in a global sensitivity analysis.

The variance-based Sobol' sensitivity analysis is determined separately for the $1/\chi(dg)^2$, $1/\chi(uz)^2$, $1/\chi(ux)^2$, $1/\chi(uy)^2$ and $1/\chi(comp)^2$ values. Note: The objective functions are computed by the kind of observation which is given in brackets. The RSA sensitivity analysis is only computed for $1/\chi(comp)^2$ values.

By performing the Sobol' sensitivity analysis to the $1/\chi()^2$ values, the unknown input parameters which mainly drive the model's behavior are identified. The RSA serves for the determination if the sensitivity of $1/\chi(comp)^2$ behaves differently concerning changes in the unknown input parameters if the fitness of the models is increasing.

6.3.1 Bayesian Uncertainty and Sobol' Sensitivity Analysis

The first set of input parameters is computed by a Monte Carlo sampling approach, generating orthogonal samples. The orthogonality is required in order to apply the global variance-based sensitivity analysis, described in Chapter 4.2.1. Table 6.8 displays the correlation matrix of the unknown input parameter samples where the required orthogonality becomes obvious. The pdfs of the unknown input parameters had been anticipated as uniform because it has not been possible to specify any areas or certain value ranges which are more likely than others within the given limits for the unknown input parameters. Furthermore, in cases with only poor prior knowledge of the unknown input parameters pdfs, Saltelli *et al.* (2000) also suggests a unique distribution.

ξ	1	-0.0018	-0.0020	-0.0010	-0.0013	-0.0016
ψ		1	-0.0013	-0.0015	-0.0016	-0.0012
ζ			1	-0.0022	-0.0011	-0.0005
p				1	-0.0017	-0.0019
r					1	-0.0011
m						1
	ξ	ψ	ζ	p	r	m

Table 6.8: Correlation coefficients between the unknown input parameters of the 28672 Monte Carlo samples.

Likelihoods for the modeled output values are given by the $1/\chi(comp)^2$ values. The generated Monte Carlo samples serve as the input of the Bayesian uncertainty and the Sobol' sensitivity analysis. Their posterior distributions are given in Figure 6.13 to Figure 6.15, whereby the prior distributions are indicated by the straight line and reflect the uniform distributed Monte Carlo sampling. The posterior distributions of the input parameters are computed with respect to the likelihood $1/\chi(comp)^2$ and applying Bayes theorem, Equation 4.1. The comparison of the prior and the posterior distribution of the sample sets shows the influence of $1/\chi(comp)^2$, so for each unknown parameter certain regions can be defined for which the fitness is larger if the unknown parameter is lying in between these regions. Analyzing these changes for the east component, a less likely region can be

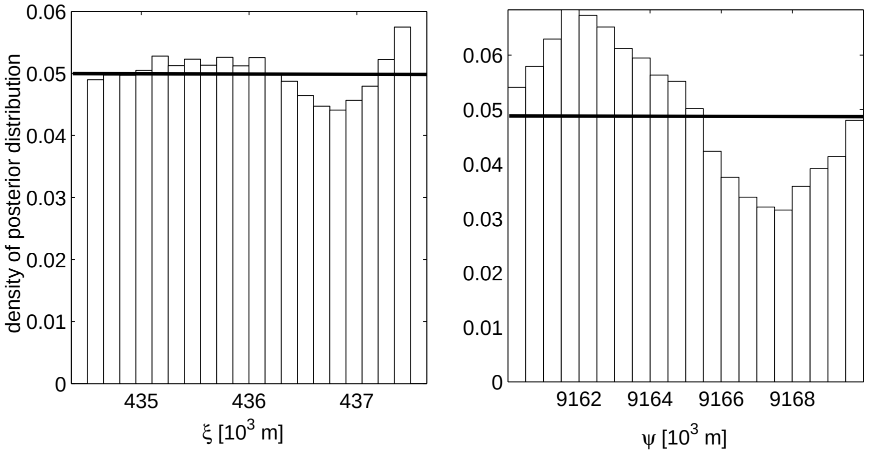

Figure 6.13: Posterior distributions of ξ and ψ, generated by 28672 Monte Carlo samples, anticipating the likelihoods given by $1/\chi(comp)^2$.

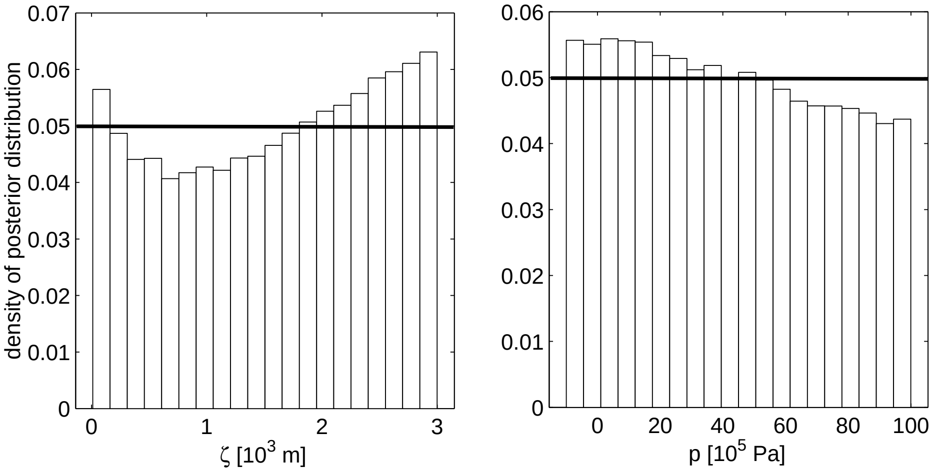

Figure 6.14: Posterior distributions of ζ and p, generated by 28672 Monte Carlo samples, anticipating the likelihoods given by $1/\chi(comp)^2$.

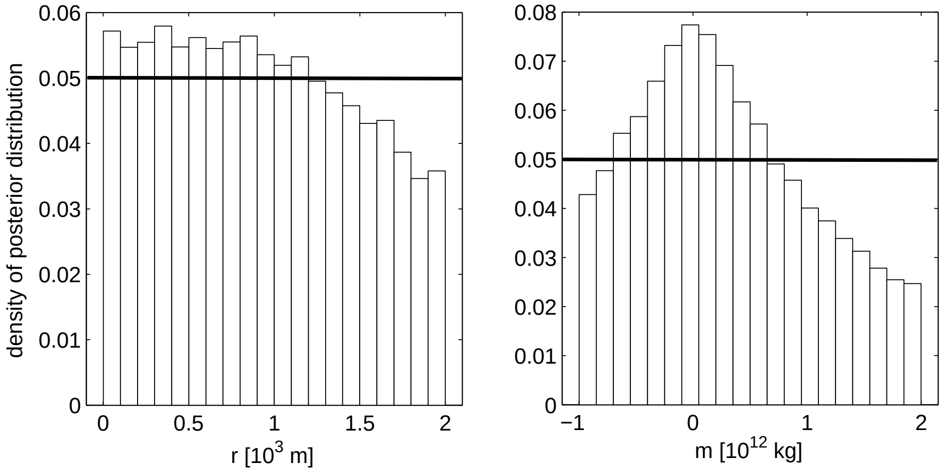

Figure 6.15: Posterior distributions of r and m, generated by 28672 Monte Carlo samples, anticipating the likelihoods given by $1/\chi(comp)^2$.

determined for $439 \cdot 10^3 \leq \xi \leq 440.5 \cdot 10^3$ m coordinates, while east components which are located $440.5 \cdot 10^3 \leq \xi \leq 441 \cdot 10^3$ m are more likely. Nevertheless, the changes between prior and posterior distribution are small. The distribution for the north component of the samples is changing drastically, so the uncertainty concerning samples with $9161 \cdot 10^3 \leq \psi \leq 9165 \cdot 10^3$ m is decreasing, whereby it increases for $9165 \cdot 10^3 \leq \psi \leq 9170 \cdot 10^3$ m. The posterior distribution of the depth is decreasing for the region of $200 \leq \zeta \leq 1800$ m, otherwise it is increasing. The posterior distribution of the pressure component shows no significant change to the prior one, so applying Bayesian theory does not result in a significant different distribution and the $1/\chi(comp)^2$ output values are not sensitive against changes in the pressure component. The posterior distribution of the radius component shows a slightly increase for smaller radius values and a decrease for larger radius components. The posterior distribution of the mass component is changing most due to applying Bayes theorem. Models with mass values around 0 kg are more likely to produce large $1/\chi(comp)^2$ values whereby the increase of the absolute mass value results in smaller likelihoods. Summarizing these results, it becomes obvious, that on the one hand the uncertainty could not be reduced for the pressure and also only slightly for the radius component by the Bayesian approach. These two components are difficult to determine due to the small change in fitness of the output models when varying the pressure p and radius r together. On the other hand, the mass component m is very good to determine.

From these plots, first assumptions of the relation between the input parameters and the fitness of the corresponding models could be drawn. Furthermore, the changes between the prior and posterior distribution have been also generated in order to validate the second sampling approach, see Chapter 6.3.2 and to compare, if the more likely areas of the unknown input parameters change with increasing the fitness of the models.

Figure 6.16 to Figure 6.20 show the output values $1/\chi(dg)^2$, $1/\chi(uz)^2$, $1/\chi(ux)^2$ and $1/\chi(uy)^2$ concerning gravity, height, east and north observations as well as $1/\chi(comp)^2$ plotted against each of the unknown input parameter of the sample set. From these plots, possible correlations between the output and the input parameters can be evaluated. The main sensitivity effects can be determined in these plots. They are given by an obvious relation between the unknown input parameter and the output value (for a large sensitivity see Figure 6.16 for the mass component). Furthermore, the plots give an excellent overview about the distribution of the estimated model output with respect to each unknown input parameter:

- For $1/\chi(dg)^2$ no relation concerning its values and the location of the unknown input parameters except the mass component m can be seen. Large $1/\chi(dg)^2$ values can be determined for small m around 0 kg. The shape of the area where most of the $1/\chi(dg)^2$ are lying shows a symmetrical behavior concerning the y-axis. The steep gradients of the shape around 0 kg, as well as the small dispersion of $1/\chi(dg)^2$ in relation to changes in m, indicates a high sensitivity of the $1/\chi(dg)^2$ against changes in m.

- $1/\chi(uz)^2$ shows only a small relation between its values and changes in east ξ, depth ζ, pressure p and mass m. The analysis of the relation between $1/\chi(uz)^2$ and the north component ψ results in a region $9150 \cdot 10^3 \leq \psi \leq 9160 \cdot 10^3$ m for which the output values show a smaller dispersion. This small dispersion is equivalent with a higher sensitivity against changes in ψ. The same effect occurs for small values of the radius r.

- Analyzing the distribution of $1/\chi(ux)^2$, high values can be observed for east components ξ $439 \cdot 10^3 \leq \xi \leq 440 \cdot 10^3$ m as well as one more diffuse region around $438 \cdot 10^3$ m. A clear region of the north component psi for large $1/\chi(ux)^2$ can be figured out (around $9165 \cdot 10^3$ m). Concerning the depth component ζ larger $1/\chi(ux)^2$ are given by smaller ζ values. $1/\chi(ux)^2$ shows small values for small radius components r but within a very small dispersion which demonstrate a higher sensitivity. The dispersion is increasing with enlarging r. The mass component m does not influence the distribution at all.

- The distribution of $1/\chi(uy)^2$ shows high sensitivity concerning changes in the radius component r because for small r a very small dispersion of $1/\chi(uy)^2$ is given. Small pressure components p result in a small dispersion of the output value whereby this effect is very local. Relations between $1/\chi(uy)^2$ and east ξ, north ψ and mass m cannot be figured out.

- The $1/\chi(comp)^2$ can be seen as the sum of the four previous described plots. The mentioned effects are overlapping, so no clear behavior can be figured out by analyzing this plot. Nevertheless, a slightly increased sensitivity concerning changes in north ψ and mass m are given, whereby a detailed analysis of the relation between unknown input parameters and $1/\chi(comp)^2$ can be drawn out by combining the information of Figure 6.20 with Figure 6.13 to Figure 6.15.

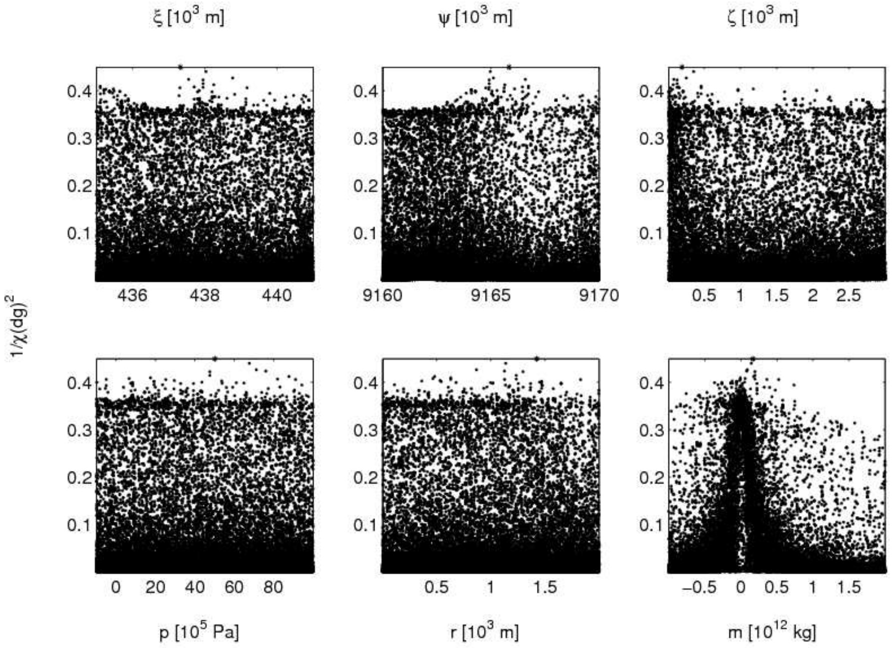

Figure 6.16: $1/\chi(dg)^2$ distribution relative to the samples of the Monte Carlo sampling with a range of $5.33710^{-8} \leq 1/\chi(dg)^2 \leq 0.4492$.

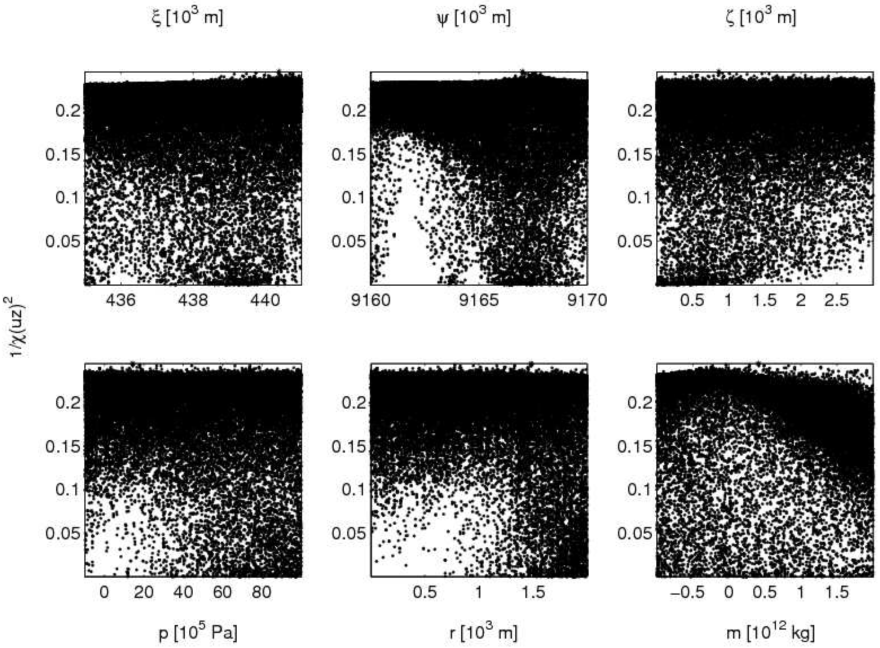

Figure 6.17: $1/\chi(uz)^2$ distribution relative to the samples of the Monte Carlo sampling with a range of $4.50810^{-6} \leq 1/\chi(uz)^2 \leq 0.2433$.

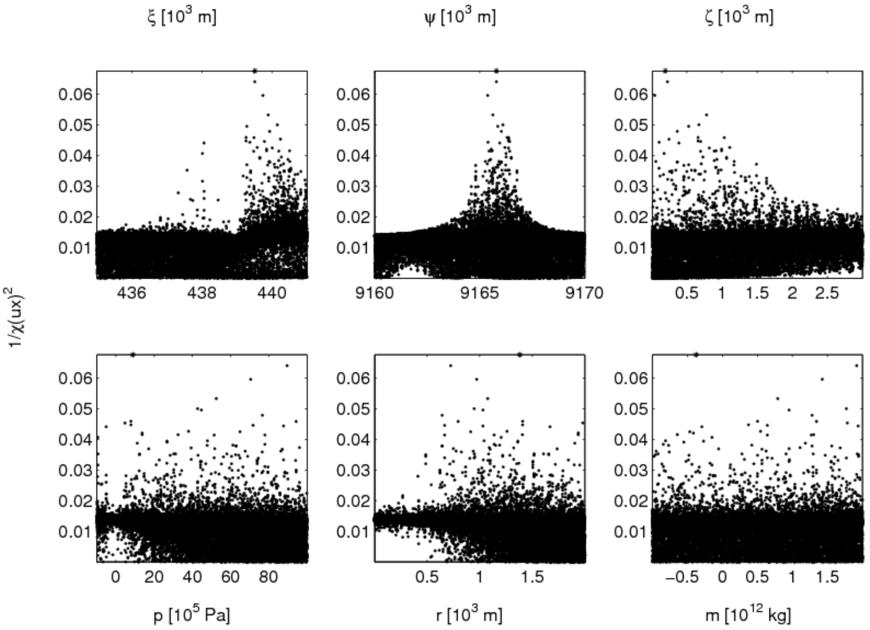

Figure 6.18: $1/\chi(ux)^2$ distribution relative to the samples of the Monte Carlo sampling with a range of $2.31310^{-8} \leq 1/\chi(ux)^2 \leq 0.06759$.

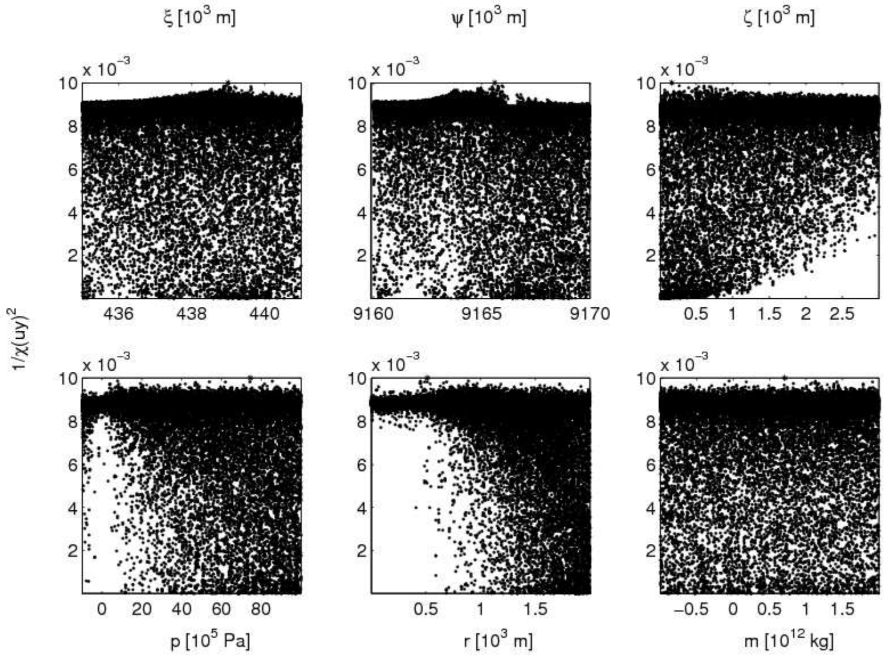

Figure 6.19: $1/\chi(uy)^2$ distribution relative to the samples of the Monte Carlo sampling with a range of $1.710^{-7} \leq 1/\chi(uy)^2 \leq 0.01002$.

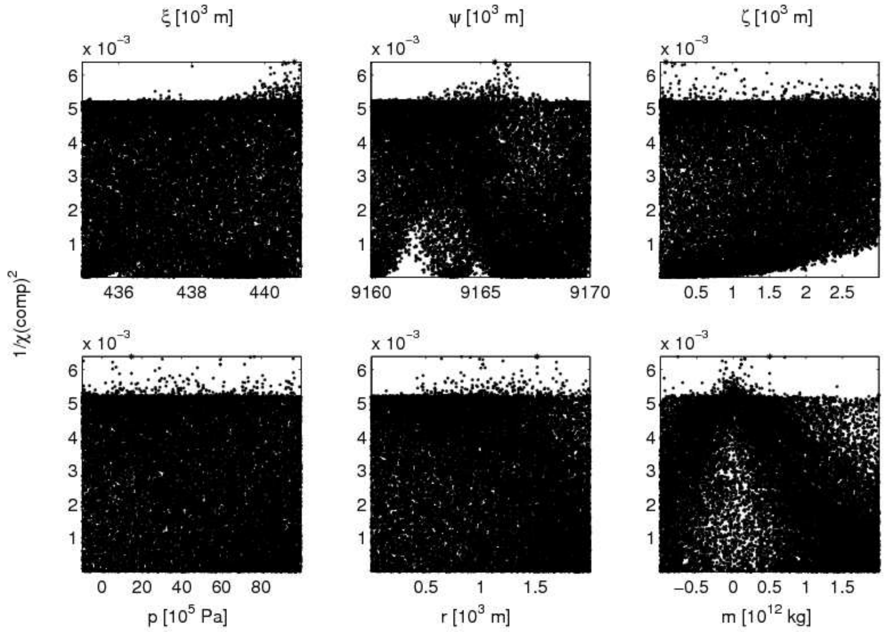

Figure 6.20: $1/\chi(comp)^2$ distribution relative to the samples of the Monte Carlo sampling with a range of $2.1910^{-8} \leq 1/\chi(comp)^2 \leq 0.006387$.

By analyzing Figure 6.20, it becomes obvious that the Monte Carlo samples do not reflect as high fitness results as given by the initial GA results, Tiede *et al.* (2004). The plots show that the generation of a realistic estimation of a predictive uncertainty for the region where the optimal models lie cannot be evaluated with this kind of sampling.

Therefore, it has to be kept in mind that the following sensitivity analysis reflects the results for the samples which are built by uniformly distributed input parameters over the whole definition range. This configuration of sensitivity analysis is chosen due to the poor prior knowledge of the region in which the unknown input parameters lie. The TSIs concerning all unknown input parameters are evaluated, anticipating the same limits for the unknown input parameters as in the optimization approaches, Chapter 6.4.

In a further sensitivity analysis a second approach is investigated with the main focus on high fit regions, Chapter 6.3.2. This analysis is computed in order to evaluate if the sensitivity is changing for samples with a high fitness compared to the sensitivity which is given by the Monte Carlo sampling set.

The previous discussed results show first relations between unknown input parameters and the output values and will be analyzed in more detail by applying the Sobol' variance-based sensitivity analysis. Therefore, the first order effects as well as the TSIs are computed after Chapter 4.2.1 for all five outputs and visualized in a comparison in Figure 6.21. Analyzing the differences between the first order effects and the TSIs, it can be seen that the model includes higher order effects. This underlines the need of incorporating the TSIs and not only the first order effects into every analysis of the sensitivity. Furthermore, the first order effects confirm the described results in Figure 6.16 to Figure 6.20.

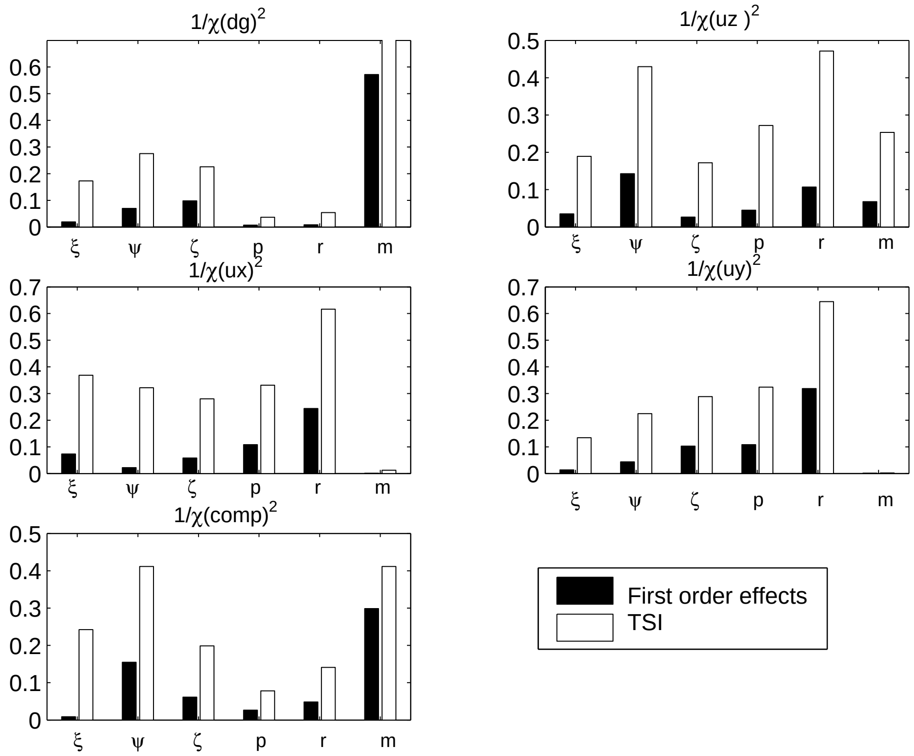

Figure 6.21: First order effects and TSIs computed by Sobol' sensitivity analysis for the Monte Carlo sampling.

Figure 6.22 displays a larger insight in the interactions of the unknown parameters comparing the closed second order effects according to Chapter 4.2.1 to the second order effects, whereby the input parameters are abbreviated in the following way: 1=ξ, 2=ψ, 3=ζ, 4=p, 5=r, 6=m. (E.g. the second order index c12 describes the interaction between ξ and ψ).

Table 6.9 to Table 6.11 give the percentage of the first, the second and the higher order effects on the corresponding TSI, separately for each certain output value. By analyzing these tables, it is possible to interpret the TSIs according to dominating effects. Note: These tables cannot give any information about the absolute value of the TSIs. The intension is to give information about the percentual composition of each TSI.

Figure 6.23 displays the normalized first order effects with respect to the unknown input parameters for all kind of output values ($1/\chi(dg)^2$, $1/\chi(uz)^2$, $1/\chi(ux)^2$, $1/\chi(uy)^2$, $1/\chi(comp)^2$). Figure 6.24 shows the corresponding normalized TSIs. The normalization is investigated according to

$$S()_{n,i} \quad = \quad S()_i / \sum_{i=1}^{6} S()_i \tag{6.6}$$

$$TSI()_{n,i} \quad = \quad TSI()_i / \sum_{i=1}^{6} TSI()_i \tag{6.7}$$

with $S()_{n,i}$ = normalized first order sensitivity index of the values given in the brackets due to the specified unknown input parameter i, $S()_i$ = first order sensitivity index concerning the unknown input parameter i, $TSI()_{n,i}$ = normalized TSI sensitivity index, due to the unknown input parameter i and $TSI()_i$ = total sensitivity index due to the unknown input parameter i.

The obvious changes in sensitivity in Figure 6.23 and Figure 6.24 caused by higher order effects makes the use of a global sensitivity analysis very important. (E.g. $1/\chi(uz)^2$ is mainly influenced by the interactions between the unknown parameters, so only taking the first order effects into account would lead to wrong sensitivity anticipations.) Furthermore, these different sensitivities concerning the unknown input parameters of different kind of output values show that only the common inversion of gravity changes and displacements can lead to a reliable determination of the unknown input parameters. Considering only gravity changes would lead to a difficult determination of the radius and pressure component, whereby the mass component could not be estimated reliably by only taking displacements into account. By analyzing the normalized TSIs, Figure 6.24 it can also be determined which type of observed data should be used to compute each unknown parameter.

Note: Figure 6.22, Figure 6.23 and Figure 6.24 give absolute sensitivity information, whereby the composition of the normalized TSIs cannot be evaluated through these figures.

The following list summarizes all information which can be taken out of the previous described figures and tables, separately for each kind of observation.

- $1/\chi(dg)^2$:

  Only $TSI(dg)_m$ is dominated by the first order effect. All other $TSI(dg)_{\sim m}$ are dominated by effects which are higher than the second order. All second order effects are negligible. $1/\chi(dg)^2$ values show a small sensitivity concerning changes in p and r. The sensitivity of $1/\chi(dg)^2$ values are strongly dependent on changes in m.

- $1/\chi(uz)^2$:

  Largest first order effect is given concerning changes in ψ. The first order effect due to m is for $1/\chi(uz)^2$ much larger than for $1/\chi(ux)^2$ and $1/\chi(uy)^2$ whereby the first order effect due to changes in r is smaller for $1/\chi(uz)^2$ compared to $1/\chi(ux)^2$ and $1/\chi(uy)^2$. Second order effects exist between ψ and all other unknown input parameters as well as between $\zeta \Leftrightarrow r$, $p \Leftrightarrow r$, $\zeta \Leftrightarrow p$, $p \Leftrightarrow m$ as well as between $r \Leftrightarrow m$. The sensitivity concerning changes in r are mostly driven by second and higher order effects, whereby the second order effects are caused by the interactions between $r \Leftrightarrow \psi$, $r \Leftrightarrow p$, $r \Leftrightarrow m$. All $TSI(uz)$ are dominated by higher order effects. $1/\chi(uz)^2$ values are mostly sensitive to changes in ψ and r.

- $1/\chi(ux)^2$:

  The largest first order effect is caused by r. All $TSI(ux)$ are dominated by higher than the second order effects. $1/\chi(ux)^2$ values are mostly sensitive to changes in r. ξ, ψ, ζ and p have nearly equal influences. $1/\chi(ux)^2$ values are not sensitive against changes in m.

- $1/\chi(uy)^2$:

  ψ, ζ and p components show a high interaction of second order with the radius component. Due to the reason that the $1/\chi(uy)^2$ values are most sensitive concerning changes in r and that the sensitivity is dominated by first and second order effects, these mentioned interactions cause a main part of the sensitivity concerning changes in r. The $TSI(uy)_m$ is dominated by the first order effects. All other $TSI(uy)_{\sim m}$ are dominated by second and higher order effects. The $1/\chi(uy)^2$ values are not sensitive against changes in m.

- $1/\chi(comp)^2$:

  Only $TSI(comp)_m$ consists mainly of the first order effect. All other $TSI(comp)_{\sim m}$ are mainly built of second and higher order effects. $1/\chi(comp)^2$ values are mainly sensitive against changes in m and ψ and only less sensitive against changes in the r and p. This fact results in difficulties to determine these two last mentioned parameters by the computation of $1/\chi(comp)^2$.

To explain the high second order effect, which is given by the interaction between ξ and ψ, Figure 6.22, the configuration of the significant observation, computed in Chapter 6.2.1, Table 6.5 has been analyzed. Computing the correlation coefficient between ξ and ψ component by only anticipating the points at which all four kind of observations are significant, leads to a correlation coefficient of -0.9961. It can be anticipated that the high second order effect is related to the observation point arrangement of the significant observations. The high second order effect of r and p concerning $1/\chi(uz)^2$, $1/\chi(ux)^2$ and $1/\chi(uy)^2$ can be explained by the defined energy form given by $p \cdot r^3$ which is computed in the physical underlying model, see Chapter 2.1.

first order effect [%]	$1/\chi$ $(dg)^2$	$1/\chi$ $(uz)^2$	$1/\chi$ $(ux)^2$	$1/\chi$ $(uy)^2$	$1/\chi$ $(comp)^2$
ξ	11.11	18.42	19.89	10.10	3.67
ψ	25.21	33.21	6.76	19.37	37.65
ζ	43.46	15.49	20.84	35.62	30.82
p	18.77	16.50	32.61	33.37	33.99
r	14.84	22.68	39.54	49.40	34.28
m	78.31	26.71	6.87	61.20	72.61

Table 6.9: Percentage of the first order effects on the TSIs.

second order effect [%]	$1/\chi$ $(dg)^2$	$1/\chi$ $(uz)^2$	$1/\chi$ $(ux)^2$	$1/\chi$ $(uy)^2$	$1/\chi$ $(comp)^2$
ξ	<0.01	<0.01	10.32	<0.01	83.23
ψ	<0.01	34.83	27.12	58.56	59.34
ζ	0.00	23.45	<0.01	11.55	20.30
p	<0.01	47.34	0.00	36.60	31.13
r	0.00	36.26	7.90	34.37	49.42
m	<0.01	26.14	<0.01	<0.01	22.44

Table 6.10: Percentage of the second order effects on the TSIs.

higher order effect [%]	$1/\chi$ $(dg)^2$	$1/\chi$ $(uz)^2$	$1/\chi$ $(ux)^2$	$1/\chi$ $(uy)^2$	$1/\chi$ $(comp)^2$
ξ	88.89	81.58	69.79	89.90	13.10
ψ	74.79	31.96	66.12	22.07	3.01
η	56.54	61.06	79.16	52.83	48.88
p	81.23	36.16	67.39	30.03	34.88
r	85.16	41.06	52.56	16.23	16.30
m	21.69	47.15	93.13	38.80	4.95

Table 6.11: Percentage of the higher order effects on the TSIs.

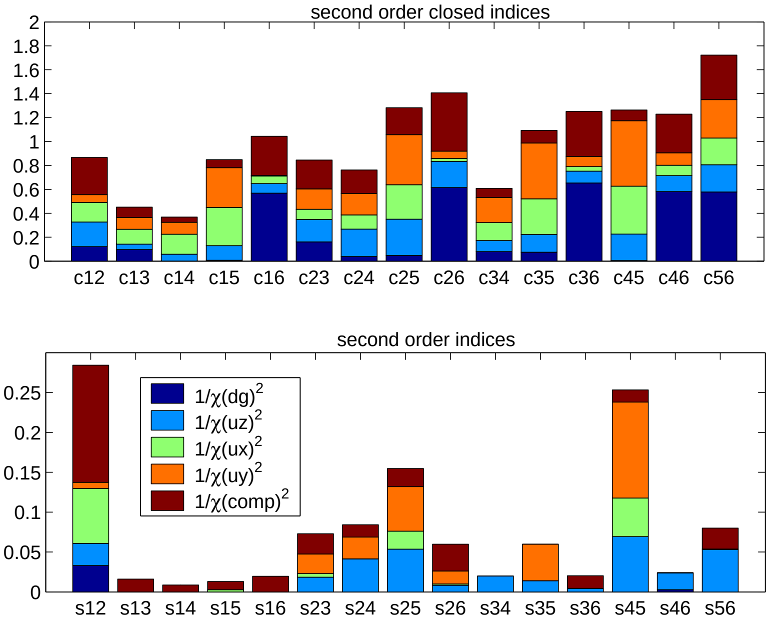

Figure 6.22: Closed second order and second order effects between the unknown input parameters determined by Sobol' sensitivity analysis for $1/\chi(dg)^2$, $1/\chi(uz)^2$, $1/\chi(ux)^2$, $1/\chi(uy)^2$, $1/\chi(comp)^2$.

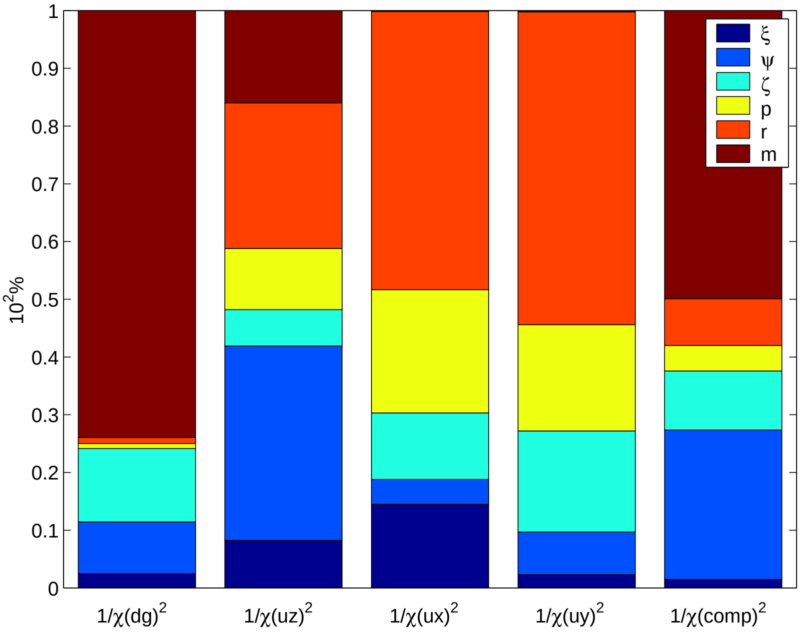

Figure 6.23: Normalized first order effects determined by Sobol' sensitivity analysis for $1/\chi(dg)^2$, $1/\chi(uz)^2$, $1/\chi(ux)^2$, $1/\chi(uy)^2$, $1/\chi(comp)^2$.

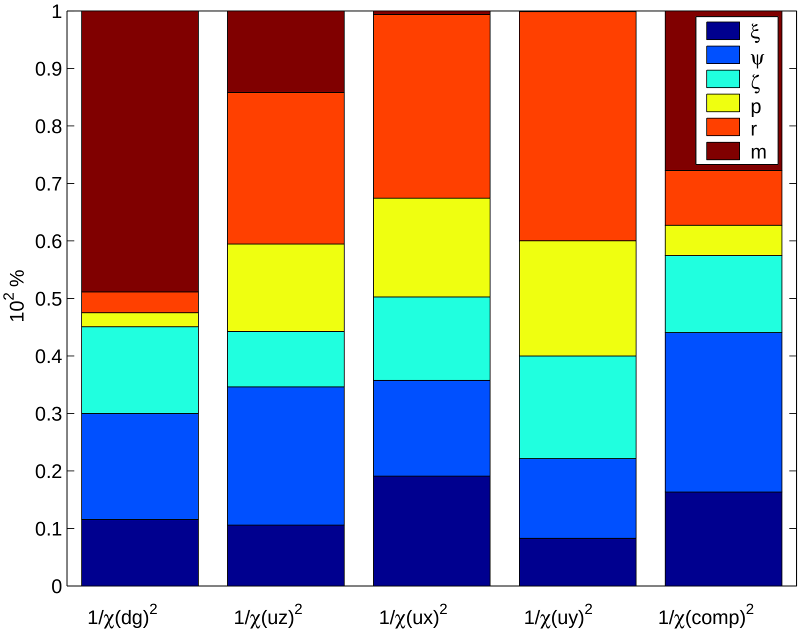

Figure 6.24: Normalized TSIs determined by Sobol' sensitivity analysis for $1/\chi(dg)^2$, $1/\chi(uz)^2$, $1/\chi(ux)^2$, $1/\chi(uy)^2$, $1/\chi(comp)^2$.

From the sensitivities analysis concerning all $1/\chi()^2$ values, conclusions about the computation of the unknown input parameters can be drawn:

- The mass component m is the unknown parameter which can be determined best. It can be computed most accurate by $1/\chi(dg)^2$, so the observations of gravity changes are most important for the determination of m. Furthermore, m would be the unknown which would lead to the highest variance reduction of $1/\chi(dg)^2$ and $1/\chi(comp)^2$ if it could be fixed.

- The radius component r is good to compute with $1/\chi(ux)^2$ and $1/\chi(uy)^2$ due to their large sensitivities against this unknown parameter.
- The north component ψ can be computed best by $1/\chi(uz)^2$.
- For the estimation of the pressure p the output values $1/\chi(uz)^2$, $1/\chi(ux)^2$ and $1/\chi(uy)^2$ are most appropriate.
- The east component ξ is computed most effectively by taking into account $1/\chi(ux)^2$.
- The depth component ζ is computed best by $1/\chi(dg)^2$ and $1/\chi(uy)^2$.

All the results which could be determined by the sensitivity analysis give a great insight into the underlying non-linear physical model as well as into the relation between observed data and unknown input parameters. Furthermore, the need of the common inversion for all types of observations becomes obvious due to the different sensitivities, because otherwise a completely wrong optimum could be determined via the optimization approach. Furthermore, small differences in sensitivities according to unknown input parameters, which cannot be seen immediately without applying a global sensitivity analysis were detected (e.g. varying sensitivities concerning the radius component). These determined $TSI()_r$ are used in order to improve the optimization computation of the unknown input parameters, see Chapter 5.2 and 6.4.

6.3.2 Uncertainty and Regionalized Sensitivity Analysis

This approach only includes the $1/\chi(comp)^2$ values because the purpose of the analysis is to determine if the sensitivity for the unknown parameters is changing for increasing fitness of the objective function. Therefore, a RSA is applied for three different samples which differ concerning their range of fitness.

For this approach the sampling had been repeated with respect to the regions where the fitness of the objective function is large. The new sampling approach is initialized by a starting point which is set in the middle of the limits given in Table 6.6 and with a randomly chosen offset from this values.

The sampling approach is comparable with a bootstrap algorithm by combining properties of genetic algorithm and simulated annealing: A certain number $i = 1...k$ of generations, consisting of a population with l members, is computed. The fittest samples of a generation are chosen in order to mutate them and generate new offsprings. Samples with a small fitness do not survive. A cooling schedule $t = t \cdot 0.9^{i-1}$ is causing a decrease of the randomly chosen variations of the values in each generation. These values are added to the values of the previous generation. The sampling approach generates, in regions where the fitness of the objective function is larger, more samples, so the sampling can reproduce better models with a larger fitness than the previously generated Monte Carlo sampling, Chapter 6.3.1.

For these sampling the likelihood of the samples is given by $1/\chi(comp)^2$. The distribution of the output value $1/\chi(comp)^2$ relative to the unknown input parameters is given by Figure 6.25. From this distribution it is obvious, that the sampling approach results in a sample set which is reflecting the region of large fitness. Furthermore, distinct regions can be detected in the distribution of the unknown input values which cause a better fit. The main drawback of this method is that the

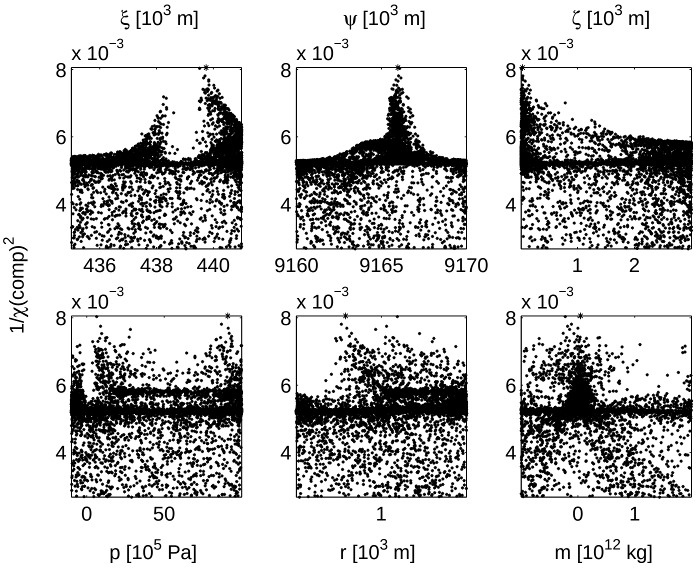

Figure 6.25: $1/\chi(comp)^2$ distribution relative to the samples of the filtering approach with a range of $0.00267 \leq 1/\chi(comp)^2 \leq 0.008061$.

filtered sampling set has no orthogonal behavior any more, which is expressed by the correlation matrix given in Table 6.12. The prior and posterior pdf of the input

ξ	1	-0.2446	-0.0397	0.2007	0.1685	-0.2112
ψ		1	0.1701	-0.1281	0.0151	0.1618
ζ			1	0.0604	0.1774	-0.0285
p				1	-0.3870	-0.0012
r					1	-0.0293
m						1
	ξ	ψ	ζ	p	r	m

Table 6.12: Correlation coefficients between the unknown input parameters of the 7168 samples computed with the filtering approach.

sample set are given in histograms by anticipating the likelihoods of $1/\chi(comp)^2$ and applying Bayes theorem, Chapter 4.1, Equation 4.1 for the computation of the posterior distribution, see Figure 6.26 to Figure 6.28. In these plots the prior distribution is indicated by red histograms, black histograms reflect the posterior distributions. These distributions are compared with the ones given by the Monte Carlo sampling, Chapter 6.3.1, Figure 6.13 to Figure 6.15. Generally, it can be seen that the posterior distribution does not differ significantly to the prior one. Analyzing the distributions in more detail shows, that models with a high fit are indicated by an east component $437 \cdot 10^3 \leq \xi \leq 439 \cdot 10^3$ m and $440 \cdot 10^3 \leq \xi \leq 441 \cdot 10^3$ m, indicated by a larger difference in this region between prior and posterior distribution. Furthermore, the second region is also found by the Monte Carlo sampling, see Chapter 6.3.1, Figure 6.13. According to the north component, models with a higher fit are characterized by north components between $9164 \cdot 10^3 \leq \psi \leq 9167 \cdot 10^3$ m, whereby this region could not be determined in detail by the first sampling set. The depth component ζ shows only slight changes between prior and posterior distribution whereby shallow depths produce a better fit. The more likely region given by large ζ values, which has been figured out by the Monte Carlo sampling, is not confirmed. Also the pressure distributions p show nearly no difference due to applying Bayes theorem. Models with a higher fitness are defined by p values $p < 0$ Pa or values $80 \cdot 10^5 \leq p \leq 100 \cdot 10^5$ Pa. Contrary, in the first sampling set no region of the posterior distribution could be figured out significantly which would indicate a higher fit. Models with a radius component $r \leq 0.7 \cdot 10^3$ m show a higher fitness whereby also this behavior cannot be seen in the first sampling set, see Chapter 6.3.1, Figure 6.15. The mass component m turns out to be very small near 0 kg, which fits to the results determined from the first sampling set.

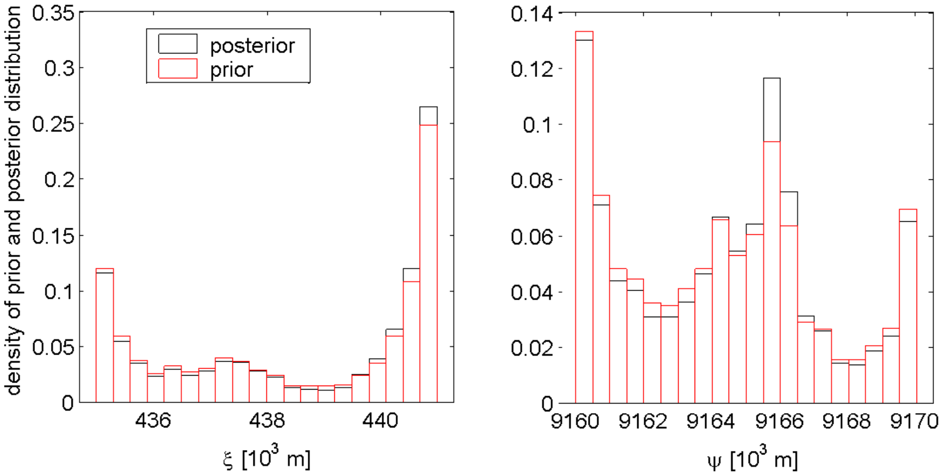

Figure 6.26: Prior and posterior distributions of the east and north component, generated by the filtering approach, anticipating likelihoods $1/\chi(comp)^2$ for the posterior distribution.

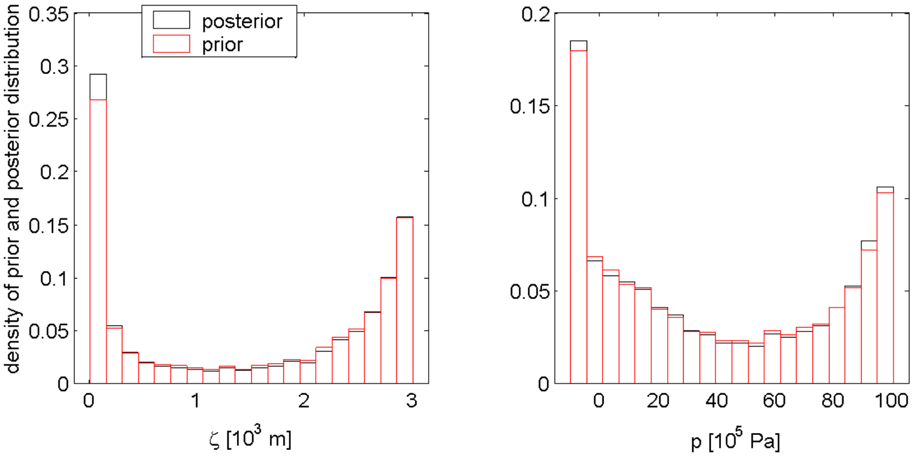

Figure 6.27: Prior and posterior distributions of the depth and pressure component, generated by the filtering approach, anticipating likelihoods $1/\chi(comp)^2$ for the posterior distribution.

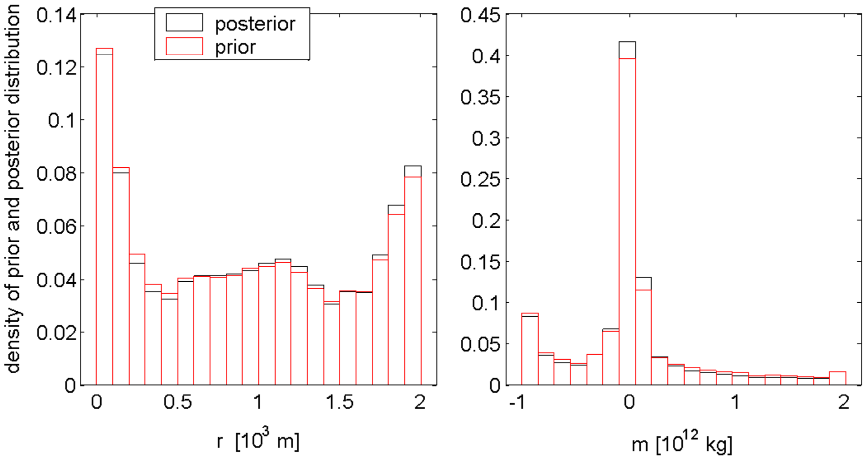

Figure 6.28: Prior and posterior distributions of the radius and mass component, generated by the filtering approach, anticipating likelihoods $1/\chi(comp)^2$ for the posterior distribution.

The non-orthogonality of the sampling set is the reason why the variance-based global sensitivity analysis cannot be applied as described in Chapter 4.2.1 for this sample set. (Note: To compute these variances for correlated input parameter samples, several approaches have been investigated and are described in the literature. The variances are computed by means of multidimensional integrals in the space of the unknown input parameters. These integrals can be estimated by a number N of Monte Carlo samplings, by fixing one input parameter at a certain value, repeating this at various values of this input parameter. This procedure would require for the computation of the first order effects S_i $u \cdot N \cdot f$ (with u = number of unknown input parameters, f = number of fixing points) runs of the model, which is very cost intensive. If only 100 Monte Carlo samplings and 100 discretization steps of the range of each of the six unknown input parameter are taken into account (60000 model executions). The number of model computations of the second order effects is $0.5u \cdot (u-1) \cdot N \cdot f$, so that additional 150000 executions would be necessary only for this computation. An additional problem arises if constraints of the input parameter have to be included. The cost intensive process and the fact that the TSIs are already given for the whole area of the unknown input parameters leads to the application of another sensitivity approach for this sample.) The applied RSA described in Chapter 4.2.2 give information about the change of the sensitivities when increasing the fitness. Three different samples are analyzed whereby the filtering sample set is divided into two sub samples, and the third one is created by the Monte Carlo sampling of Chapter 6.3.1. To list the three different samples:

- First sample set - **S1**: This set consists only of samples generated by the filtering approach with $0.0050 < 1/\chi(comp)^2 \leq 0.0080$.

- Second sample set - **S2**: The second sample set consists of samples generated by the filtering approach with $0.0027 < 1/\chi(comp)^2 \leq 0.0050$.

- Third sample set - **S3**: This set has been generated of the Monte Carlo set computed in Chapter 6.3.1, whereby the original sample set has to be reduced to avoid an overlapping of the sub samples, so that $10^{-8} < 1/\chi(comp)^2 \leq 0.0027$.

For the RSA two sub samples $\mathbf{c}|B$ and $\mathbf{c}|\bar{B}$ are built for each of the three mentioned samples by the separation of the descending sorted samples $1/\chi(comp)^2_s$, so

$$\mathbf{c}|B = \left\{1/\chi(comp)^2_s\right\}_{i=1,0.5\cdot n} \quad (6.8)$$

$$\mathbf{c}|\bar{B} = \left\{1/\chi(comp)^2_s\right\}_{i=1+0.5\cdot n,n} \quad (6.9)$$

with $\mathbf{c}$ = sample set and n = number of samples = 7168.

Figure 6.29 to Figure 6.31 display the cumulative distributions of $\mathbf{c}|B$ and $\mathbf{c}|\bar{B}$ as well as the distribution of the whole second sample set. Comparing the different distribution shapes of the three samples leads to interesting results: It becomes obvious, that the sensitivity is changing with objective function's increasing fitness. For a complete analysis, the gradient of the density functions has to be taken into account in combination to the change between $\mathbf{c}|B$ and $\mathbf{c}|\bar{B}$ over the three samples.

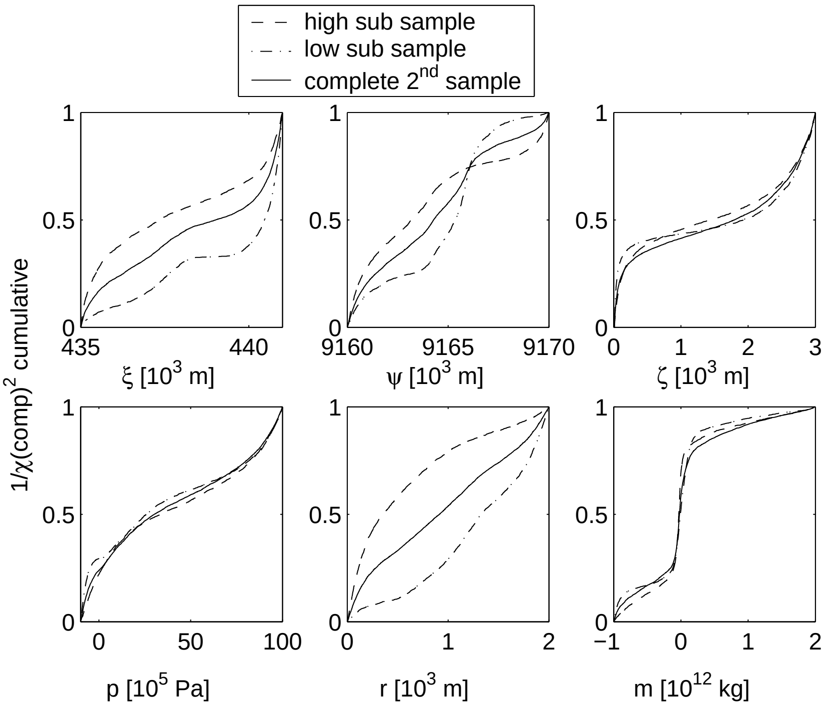

Figure 6.29: $\mathbf{c}|B$ and $\mathbf{c}|\bar{B}$ distribution of $1/\chi(comp)^2$ for $\mathbf{c} = \mathbf{S1}$.

Flat regions in the curves are representing areas of the unknown input parameter where only few corresponding output values had been classified to be in the certain sub sample. Steep gradients indicate that for this region of input parameter due to the classification criterion many output values belong to the sub sample $\mathbf{c}|B$ or $\mathbf{c}|\bar{B}$. Only small differences of the distribution between $\mathbf{c}|B$ and $\mathbf{c}|\bar{B}$ indicate that the unknown input parameter is not responsible for classifying the output samples in $\mathbf{c}|B$ or $\mathbf{c}|\bar{B}$. Opposite shapes of $\mathbf{c}|B$ and $\mathbf{c}|\bar{B}$ indicate the best classification possibility (if $\mathbf{c}|B$ is showing a gradient near 0 in a certain area whereby the gradient of $\mathbf{c}|\bar{B}$ reaches 1).

The Kolmogorov-Smirnov test statistics according to Chapter 4.2.2 with a significance level of α=1% is applied to the sample sets $\mathbf{S1}|B-\mathbf{S1}|\bar{B}$, $\mathbf{S2}|B-\mathbf{S2}|\bar{B}$ and

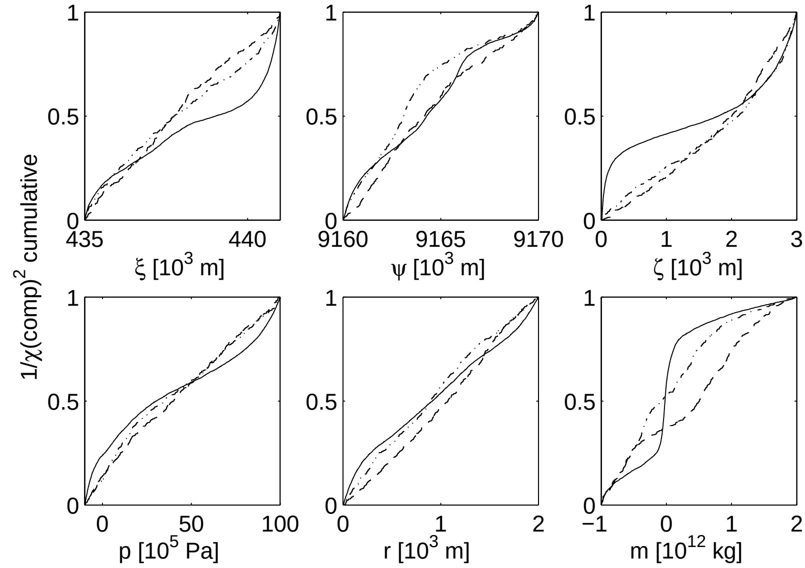

Figure 6.30: $\mathbf{c}|B$ and $\mathbf{c}|\bar{B}$ distribution of $1/\chi(comp)^2$ for $\mathbf{c} = \mathbf{S2}$.

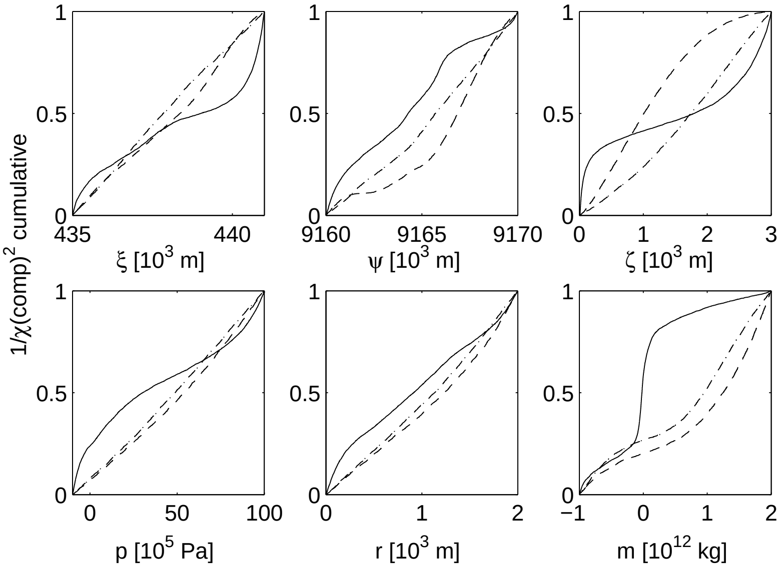

Figure 6.31: $\mathbf{c}|B$ and $\mathbf{c}|\bar{B}$ distribution of $1/\chi(comp)^3$ for $\mathbf{c} = \mathbf{S3}$.

$\mathbf{S3}|B - \mathbf{S3}|\bar{B}$. The statistics states that only for the east ξ, depth ζ and pressure p of $\mathbf{S2}|B - \mathbf{S2}|\bar{B}$ the H_0-hypothesis is accepted with the given significance level. So all other components show the power to classify the fitness into the given sub samples, anticipating α=1%. In addition to the test statistics, Table 6.13 summarizes the maximal differences between the sub samples for each unknown input parameter. The table underlines the varying power of specification. The larger the values are, the better is the classification possibility (regarding the two sub samples) of the corresponding unknown input parameter.

	ξ	ψ	ζ	p	r	m
$max\lvert\mathbf{S1}\rvert B - \mathbf{S1}\lvert\bar{B}\rvert$	0.3154	0.3066	0.1161	0.1249	0.5193	0.1748
$max\lvert\mathbf{S2}\rvert B - \mathbf{S2}\lvert\bar{B}\rvert$	0.0938	0.1837	0.0978	0.0570	0.1202	0.2664
$max\lvert\mathbf{S3}\rvert B - \mathbf{S3}\lvert\bar{B}\rvert$	0.1000	0.1954	0.3246	0.0561	0.0658	0.1578

Table 6.13: Results of Kolmogorov-Smirnov test statistics.

Summarizing the main aspects which can be drawn out of the RSA, leads to the following assumptions: The change between the first and the second sub sample is significant and also larger than the difference between the second and third sub sample, although the range of the output $1/\chi(comp)^2$ changed by smaller amounts between the first and second sub sample. The changing sensitivity with the increase of the fitness of the output must be therefore anticipated. Moreover, the larger the fitness is getting the larger is the increase of sensitivity change. Also the maximal differences which are given in Table 6.13 are changing with varying fitness classifications. Generally, the power of classifying the east component ξ is increasing for **S1** compared to the samples **S2** and **S3**. The same effect appears regarding the north ψ and radius r component. The power to classify an output into $\mathbf{c}|B$ or $\mathbf{c}|\bar{B}$ is concerning the depth component ζ large, if the fitness is small (**S3**). If the fitness is increasing, the classification due to this component is not possible any more. A classification into $\mathbf{c}|B$ and $\mathbf{c}|\bar{B}$ due to the pressure component p is not possible with the fitness either being good or being bad.

This second sensitivity analysis underlines, that the optimization of the nonlinear inversion, which is based on the generalized static Navier equations described in Chapter 2.1, is not trivial. The different types of observations have different sensitivities concerning changes in the unknown input parameters, which are analyzed in detail in Chapter 6.3.1. These sensitivities change with increasing fitness of the objective function, so the inversion problem increases in complexity.

6.4 Modeling

In this chapter synthetic data have been generated in order to configure the two optimization approaches, described in Chapter 3.1.1 and Chapter 3.2.1 properly for the application. These synthetic data reflect the observed data by taking first results from the genetic algorithm optimization, Tiede *et al.* (2004). The model is described by the following values of the source, given in Table 6.14, and $1/\chi(comp)^2 = 0.00862$. By applying F-statistics, see Chapter 6.3, Equation 6.5, with $T_{synthetic} = 2.33754 < F(0.9999, 80, 74) = 2.38549$ the H_0-hypothesis can be accepted so that the model fits the data with a significance level of 0.01%. The standard deviations for the synthetic data of this model are computed by anticipating normal distributed standard deviations, by $\sigma() = k() + rand(0,1) \cdot m()$, with $k()$ = additional constant value and $m()$ = multiplication factor, both with respect to the kind of observation, given in brackets. These data has to be modeled by the downhill simplex and the GA approach. The downhill simplex approach is computed by the software Matlab Release 13, using the function $fminsearch$ in which the downhill simplex algorithm is implemented. In order to compute the downhill simplex under the same conditions as the GA, an additional penalty term had been added forcing all results of the optimization to lie in between the given limits of the unknown parameters, given in Chapter 6.3, Table 6.6. Due to its variation of the simplex, see Chapter 3.1.1, the generation of solutions beyond these boundaries would be otherwise possible.

source parameter	source for synthetic data	synth. model downhill simplex	synth. model GA
ξ [10^3 m]	439.372	439.372	439.372
ψ [10^3 m]	9166.185	9166.185	9166.185
ζ [10^3 m]	0.020	0.020	0.020
p [10^5 Pa]	55.15	1.033	81.76
r [10^3 m]	0.452	1.702	0.396
m [10^{12} kg]	0.0251	0.0251	0.0251
$p \cdot r^3$ [$kg \cdot m^2/sec^2$]	5.093	5.093	5.077
T(80,74)	2.33754	1.08101	1.08111
$1/\chi(comp)^2$	0.00862	$1/(2 \cdot 10^{-6})$	$1/3 \cdot 10^{-5}$

Table 6.14: Source parameters for the synthetic data generation.

The optimization approach consists of 500 samples, whereby the maximum of iterations is set to 5000 for each sample, so that the same kind of termination criterion is set for the downhill simplex as for the GA. Figure 6.32 shows the results of this approach by displaying the $\chi(comp)^2$ values of the generated samples. The best result of the downhill simplex samples concerning its fitness of the objective function is given in Table 6.14 with $\chi(comp)^2 = 2 \cdot 10^{-6}$. This high fitness demonstrates that the downhill simplex algorithm could determine the source which had been anticipated for the modeling of the synthetic data. Note: $p \cdot r^3$ has to be compared between the synthetic source and the determined best model. The result is tested by applying F-test: With $T_{synt(downhill)} = 1.08101 < F(0.68, 80, 74) = 1.11215$ the model fits the synthetic data with a significance level of 32%. Although the algorithm could compute the synthetic source, a large dispersion of the fitness values can be seen (mean fit of $\chi(comp)^2 = 101.05$, smallest fit of $\chi(comp)^2 = 681.29$) which implies, that the algorithm cannot escape from a local optimum, if it runs into it once. The restarting process of the algorithm results in a probabilistic part, that the algorithm might find the global optimum, whereby the probability increases with increasing number of restarts. But this increase forces also the increase of

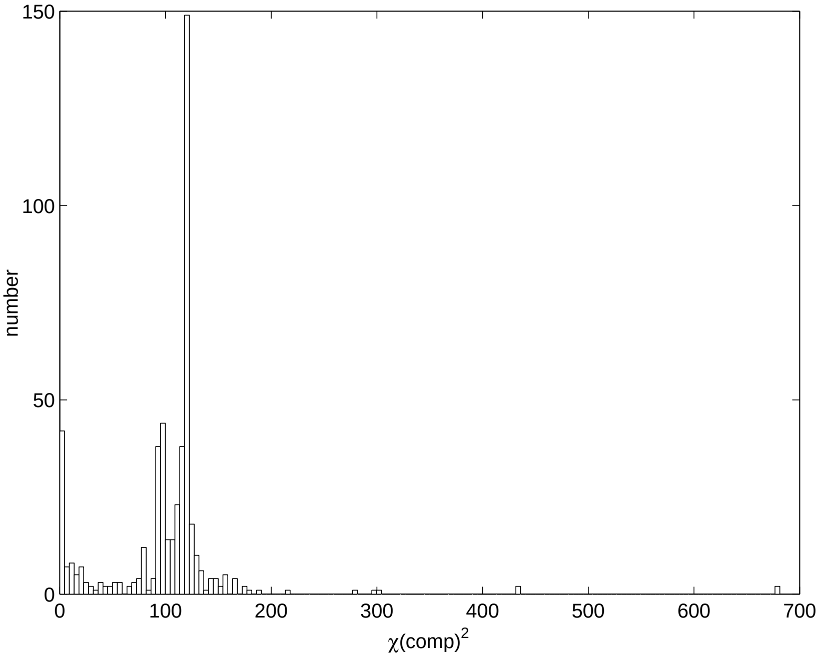

Figure 6.32: Histogram of $\chi(comp)^2$, generated by 500 downhill simplex samples, using synthetic data for *dg*, *uz*, *ux* and *uy*.

computation time. Due to the reason that the algorithm could reproduce the underlying source of the synthetic data. Because of its advantages, that it is a fast (elapsed CPU-time for the computation of one sample ≈ 80 seconds on a Pentium 1.6 GHz machine), well explored and stable optimization tool, it has been taken into account for the following investigation of improvement approaches. Nevertheless, the drawback that most of the results reflect only local optima has to be kept in mind.

The GA approach, described in Chapter 3.2.1, has been used for the optimization of the synthetic model with a generation of 50 samples, whereby the population size is set to 100 individuals. Each sample is computed for 1000 generations. These parameters had been chosen due to initial configuration runs, where stable outputs could be achieved, so that a more time consuming computation of the GA by increasing the population and generation size could be avoided. Configuration runs had been investigated with varying population sizes of 100, 200, 500 and 1000, whereby no significant change in the parameter output values could be observed when reducing the population size to 100. This confirms that the possibility of running into a local optimum by decreasing the population does not exist for these numbers of individuals in a population. Furthermore, this population size is also proposed in optimization approaches dealing with similar inversions, TIAMPO *et al.* (2000), TIAMPO *et al.* (2004a). According to these references the probability of mutation has been set to 45% and the one for crossover to 95%.

The generation size has been evaluated from 12 GA runs of the original data, Figure 6.33, whereby the generation size is cut at a size of 5000. By anticipating a size of 1000, the difference between the fitness function and the converging result is smaller than 1%. Figure 6.34 displays the distribution of the determined results of the 50 GA samples whereby, compared with the distribution which has been carried out by the downhill simplex approach, the small dispersion around the nominal

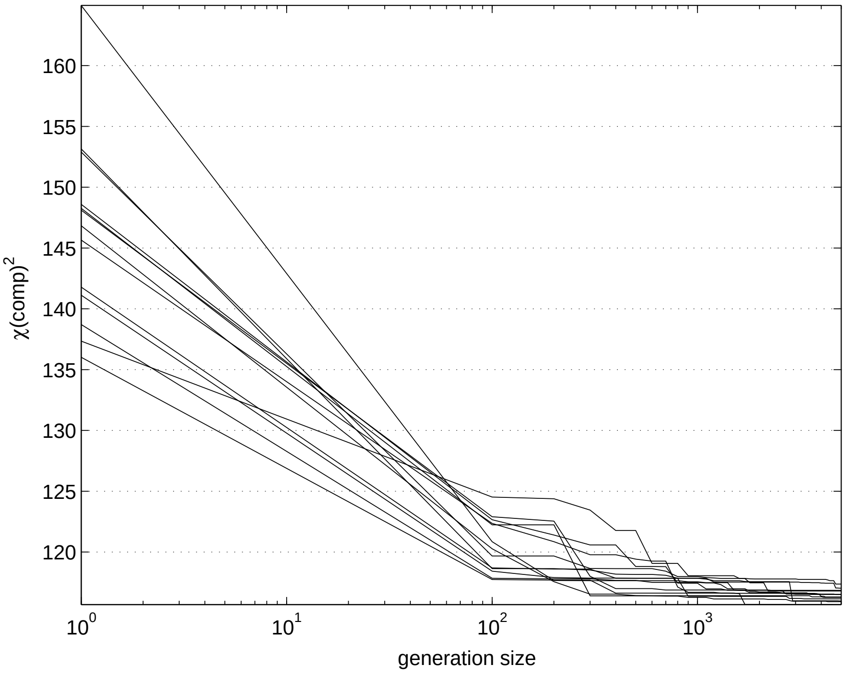

Figure 6.33: Relation between generated fitness function result and size of generation.

value of $\chi(comp)^2 = 0$ is obvious (with a mean fitness about $\chi(comp)^2 = 0.0108$, and the smallest fitness $\chi(comp)^2 = 0.065$). The best result according to the fitness is given in Table 6.14, whereby the synthetic model could be reproduced by the GA ($\chi(comp)^2$=$3.14 \cdot 10^{-5}$). This model is tested by F-test statistics $T_{synt(GA)} = 1.08111 < F(0.68, 80, 74) = 1.11215$ which states that the model fits the synthetic data with a significance level of 32%.

Summarizing the synthetic modeling leads to the results of taking both optimization approaches into account for further improvement approaches, described in Chapter 5. Both approaches could reproduce the generated synthetic data, whereby the dispersion of the downhill simplex approach is large. The increase of the iteration size from 5000 until 100000 did not decrease the dispersion significantly. So the number of re-runs has to be increased in order to increase the possibility to determine the global solution but not only a local one. On the other hand the GA generated good results within a small dispersion but in a longer time period than the downhill simplex approach. (Computation time of one sample with the GA $\approx$ 2.75 hours on a Pentium, 3GHz machine).

The two different optimization approaches have been chosen, and the following four different configurations concerning the implementation of improvement techniques, described in Chapter 5 are investigated, taking the real observed data of dg, uz, ux and uy:

- Optimization without any implementation of improvements.
- Optimization with the implementation of constraints, see Chapter 5.1.
- Optimization with the implementation of the global sensitivity analysis results, see Chapter 5.2.

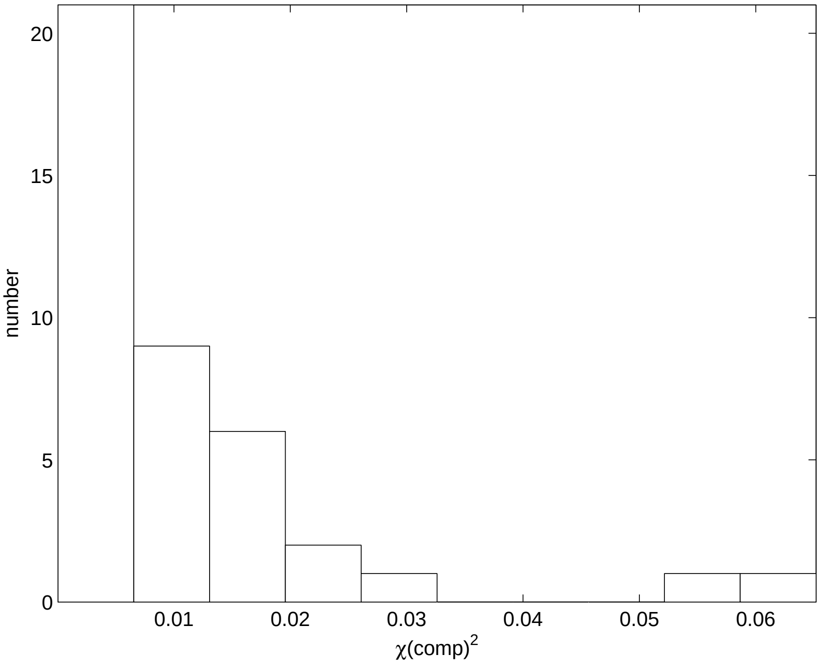

Figure 6.34: Histogram of $\chi(comp)^2$ generated by 50 GA samples, using synthetic data for dg, uz, ux and uy.

- Optimization with the implementation of fuzzy logic, see Chapter 5.3.

The results of each sample set approach are shown by the correlation matrix, in order to describe the linear behavior between the computed unknown input parameters and in order to analyse the influence of the applied improvement in relation to the sampling, which is determined without applying any improvement. Some correlation coefficients can be anticipated by analyzing the underlying physical based mathematical model and the results of the variance-based sensitivity analysis:

- The correlation between east ξ and north ψ component is supposed to be high and negative, caused by the point configuration of the significant measurements at the summit, compare Chapter 6.3.1.
- The correlation between depth ζ and energy form $p \cdot r^3$ has to be negative. Two combinations are possible: A negative correlation between radius r and ζ, accompanied with a positive correlation between ζ and pressure p or vice versa.
- The correlation between r and p has to be negative due to the defined energy form $p \cdot r^3$ in the underlying physical based mathematical model, Chapter 2.1.

From the generated 500 downhill samples and 50 GA samples respectively, the best sample according to its fitness of the objective function is chosen. For this sample the modeled values are generated and plotted against the observed ones. In addition, for this source all unknown parameters as well as the physical reliability (computed by the fuzzy logic controller, see Chapter 5.3), fitness (separately for all kind of observations and also for all observations together) and the result of the applied F-test statistics are given and compared in Table 6.23. The results are shown in cumulative distributions for each of the unknown input parameters ξ, ψ,

ζ, p, r and m of the unknown source which is responsible for the measured changes in gravity as well as for the three dimensional deformations, Chapter 6.4.3, Figure 6.43 to Figure 6.48.

Finally, a comparison between the downhill simplex and the GA optimization approach as well as between all configurations is investigated in order to give a recommended approach for the optimization of the source based on the described physical based mathematical model. Discussions about the adaption of the underlying physical based mathematical model complete the chapter and result in a refinement of the model. This final model is described in Chapter 6.5 and is validated by the results of other geophysical and geochemical observations and modeling approaches for Merapi.

Note: For all results of optimization the determined sources are based on the underlying mathematical half-space model, so topography is not taken into account. For all results, except these which are determined by the improved approach with the implementation of constraints, the resulting source must be interpreted in that way, that the determined mass occurs at the determined position of the source. But the source is neither explained by a spherical body nor by a homogeneous filled body in these optimization approaches. The only statement which can be done about radius and pressure is that the energy form which is given by $p \cdot r^3$ is taking place at the determined position.

6.4.1 Downhill Simplex Approach

For each downhill simplex optimization approach 500 samples are generated, whereby the maximum of iterations is fixed at 5000. The described boundary limits in Chapter 6.3, Table 6.6 are used for all computations.

The first sampling is generated by applying the downhill simplex approach without any implementation of improvement. The correlation coefficients between the unknown parameters are given in Table 6.15 whereby the anticipated negative correlation between r and p can be seen. The opposite correlation between ζ-p and ζ-r does not occur; both correlation coefficients are very small. The best sample with $1/\chi(comp)^2 = 0.01098$ is shown in Figure 6.35. This model fits very well the north component uy, especially the large displacement which is occurring at observation point no. 3. Applying F-test results in accepting the H_0-hypothesis with $T_{downhill} = 1.50673 < F(0.9999, 80, 74) = 2.38549$ so the model fits the data with a significance level of 0.01%.

ξ	1	-0.2138	-0.2320	0.2331	0.3128	-0.1366
ψ		1	0.1044	0.0342	-0.2653	0.2644
ζ			1	0.0438	0.0270	0.0274
p				1	-0.2874	0.0689
r					1	0.0884
m						1
	ξ	ψ	ζ	p	r	m

Table 6.15: Correlation coefficients between the unknown input parameters determined by 500 downhill simplex samples without implementation of improvement approaches.

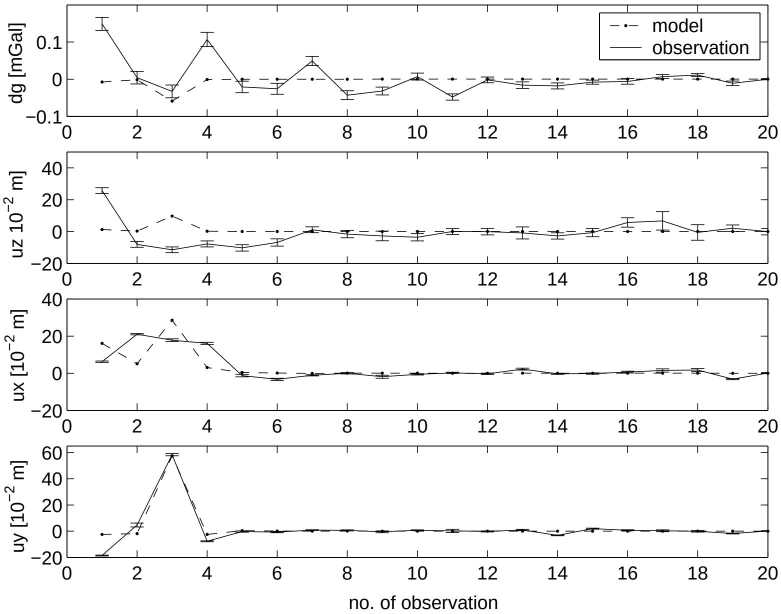

Figure 6.35: Overview of modeled and observed values for gravity changes dg, vertical displacements uz and horizontal displacements ux and uy. The model is computed by the best sample of the downhill simplex approach without implied improvement approaches.

The second configuration is determined by applying the defined constraints, described in Chapter 5.1. In comparison to Table 6.15 in this approach the

ξ	1	-0.2271	-0.1542	0.2565	0.3085	0.0779
ψ		1	0.1112	-0.0498	-0.1730	0.1348
ζ			1	-0.1074	0.1314	-0.0523
p				1	-0.4126	0.0704
r					1	0.1678
m						1
	ξ	ψ	ζ	p	r	m

Table 6.16: Correlation coefficients between the unknown input parameters, determined by 500 downhill simplex samples including constraints in the optimization configuration.

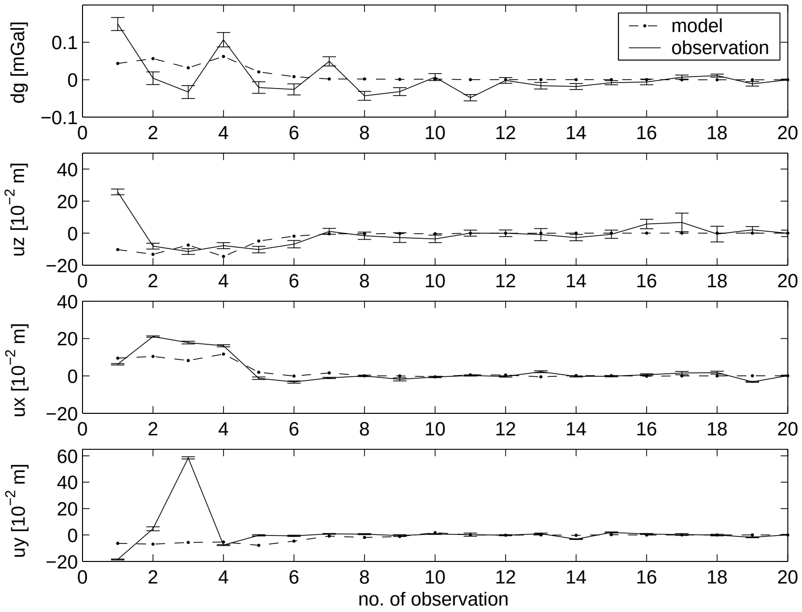

Figure 6.36: Overview of modeled and observed values for gravity changes dg, vertical displacements uz and horizontal displacements ux and uy. The model is computed by the best sample of the downhill simplex approach including constraints in the optimization configuration.

correlation between ζ-p as well as between ζ-r component could be determined like it is anticipated. Also the negative correlation between p and r is determined. All other coefficients only change slightly, compared to the approach without any improvement, Table 6.15. The best sample with a value of $1/\chi(comp)^2 = 0.00755$ is given in Figure 6.36. Comparing this model with the one which has been generated without any improvement implementation, the main difference can be seen in the power of modeling the north component of the displacements, see Table 6.23. By applying the constraints, the north component cannot be modeled with the high fit like before. It has to be pointed out, that the good fit of the north component from the model without any improvement is related to the fit of only one observation point (no. 3). By taking the constrained improvement approach into account, the results adapt the observed data in a more global sense; but this is also accompanied by a lower fit. This result is quite interesting but not expected and therefore discussed in the final comparison, Chapter 6.4.3. The applied F-test shows that the inclusion of constraints causes the model to not fit the observed data with the given significance level of 0.01% any more, ($T_{constr(downhill)} = 3.94300 > F(0.9999, 80, 74) = 2.38549$).

The implementation of the TSIs, which result of the global sensitivity analysis, Chapter 6.3.1 reflects the second improvement approach. The correlation matrix

ξ	1	-0.3633	-0.1573	0.0963	0.3245	-0.0942
ψ		1	0.0787	-0.0485	-0.3587	0.2810
ζ			1	-0.0308	0.0265	-0.2632
p				1	-0.2945	0.1113
r					1	-0.0653
m						1
	ξ	ψ	ζ	p	r	m

Table 6.17: Correlation coefficients between the unknown input parameters, determined by 500 downhill simplex samples including the results of the global sensitivity analysis.

given in Table 6.17 shows the negative correlation, which is anticipated between ψ and ξ better than the original sampling set. Also the correlations between ζ, p and r could be determined as anticipated. The best sample with a value of $1/\chi(comp)^2 = 0.01048$ is shown in Figure 6.37, (accepted H_0-hypothesis of the F-test: ($T_{sens(downhill)} = 1.50842 < F(0.9999, 80, 74) = 2.38549$)). By comparing this

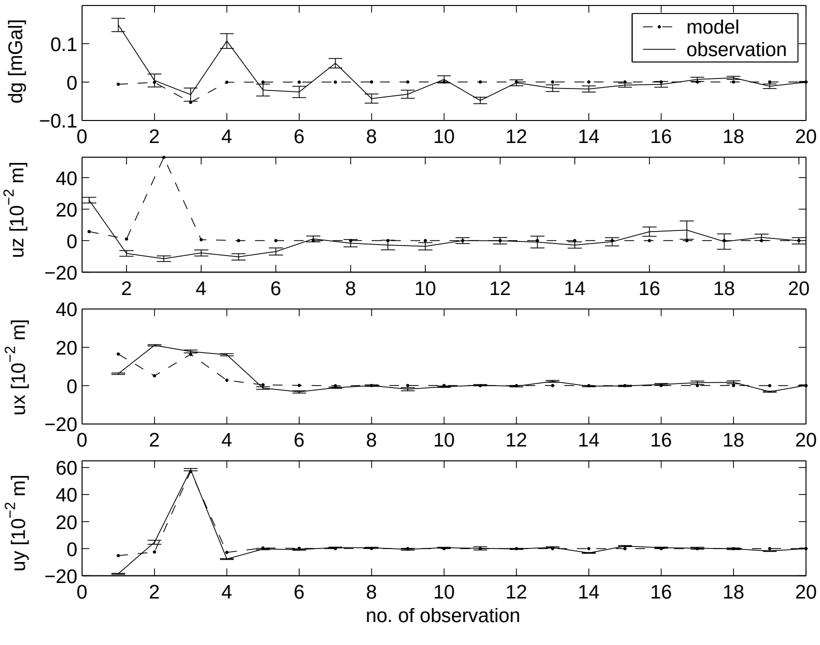

Figure 6.37: Overview of modeled and observed values for gravity changes dg, vertical displacements uz and horizontal displacements ux and uy. The model is computed by the best sample of the downhill simplex approach including the results of the global sensitivity analysis.

model with the one which is given by the optimization without any improvement approaches, it can be seen that a better fitness could be achieved in the modeled north displacements, Table 6.23. Taking the sensitivity analysis results concerning the radius component into account and the fact, that the north displacements are mainly sensitive against changes in the radius component, this increase in the fitness could be expected, due to the increased weight of these type of observations in the whole optimization approach.

The last improvement approach has been investigated by implying the fuzzy logic controller, Chapter 5.3.

ξ	1	-0.2028	-0.1877	0.1797	0.2776	-0.1474
ψ		1	0.0673	0.0319	-0.2035	0.3214
ζ			1	0.0504	0.0840	0.0381
p				1	-0.3517	0.1273
r					1	0.0124
m						1
	ξ	ψ	ζ	p	r	m

Table 6.18: Correlation coefficients between the unknown input parameters, determined by 500 downhill simplex samples including fuzzy logic.

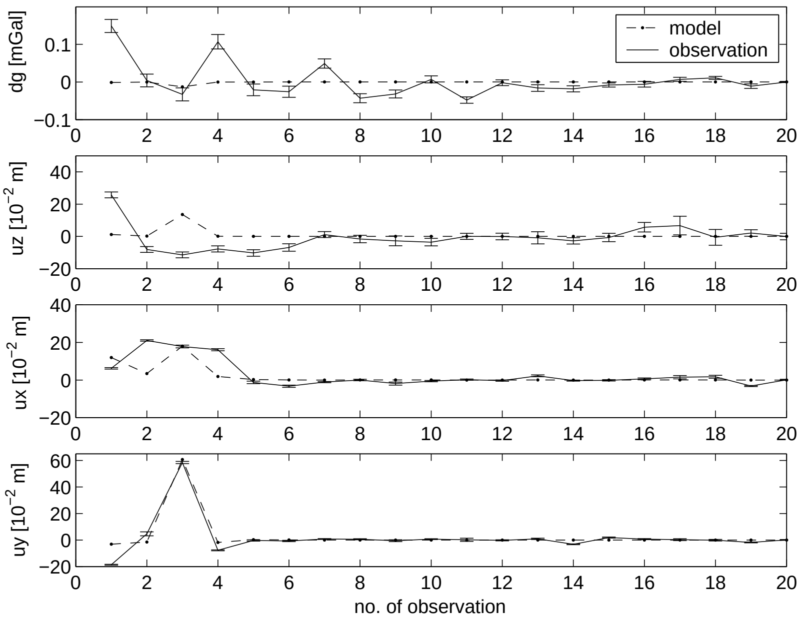

Figure 6.38: Overview of modeled and observed values for gravity changes dg, vertical displacements uz and horizontal displacements ux and uy. The model is computed by the best sample of the downhill simplex approach including fuzzy logic.

This approach does not show significant changes in the correlations compared to the coefficients which were computed in the optimization approach without any improvement. Furthermore, due to the applied fuzzy logic, additional non-linear behaviors are incorporated into the model, which are related to the information drawn out of the fuzzy logic model. This means, that inferences regarding the reason for a possible correlation change cannot be described in more detail. The best sample with a value of $1/\chi(comp)^2 = 0.01129$ is shown in Figure 6.38, whereby the main difference to the model without any improvement is given by a smaller fit of the height displacements uz, Table 6.23. Also this modeling approach gives a significant fit, proved by applying F-test with $(T_{fuzzy(downhill)} = 1.78499 < F(0.9999, 80, 74) = 2.38549)$.

6.4.2 Genetic Algorithm Approach

In all GA approaches the configuration of the parameters have been anticipated as they were evaluated in the synthetic GA approach due to the valuable results of the proven modeling configuration, see Chapter 6.4.

The first 50 samples have been determined without implied improvement approaches. The correlation coefficients, Table 6.19 reflect the high negative correlation between ξ and ψ, which might be related to the point configuration of the significant observations, and which is also proved by the sensitivity analysis, Chapter 6.3.1, Figure 6.22. Furthermore, a high negative correlation between r

ξ	1	-0.8542	-0.6432	-0.0369	0.1535	0.7003
ψ		1	0.4594	-0.0623	-0.0039	-0.5547
ζ			1	0.0828	-0.1807	-0.8980
p				1	-0.8318	-0.0647
r					1	0.1760
m						1
	ξ	ψ	ζ	p	r	m

Table 6.19: Correlation coefficients between the unknown input parameters, determined by 50 GA samples without implied improvement approaches.

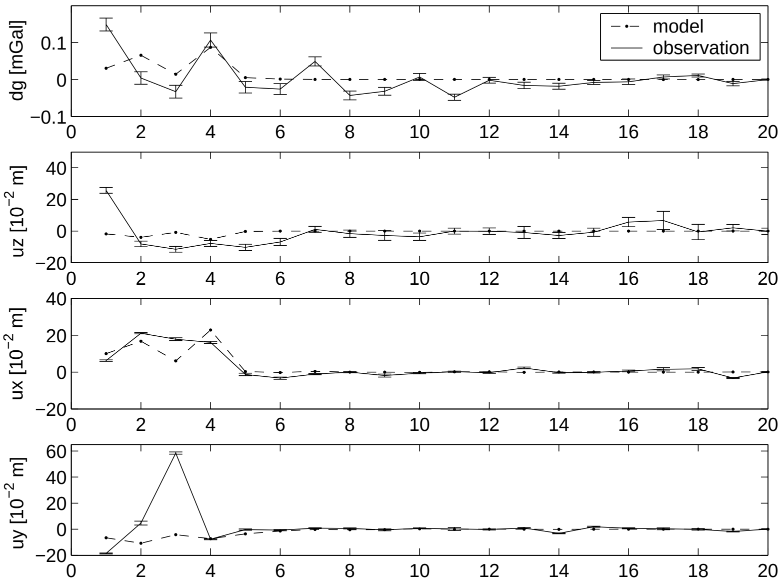

Figure 6.39: Overview of modeled and observed values for gravity changes dg, vertical displacements uz and horizontal displacements ux and uy. The model is computed by the best sample of the GA approach without implied improvement approaches.

and p as well as the relation between the correlations of ζ-p and ζ-r which satisfy the underlying physical based mathematical model can be determined. The best sample with a value of $1/\chi(comp)^2 = 0.00865$ is shown in Figure 6.39, (F-test: $T_{GA} = 2.31169 < F(0.9999, 80, 74) = 2.38549$). The model fits the observed data with the given significance level of 0.01%. Nevertheless, the fit of the corresponding downhill simplex approach is better. By comparing the best model determined by the 50 GA samples without any improvement approach, Figure 6.39 with the corresponding result of the downhill simplex approach, Chapter 6.4.1, Figure 6.35, it can be seen, that the main difference is in the model fit of the east and north displacements, see Table 6.23. The GA approach models the east component with a higher fit, which has the effect, that the north observations cannot be modeled as good as in the downhill simplex approach. Similar results to the GA approach without implementation of improvement approaches are as in the downhill simplex approach with anticipating the constraints, Figure 6.36. This approach, determined by the GA, seems to be a more global fit, whereby the downhill simplex approach is adapting the model mainly according to the large displacement in the north component. For further explanations concerning this effect, it is referred to the final comparison, Chapter 6.4.3.

As a first improvement approach for the optimization, the defined constraints, Chapter 5.1, have been applied to the GA optimization. Analyzing the correlation coefficients which are given in Table 6.20, it becomes obvious, that the high correlation between ξ and ψ could not be evaluated in that manner, as was possible without anticipating improvement approaches. The correlations between ζ, p and r satisfy very well the anticipations whereby the very high values are referred to the defined constraints. Generally, it turns out, that all correlations are increasing except the ones concerning the m. These small values show that the constraints caused a decoupling of the mass from the other unknown parameters. Figure 6.40 displays the best model, which was determined by this approach with $1/\chi(comp)^2 = 0.00731$. The main differences caused by the implementation of the constraints into the optimization approach appear in the decreased fit of the model to the observed gravity changes dg (decrease of fitness about $1/\chi(dg)^2 = 42\%$) and height displacements uz (decrease of fitness about $1/\chi(uz)^2 = 22\%$), Table 6.23. Keeping the $TSI()_m$, Chapter 6.3.1, Figure 6.24 in mind, these two types of measurements show a high sensitivity to changes in the mass m value, whereby the m is showing the mentioned low correlation to all other unknown parameters in this approach. Anticipating a larger dispersion of m, this effect would be seen in the fitness of the modeled gravity changes dg and height displacements uz. Testing this model by F-test statistics shows that the implementation of constraints into the GA, as in the case of the downhill simplex approach, results in a model which does not fit the observed data with the significance level of 0.01%, ($T_{constr(GA)} = 3.56072 > F(0.9999, 80, 74) = 2.38549$). Summarizing the results which can be drawn out of the GA approach with included constraints leads to the

ξ	1	-0.4164	0.7626	-0.4521	0.7767	-0.0443
ψ		1	-0.4989	0.3331	-0.5065	-0.1278
ζ			1	-0.7003	0.9277	0.0500
p				1	-0.8468	-0.0056
r					1	-0.0102
m						1
	ξ	ψ	ζ	p	r	m

Table 6.20: Correlation coefficients between the unknown input parameters, determined by 50 GA samples including constraints into the optimization.

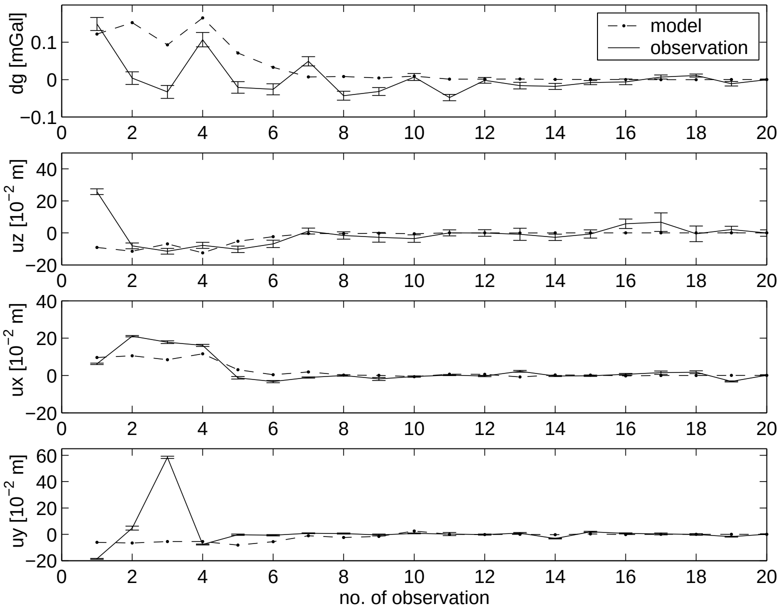

Figure 6.40: Overview of modeled and observed values for gravity changes dg, vertical displacements uz and horizontal displacements ux and uy. The model is computed by the best sample of the GA approach including constraints.

decoupling of the mass component from the determination of the other unknown parameters. This behavior influences only the output values which are most sensitive against changes in the mass component. Furthermore, the implementation of the constraints into the downhill simplex and also into the GA approach resulted in a model that does not fit the observed data with the given significance level.

The second improvement approach is investigated by applying the results of the sensitivity analysis, Chapter 5.2 to the optimization approach. This approach results in the smallest correlation coefficients concerning the mass component of all investigated optimization approaches, Table 6.21. Furthermore, the anticipated correlations between ζ, p and r as well as between ξ and ψ could be evaluated. The best sample with a value of $1/\chi(comp)^2 = 0.00864$ is shown in Figure 6.41, (F-test: $T_{sens(GA)} = 2.31747 < F(0.9999, 80, 74) = 2.38549$).

ξ	1	-0.8442	-0.5985	-0.0488	0.0875	0.0636
ψ		1	0.3798	-0.0375	-0.0756	-0.0429
ζ			1	-0.1143	0.1275	-0.0863
p				1	-0.9159	0.0575
r					1	-0.0677
m						1
	ξ	ψ	ζ	p	r	m

Table 6.21: Correlation coefficients between the unknown input parameters, determined by 50 GA samples including the results of the global sensitivity analysis.

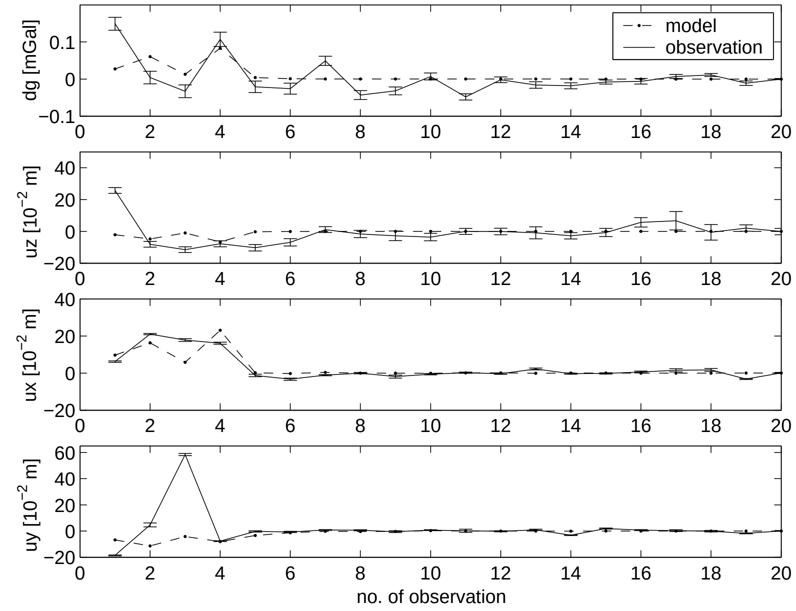

Figure 6.41: Overview of modeled and observed values for gravity changes dg, vertical displacements uz and horizontal displacements ux and uy. The model is computed by the best sample of the GA approach including the results of the global sensitivity analysis.

The implementation of the fuzzy logic set, described in Chapter 5.3 is investigated in the following section. The correlation coefficients in Table 6.22 reflect the anticipated interactions between ξ and ψ as well as between ζ, p and r. The best sample with a value of $1/\chi(comp)^2 = 0.00852$ is shown in Figure 6.42, whereby only insignificant differences between this result and the GA reference model, Figure 6.39 can be observed, Table 6.23. The applied F-test results in the acceptance of the H_0-hypothesis for a significance level of 0.01%, $(T_{fuzzy(GA)} = 2.29026 < F(0.9999, 80, 74) = 2.38549)$.

ξ	1	-0.7751	-0.1535	-0.0431	0.5086	0.4664
ψ		1	0.2969	-0.0081	-0.3288	-0.4445
ζ			1	-0.0562	0.0602	-0.3687
p				1	-0.7505	0.0196
r					1	0.1135
m						1
	ξ	ψ	ζ	p	r	m

Table 6.22: Correlation coefficients between the unknown input parameters, determined by 50 GA samples including fuzzy logic.

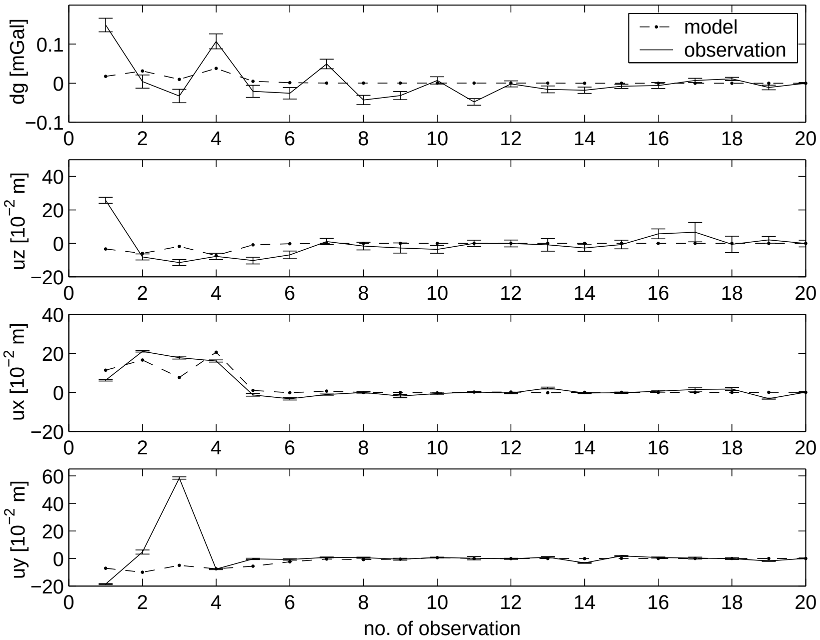

Figure 6.42: Overview of modeled and observed values for gravity changes dg, vertical displacements uz and horizontal displacements ux and uy. The model is computed by the best sample of the GA approach including fuzzy logic.

6.4.3 Comparison and Conclusions

The final comparison mainly focuses on the differences between the downhill simplex and the GA approach, whereby the conclusions are drawn from cumulative distributions of all approaches, separately for each of the unknown input parameters ξ, ψ, ζ, p, r, m as well as for $p \cdot r^3$.

Analyzing Figure 6.43 to Figure 6.49 the main drawback of the downhill simplex approach becomes obvious by comparing them with the samples generated by the GA approach: Generally all downhill simplex approaches show wide spreaded results. Moreover, the dispersion is ranging across the complete area in which the unknown input parameter are defined (limits are given in Chapter 6.3, Table 6.6).

Analyzing the cumulative distributions, it can be generally stated that the steeper the gradient of a determined unknown parameter, the better and the more stable its determination and the higher the sensitivity of $1/\chi(comp)^2$ according to this unknown parameter.

- Comparing the results of the east component ξ, leads to the following assumptions: No improvement approach could cause a better optimization result using the downhill simplex approach. The improvement approaches give some small areas, in which more samples are lying but nevertheless, the wide spreaded property of the downhill simplex approach could not be reduced by the applied techniques. Analyzing the results of the GA approach, it becomes obvious that the dispersion is increasing by implementing constraints or fuzzy logic into the optimization. This reflects a decrease of sensitivity of the observations concerning changes in ξ. The implementation of the sensitivity results causes a constant offset in the determination of the ξ with a small increase of the gradient, which implies a decrease in the dispersion as well as a sensitivity increase. Concerning the determination of ξ, the computation by all types of applied downhill simplex as well as by GA approaches which imply fuzzy logic or constrained improvements do not result in valuable sampling sets.

- According to the determination of the north component ψ, similar results are concluded, whereby the downhill simplex approach is able to locate a region around $9166 \cdot 10^3$ m in which more samples are lying. Nevertheless, no improvement approach could reduce the high dispersion. For the GA approaches the improvement applying the sensitivity results gives quite good results with a smaller dispersion than the original sample set, whereby an increase of dispersion is seen in all other improvement approaches. Also here, the approaches including fuzzy logic or constraints into the GA as well as all kind of downhill simplex approaches do not reflect valuable sampling sets.

- For the depth ζ determination the approaches determined by the downhill simplex could not be improved by applying improvement approaches. The cumulative distributions which reflect the implementation of the constraints, clearly show the influence of the constraints: ζ is set to be larger than the radius. This results in the shallow gradient of the function for small ζ values but could not reduce the dispersion at all. For the GA approaches, the fuzzy logic and constraints implementation causes a larger dispersion, whereby it can be anticipated that by implementing constraints into the determination concerning ζ, its dispersion should decrease. Furthermore, due to the increase of ζ values, also the energy form $p \cdot r^3$ has to increase. The implementation of the sensitivity result improvement causes a small decrease in the dispersion of the depth component. For the determination of ζ the best optimization approach is given by the implementation of the sensitivity analysis results into the GA approach.

- The distributions of the pressure component p with regard to the downhill simplex approaches an approximately linear trend, whereby no improvement approach could lead to a decrease of dispersion. The linear trend reflects the difficulty to determine p as well as the small sensitivity of $1/\chi(comp)^2$ concerning changes in p. The cumulative distributions of p, generated by the GA approaches show more signals. The implementation of the constraints causes the dispersion of p to be reduced to $32 \cdot 10^5 \leq p \leq 100 \cdot 10^5$ Pa. This effect is related to the physical relation of ζ, p and r. The implementation of the sensitivity analysis results causes a small reduction of the range of p, so the sensitivity concerning changes in p becomes larger in these mentioned improvement approaches. The fuzzy logic approach could determine two regions with a steeper gradient, whereby the dispersion could not be decreased by this approach. Concluding, the best optimization approach for the determination of p is given by the constrained improvement or the implementation of the sensitivity analysis results into the GA approach.

- The determination of the radius component r by the downhill simplex approaches show by implying constraints into the optimization approach a small offset, so larger r are computed. In order to get similar displacements caused by a deeper source, $p \cdot r^3$ has to increase. Due to the reason that the pressure does not show any offset in its cumulative distribution of the constrained optimization approach, r has to be enlarged. Apart from this signal the cumulative distributions of r computed by the downhill simplex approaches show an approximately linear trend. The cumulative distribution carried out by the GA approaches including constraints shows the increased r values which are forced by the included constraints. The implementation of the sensitivity analysis results causes a great improvement in reducing the dispersion of r. This behavior is anticipated because the improvement approach consists of including the sensitivities concerning changes in r. Concerning the determination of r, the most stable results could be determined by applying the GA approach including sensitivity analysis results.

- Analyzing the distributions of the mass component m, it becomes obvious that the downhill simplex approaches (except the one with implied results of the sensitivity analysis) show a steep increase in the distribution for values around 0 kg. The implementation of the sensitivity analysis results cause an increase of the dispersion, which might be related to the decreased weight of dg and uz, which are normally most sensitive concerning changes in m. In the implied sensitivity analysis approach the sensitivities concerning the radius component had been applied, whereby dg as well as uz do not show large sensitivities concerning changes in the radius component. The GA approach with implied results of the sensitivity analysis shows a similar distribution to the GA approach without implying any improvements. The steep gradient of the function implies that m could be determined very stably. This is a very interesting result because the implied results of the sensitivity analysis cause a smaller weight of dg which are normally highly sensitive to changes in m. The small dispersion of m has no linear influence on the other determined parameters, which results from the negligible correlation coefficients, Table 6.21 in this improved GA approach. The implementation of fuzzy logic and constraints cause a higher dispersion, which is similar to a decrease in the sensitivity against m. Concerning the determination of m the GA approach without any implementation of improvement or the approach implying the results of the sensitivity analysis are useful.

- The cumulative distributions of the product $p \cdot r^3$ show a steep increase of the distributions for small values near $p \cdot r^3 = 0 \cdot 10^{14} \mathrm{kg \cdot m^2/sec^2}$. The distributions generated with the GA show, that the dispersion by applying fuzzy logic as well as by applying the constraints cause a larger dispersion of $p \cdot r^3$, so that these two improved optimization approaches have to be neglected. The GA approach without applying any improvement approaches results in values $3.3990 \cdot 10^{14} \leq p \cdot r^3 \leq 4.5336 \cdot 10^{14} \mathrm{kg \cdot m^2/sec^2}$. Comparing this dispersion with the one which results of the approach by implying the sensitivity results into the GA shows that the dispersion can be decreased by the implementation of the sensitivity results into the GA approach with values of $3.0345 \cdot 10^{14} \leq p \cdot r^3 \leq 4.1620 \cdot 10^{14} \mathrm{kg \cdot m^2/sec^2}$.

Summarizing the comparison of all investigated optimization approaches leads to the assumption that the improved GA approach applying results of the sensitivity analysis is the best suitable one, because the dispersions of all unknown input parameters could be decreased or at least could be stabilized on the original dispersion given by the GA approach without any improvement.

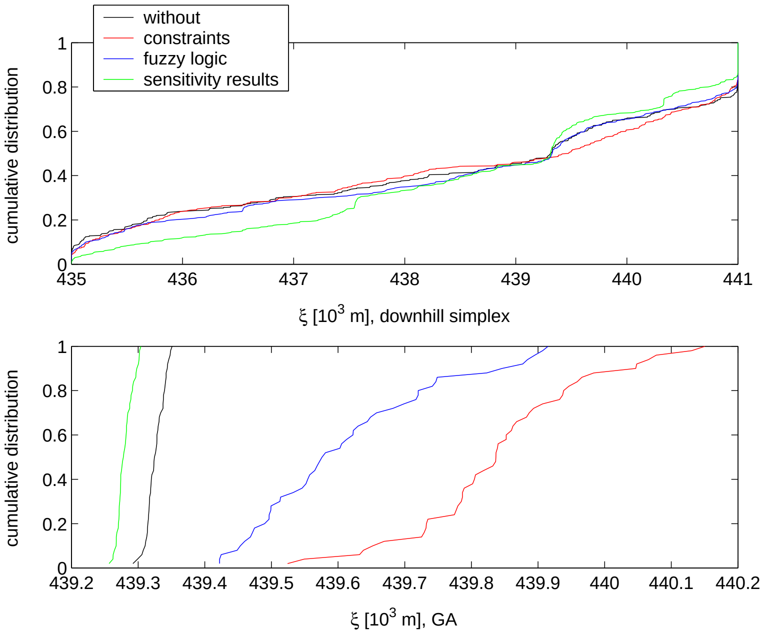

Figure 6.43: Cumulative distribution of ξ, generated with downhill simplex and GA samples, applying all kind of improvement approaches.

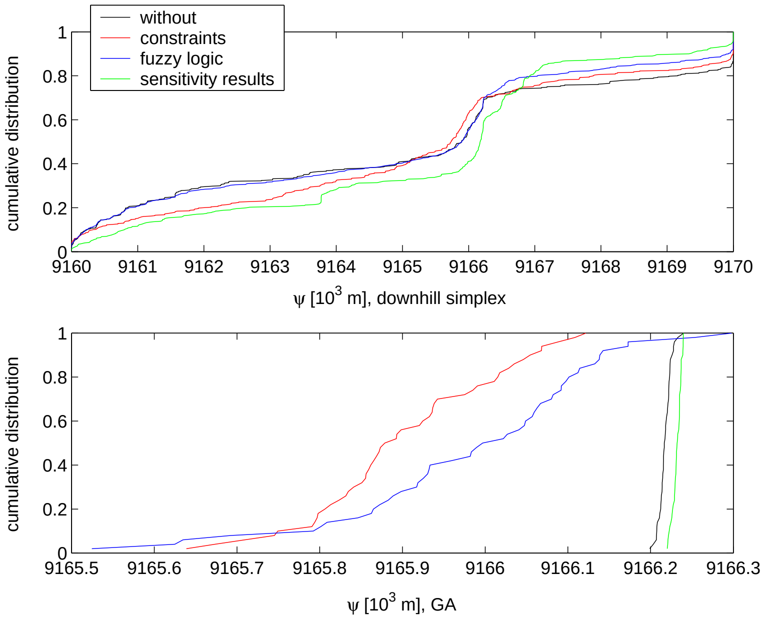

Figure 6.44: Cumulative distribution of ψ, generated with downhill simplex and GA samples, applying all kind of improvement approaches.

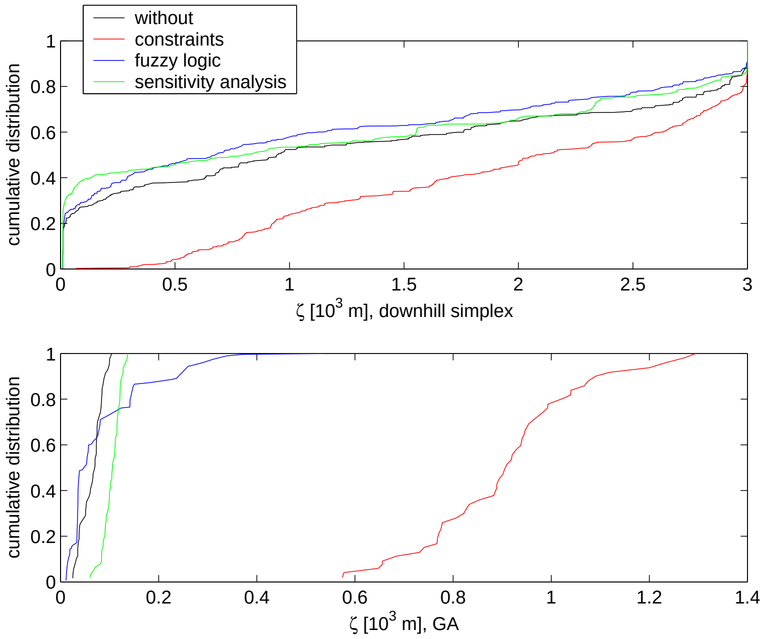

Figure 6.45: Cumulative distribution of ζ, generated with downhill simplex and GA samples, applying all kind of improvement approaches.

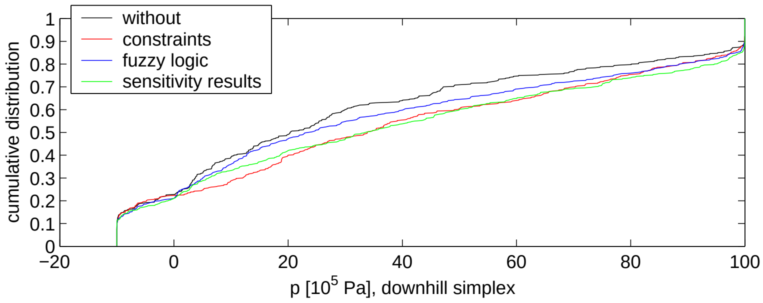

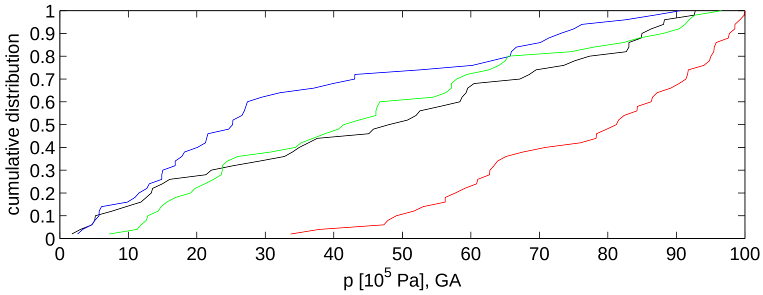

Figure 6.46: Cumulative distribution of p, generated with downhill simplex and GA samples, applying all kind of improvement approaches.

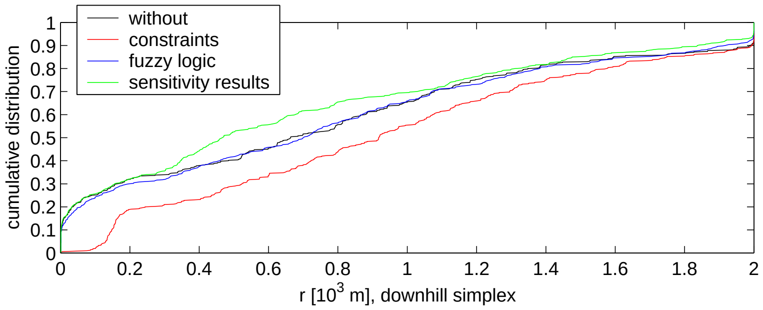

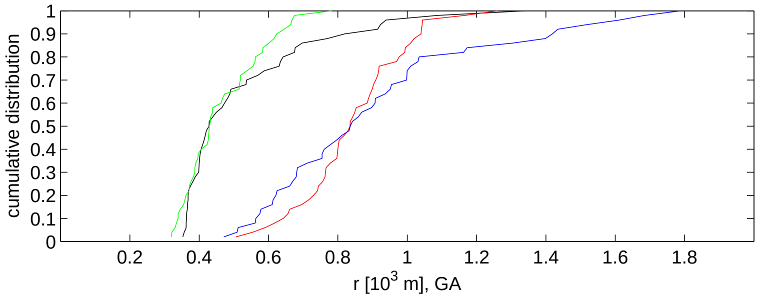

Figure 6.47: Cumulative distribution of r, generated with downhill simplex and GA samples, applying all kind of improvement approaches.

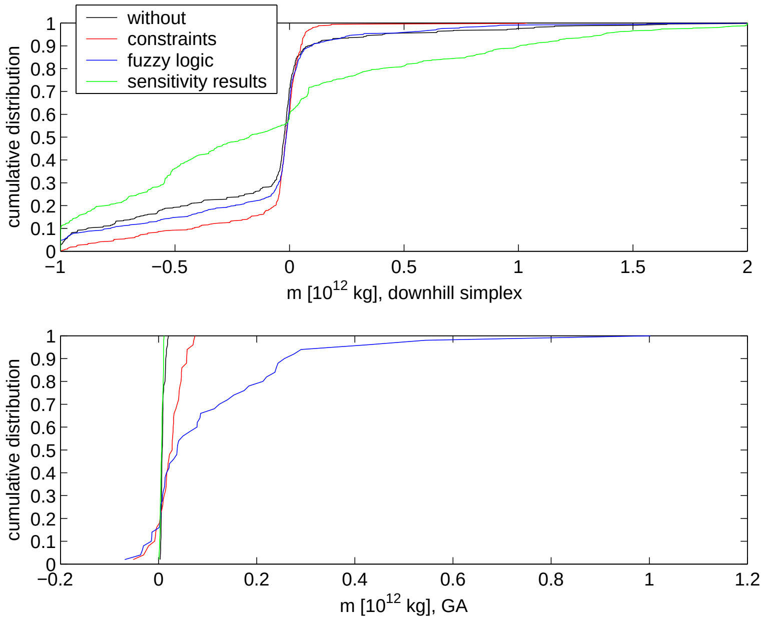

Figure 6.48: Cumulative distribution of m, generated with downhill simplex and GA samples, applying all kind of improvement approaches.

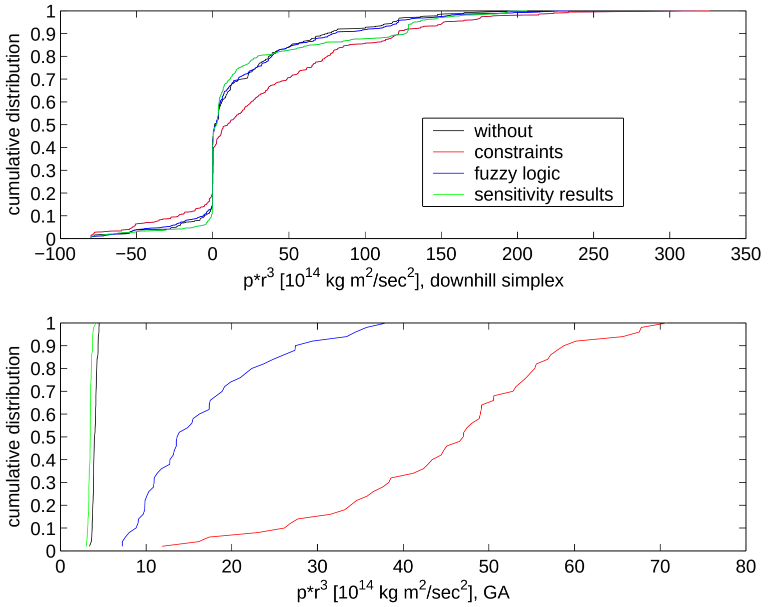

Figure 6.49: Cumulative distribution of $p \cdot r^3$, generated with downhill simplex and GA samples, applying all kind of improvement approaches.

unknown parameter	downhill, no improvement	downhill with constraints	downhill with sensitivity res.	downhill with fuzzy
ξ [10^3 m]	438.822	439.500	438.839	438.836
ψ [10^3 m]	9166.486	9166.100	9166.502	9166.496
ζ [10^3 m]	0.010	0.599	0.040	0.011
p [10^5 Pa]	-2.050230	91.297697	-8.016145	-8.977567
r [10^3 m]	0.607	0.599	0.385	0.317
m [10^{12} kg]	-0.000310	0.009955	-0.000095	-0.000058
$p \cdot r^3$ [10^{14}N·m]	0.4585	19.6219	0.4575	0.2860
reliability [%]	43.99	26.09	43.14	43.95
$1/\chi(dg)^2$	0.06510	0.08032	0.06596	0.06757
$1/\chi(uz)^2$	0.03419	0.03135	0.00939	0.03014
$1/\chi(ux)^2$	0.00378	0.00946	0.00393	0.00396
$1/\chi(uy)^2$	0.00579	0.00180	0.00780	0.00596
$1/\chi(comp)^2$	0.01098	0.00755	0.01048	0.01129
T(80,74)	1.50673	3.94300	1.50842	1.78499
mean $1/\chi(comp)^2$	0.00551	0.00541	0.00447	0.00564
min $1/\chi(comp)^2$	0.00291	0.00290	0.00076	0.00291

unknown parameter	GA, no improvement	GA with constraints	GA with sensitivity res.	GA with fuzzy
ξ [10^3 m]	439.320	439.638	439.301	439.422
ψ [10^3 m]	9166.222	9166.028	9166.220	9166.173
ζ [10^3 m]	0.070	0.685	0.080	0.141
p [10^5 Pa]	77.315134	95.057112	46.152149	16.848555
r [10^3 m]	0.369	0.656	0.428	0.754
m [10^{12} kg]	0.006220	0.035056	0.004574	0.004284
$p \cdot r^3$ [10^{14}N·m]	3.8846	26.8347	3.6185	7.2223
reliability [%]	42.28	23.87	42.00	40.18
$1/\chi(dg)^2$	0.08251	0.04771	0.08258	0.07776
$1/\chi(uz)^2$	0.04359	0.03404	0.03994	0.04207
$1/\chi(ux)^2$	0.01596	0.00926	0.01540	0.01647
$1/\chi(uy)^2$	0.00195	0.00177	0.00195	0.00191
$1/\chi(comp)^2$	0.00865	0.00731	0.00864	0.00852
T(80,74)	2.31169	3.56072	2.31747	2.29026
mean $1/\chi(comp)^2$	0.00864	0.00692	0.00857	0.00802
min $1/\chi(comp)^2$	0.00863	0.00644	0.00830	0.00706

Table 6.23: Comparison of all sampling approaches.

Summarizing, each algorithm has drawbacks but also advantages. Generally, the downhill simplex is on the one hand a fast optimization tool whose probability to reach a global optimum is increasing with increasing the number of restarts, accompanied by an increase in computation time. On the other hand the GA, which is more time consuming, determines most of the unknown input parameters with a very small dispersion.

Table 6.23 shows the samples with the best fit determined by the different optimization approaches. In addition, the minimum, maximum and mean fitness, the determined $p \cdot r^3$ values, the F-test result as well as the reliability for each model are given.

Analyzing and comparing the models with the best fit result in the following conclusions about the general model as well as about the improvement approaches:

Comparing the best results determined by the downhill simplex with the ones which had been generated by the GA approach, it becomes obvious that although the GA is said to be a global optimization algorithm, the optimal result which is computed by downhill simplex samples shows a better fit. Figure 6.50 displays the results of the fitness function $1/\chi(comp)^2$, computed for an area $437.822 \cdot 10^3 \leq \xi \leq 439.822 \cdot 10^3$ m and $9165.486 \cdot 10^3 \leq \psi \leq 9167.486 \cdot 10^3$ m, whereby all other input parameters determined by the downhill simplex approach without implying improvement approaches (Table 6.23) are kept fixed. In comparison to this, Figure 6.51 displays the results of the corresponding GA samples in a region $438.320 \cdot 10^3 \leq \xi \leq 440.320 \cdot 10^3$ m and $9165.222 \cdot 10^3 \leq \psi \leq 9167.222 \cdot 10^3$ m. The model with the high fitness, which is found by the downhill simplex samples, covers only a very small area, surrounded by steep low fitness regions which occur at the positions where the other observation points are located, see Chapter 6.2.1, Figure 6.5. In comparison to this small optimum, the optimum found by the GA approach is much larger and better to detect. This behavior shows that the downhill simplex

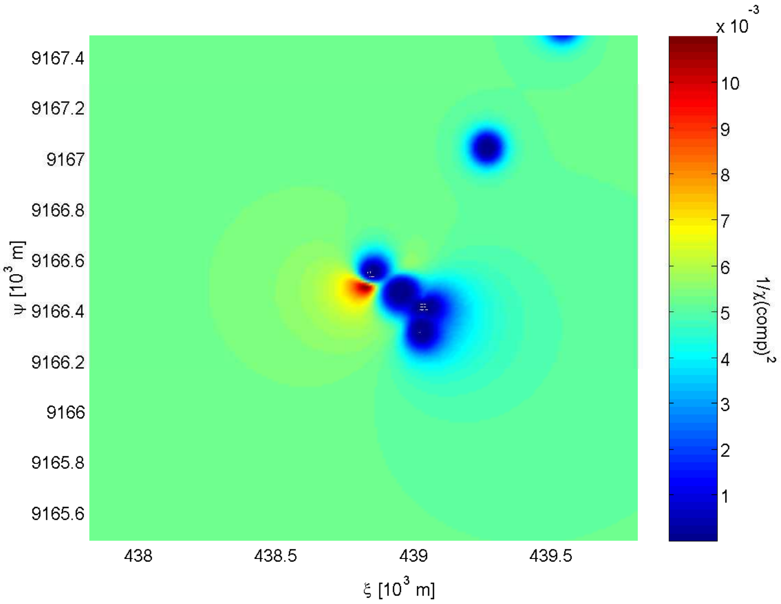

Figure 6.50: $1/\chi(comp)^2$, computed in the region 1000 m around the best solution, given in Table 6.23 of the downhill simplex samples, anticipating no improvement approach.

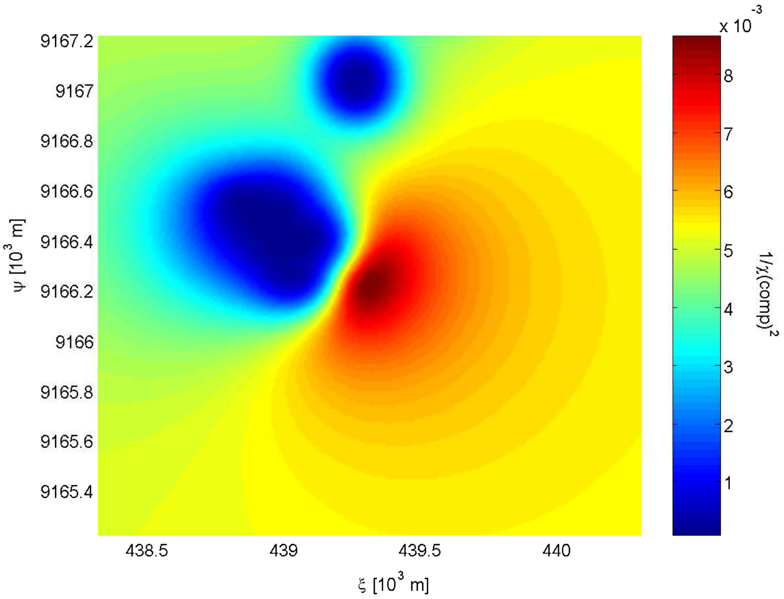

Figure 6.51: $1/\chi(comp)^2$, computed in the region 1000 m around the best solution, given in Table 6.23 of the GA samples, anticipating no improvement approach.

approach results indeed in a larger fit but also shows a very local effect, which is due to the fitting of one large displacement, observed in the north component of point no. 3 (compare Figure 6.35 with Figure 6.39). The good fit of this displacement causes all other observed signals to not be modeled as well with the downhill simplex model as it could be done with the GA models. So, these results of the downhill simplex approach lead to the best fit but reflect the modeling of a local signal. By applying the constrained downhill simplex approach the algorithm also determines the model results which are determined by the GA approaches. Also this behavior indicates that the models carried out by the GA approach reflect a better global fit and are more likely.

Due to the reason that GAs compute the optimization population based, it is more likely to locate the global optimum than with the downhill simplex method. A further aspect is that GAs are, due to their parallel processing of individuals, crossover and mutation, less sensitive against initial values of the unknowns. Nevertheless, the algorithm shows difficulties to detect very small optimal regions like the downhill simplex approach does. The result carried out by the downhill simplex approach shows a very small and steep characteristic, whereby the result developed by the GA show a large area of large objective function values. The GA shows a similiar behaviour to integration and smoothing, whereby the downhill simplex is acting similiar to differentiation: In the GA generated models the results adapt to all measurements best, the downhill simplex adapts to a local signal like the large displacement in the north component of observation point no. 3. The reason for not detecting these small regions of optimal solution spaces by the GA cannot be related to the working precision of crossover or mutation and it is not related to the Monte Carlo sampling, because all these techniques use the incremental solution which is given by double precision values. Due to the applied Elitism principle also small optimal solutions are transported from one to another generation, so the GA is keeping this solution found once. The only reason for not detecting this small and steep optima can be that the generation or population size is too small. Due to the reason that the GA is beginning with a highly probabilistic search, which is turning more and more to a deterministic one, the possibility to detect this small optimum at the beginning of the optimization is more likely than later on.

Several attempts have been tested to let the GA approach find the optimum which has been found by the downhill simplex samples in order to verify if the increase of the probabilistic behavior at the beginning of the algorithm would lead the process run in this very small optimum. In detail

- the population size has been increased to a number of 1000.
- the size of generation has been increased to 5000.
- the increase of the probability of mutation has been increased from 45% until 75% within 10% increments in order to increase the probabilistic property of the GA.
- the randomly generated initial values of the first population includes the optimal solution of the downhill simplex method.

Concluding the results of these different configurations, neither the size of population or generation nor the probability of mutation could cause a difference in the results of the GA approach. Only the implementation of the downhill simplex model parameters into the initial generation of the GA could force the algorithm to determine this point, which shows up the included Elitism principle. Although, if the results which were computed by the GA in this special application are more reliable due to its more global adaption to the observed data, one has to keep in mind that a GA is able to run in a local optimum, especially if the global one is very small. The computation time for detecting this kind of very small optimum would lead to a very time consuming approach, whereby the downhill simplex could evaluate these results faster.

To prove if the results of the downhill simplex approach describes mainly the north component of observation point no. 3 which is more or less an outlier of the observation, the downhill simplex approach has been restarted without implying improvement approaches but anticipating L_1-Norm, see Chapter 3, Equation 3.3 for the objective function's minimization. The results show clearly that due to the different anticipated norm a more global result could be evaluated, so the best generated model (generated with downhill simplex approach without implementation of improvements but anticipating L_1-Norm) with $1/\chi(comp)^2 = 0.00818$ shows similar source values like the ones determined by the GA approaches ($\xi = 439.244 \cdot 10^3$ m, $\psi = 9166.220 \cdot 10^3$ m, $\zeta = 0.105 \cdot 10^3$ m, $p = 29.5239 \cdot 10^5$ Pa, $r = 0.422 \cdot 10^3$ m, $m = 0.002881 \cdot 10^{12}$ kg).

Summarizing all results concerning the effectiveness of the optimization approaches as well as the dispersion of the results lead to the conclusion that the optimization approach consisting of the GA optimization with the implementation of the sensitivity analysis results computes the smallest dispersion for all unknown parameters. The downhill simplex approaches are not furthermore used due to the large dispersion of the unknowns. The likelihood to run into a local minimum is highly dependent on the initial starting values of these approaches, and the optimal solution shows a very local adaption, whereby the task is given by the determination of the most valuable global model which fits all observations or data points as best as possible.

The influence of the implemented fuzzy logic controller into the optimization could not result in more reliable models. Furthermore, some models which are determined without this kind of improvement are located in a region which is related to a higher physical reliability. This problem can be fixed by increasing the multiplication factor λ in the maximization of the objective function in order to increase the weight of the fuzzy logic system in the objective function computation, TIEDE *et al.* (2005c). But this seems at the moment not appropriate, because the fuzzy logic can only give a reliability concerning the position of the source right now. If more data are implied into the fuzzy logic controller, especially additional data from different geophysical and chemical observation techniques which also allow a combination of the position of the source with the pressure and mass component in future, the active implementation into the optimization itself can become very meaningful for the determination of physical reliable models. At the moment the fuzzy logic is mainly based on the density model and some position based plausibility checks of the unknown source and should therefore be used only passively. The passive implementation is investigated by the computation of the physical reliability of the derived model parameters.

Finally, the combination of the implied results of sensitivity analysis into the GA approach with the passive implementation of the physical reliability for the final model computed by the fuzzy logic seems to be the most appropriate strategy to determine the source parameters. By decreasing the dispersions of the unknown parameters and defining a physical reliability for the source model, the quality of the model is increased statistically (smaller dispersion) and can be given by a physical reliability.

To summarize the adaption of the determined model to the data, all models which were determined by the optimization approaches consist of a very small mass in a very shallow source compared to high energy effects (described by $p \cdot r^3$). These results lead to the assumption that the system is mainly dominated by pressure rather than mass effects. The approach to constrain the value of the radius component to set it smaller than the depth results in the same information but within a smaller fit of the models: The source is supposed to be very shallow with a very small mass. These results can be verified by a similar tendency resulting out of approximations of the mass change which had been computed in Chapter 6.2.1, Table 6.2.

The shallow depth as well as small mass components fit very well to the results which were determined by former modeling approaches by KÖRNER (2000). He anticipated a depth of only a few hundred meters, modeled by GPS and tilt data, whereby the shape of the magmatic source does not influence the modeling results. The magmatic mass is according to KÖRNER (2000), very small. Shallow magma chamber depths are also anticipated by CAMUS *et al.* (2000) and REBSCHER *et al.* (2000), who could not find any evidence for magma sources deeper than 1000 m below the summit by analyzing GPS and tilt data. KÖRNER (2000) anticipated pressure values between 30-40$\cdot 10^5$ Pa and a vertical extension of the source between 100 and 200 m as well as a horizontal extension between 200 and 600 m. These values result in an approximated energy values between $0.624 - 0.832 \cdot 10^{14}$ kg$\cdot$m^2/sec^2 for the source. Comparing these values with the resulting energy values given in Table 6.23 for the GA approaches, leads to the conclusion that all energy effects responsible for the displacements are determined too large. In order to decrease these values, the assumption has to be made that an additional effect which causes the displacements is latent.

Comparing the position of the sources determined by the GA with the geological structure of Merapi, leads to a very interesting connection: All these computed sources are located SE from the summit near the area in which the two fumarole fields Gendol and Woro are located. Furthermore all the determined depths of the sources are very shallow. If the model is related directly to the fumarole fields or to a magma chamber below cannot be distinguished yet. The very small mass of all sources might be an indicator that the models reflect the fumarole fields and do not consist of a magmatic source at all, but also a magmatic source in the area of the fields where degassing could be observed is likely. In comparison, these similarities cannot be seen in the results of the downhill simplex approaches where the sources are located NW as well as SE, at a greater distance.

Summarizing, the small mass values as well as the too large energy effects accompanied with a small fit of large displacements in the summit region, lead to the assumption that the main factor which is causing the observed displacements is not solely related to a magmatic source. Therefore, a refinement of the anticipated model is investigated.

6.5 Combined Final Model of Merapi

The small fit (given by the small significance level of 0.01%) of the model approaches described in Chapter 6.4 leads to the assumption that the underlying physical based mathematical model described in Chapter 2.1 does not reflect reality properly. Therefore, the physical based mathematical model has been enlarged by anticipating the existence of a fracture zone in the summit region which is modeled by a combined dip-slip/strike-slip fault. Due to this anticipation, the energy defined by $p \cdot r^3$ is also assumed to decrease, so it will fit better to former modeling approaches by KÖRNER (2000). Figure 6.52 shows the area of the summit region, where the large dots indicate the observation points. For each point, the three-dimensional displacements are given in the small overviews in [m]. Due to the NE movement of observation point no. 3, whereby all other points move into SE direction or show no significant horizontal movement at all, a strike-slip fault has been anticipated which separates observation point no. 3 from the other observation points. In addition, a downlift motion in observation point no. 1 is observed, whereby all other points are characterized by an uplift movement. In order to model this behavior, an additional dip-slip fault is anticipated. Both kind of faults are supposed to interact at the same location in order to avoid the modeling of too local effects and the decrease of the degrees of freedom in the optimization. In the

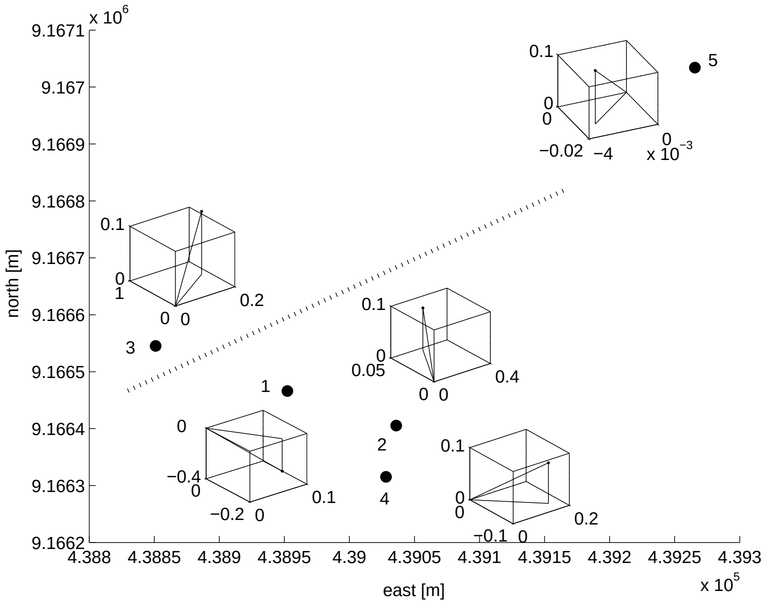

Figure 6.52: Overview of the summit region with three-dimensional displacements at each point and the anticipated direction of the fault zone shown as dotted line.

optimization approach the eight additional unknown parameters, midpoint in east (1) and north (2) direction, dip-slip fault movement (3), semi length of the fault (4), depth of the bottom of the fault (5), dip (6) and strike (7) angle, as well as the strike-slip fault(8) are added. All parameters are given in [m] except (6) and (7) which are given in [rad]. The physical based mathematical model described in Chapter 2.2, anticipating both faults, has been implemented into the GA approach without any improvement approaches due to the reason that all these approaches are based on the underlying source model, described in Chapter 2.1. The two models are superposed. The main reason for dividing the optimization has been that initial optimization approaches, in which all 14 unknown parameters had been determined in one step, failed. The samples could not be stabilized. Two reasons for this effect can be possible: First the configuration parameters of the GA are too small. In that case, they have to be drastically increased in order to get stable results for the unknown parameters in a combined optimization approach in which fault as well as source parameters are optimized at the same time. The second point might be that the number of unknowns compared to the number of significant observations in the summit region, becomes very high, so the degrees of freedom is getting very small. Furthermore, it might be that the two models are not independent. Neglecting the possibility of dependent models, the final model is computed by superposition, so the final optimization is determined in two steps:

In the first step, the fault effects are determined and subtracted from the original observations. In the further step these residuals are taken in order to optimize the elastic-gravitational model. By only anticipating the fault in the first optimization step the samples showed only small dispersion, so the unknown input parameters could be determined very stably.

The combined dip-slip/strike-slip fault effects are computed by 30 GA samples with a chosen generation size of 30000, a population size of 200 and the given parameter bounds in Table 6.24, which are anticipated according to first analyses of the displacements, evaluated from Figure 6.52. The distribution of the sampling is given in Figure 6.53, where all parameters could be determined with only small dispersions which is the reason why no further attempts have been investigated to improve the optimization process. The fault model with the best fit of $1/\chi(comp)^2 = 0.03249$ has been tested by F-test according to Chapter 6.3, Equation 6.5. The model fits the data with a significance level of 10% ($T_{fault(GA)} = 1.15919 < F(0.90, 72, 80) = 1.34666$). In the next step, these fault effects are subtracted from the original observation. The resulting residuals served as input for the final optimization of the elastic-gravitational source model. Due to the fact that the observed values are replaced by the residuals, the implementation of the sensitivity analysis results into the GA approach cannot be applied in this final optimization. So, the result of this final modeling has to be compared with the model which is determined by the GA approach without anticipating improvements. The

Parameter	lower bound	upper bound
east component of midpoint[10^3 m](1)	437.5	440.5
north component of midpoint [10^3 m](2)	9165	9168
dip slip [m](3)	-1	1
semi length of fault [m](4)	0	500
depth of bottom [m](5)	0	500
dip angle [rad](6)	0	$< \pi/2$
strike angle [rad](7)	0	2π
strike slip [m](8)	-1	1

Table 6.24: Parameter limits for the strike-slip/dip-slip fault.

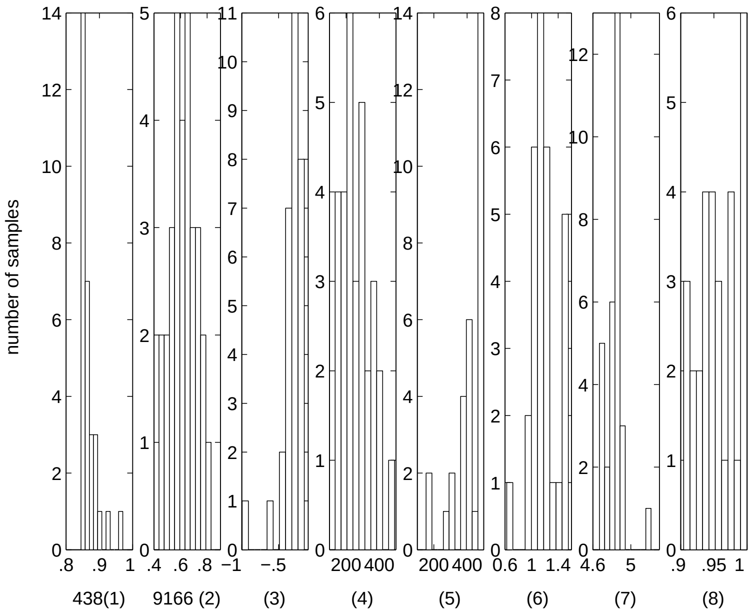

Figure 6.53: Histogram showing the distribution of the unknown fault parameters determined by 30 GA optimization approaches.

optimization of the source model has been investigated by 30 GA samples, anticipating the configuration which were determined in the synthetic modeling approach. These samples result in a larger dispersion of the unknown input parameters, which is caused by the small residuals that serve as input values of the optimization approach. Nevertheless, a best model according to the fitness of $1/\chi(comp)^2 = 0.04145$ is determined. Also the fit of this model to the data (the residuals) is tested by F-test and results in $T_{source(GA)} = 3.57157 > F(0.9999, 72, 80) = 2.40582$, so the elastic-gravitational model does not fit the residuals with the given significance level. By superposing both effects and applying F-test to the final model, it can be seen that the final model results in a better fit than the fault model solely ($T_{combined(GA)} = 1.12200 < F(0.90, 66, 80) = 1.34953$), so the elastic-gravitational model which is itself not significant is not rejected. Figure 6.54 shows the modeled effect of the combined fault (dotted line) as well as the complete model (straight line). The complete model consists of fault effects as well as the elastic-gravitational source effects (observed data displayed as red line with 1σ-error bars). Figure 6.54 shows clearly that the main effects are modeled by the fault and that the inclusion of the elastic-gravitational model causes only a small increase in fitness which confirms the F-test statistics result. The high fit of the fault model underlines the hypothesis of an additional effect beside the former anticipated elastic-gravitational model. Table 6.25 summarizes all parameters of the final model, including the degrees of freedom and $1/\chi(comp)^2$ values for each model. Furthermore, the corresponding reliability of the final model with respect to the position of the elastic-gravitational source is given and all models are tested by applying the F-test, anticipating a significance level of 10% for the fault effect and the combined model as well as 0.01% for the elastic-gravitational source.

Figure 6.55 shows both modeled effects. Note: Both effects are modeled concerning a homogeneous half-space. The elastic-gravitational source is shown as a sphere whereby the half-space is anticipated at an ellipsoidal height = 0 m. In the middle of the body the mass is acting as a point source, but no conclusions can be

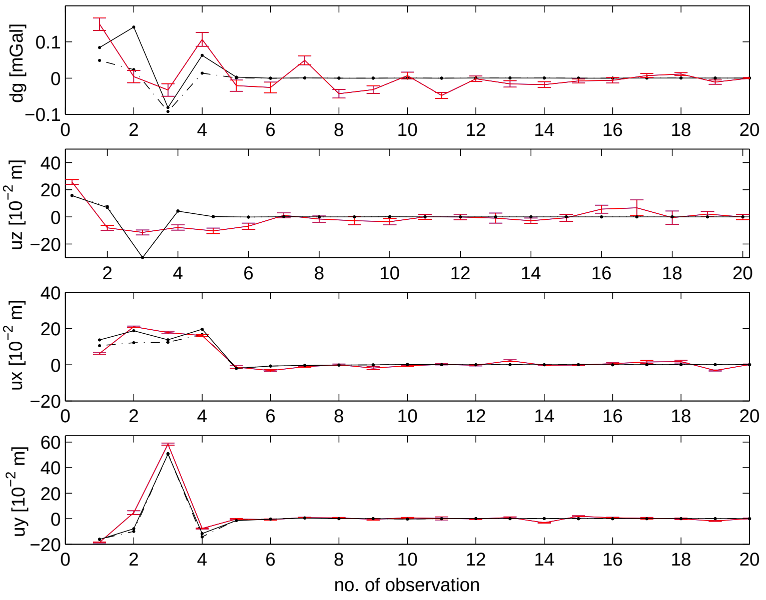

Figure 6.54: Modeled effects of the fault and the complete final model consisting of fault and source effects compared to the original observation data (dashed line=fault model, straight line=combined model, red line=observations including 1σ-error bars).

drawn about the shape of the body.

Also, the inclusion of the fault effects into the model does not change the position of the elastic-gravitational source model significantly (compared to the position determined by the GA approach without any implied improvement approaches, Chapter 6.4.3, Table 6.23). It can be seen that the position of the elastic-gravitational source is only moving slightly in the NW direction. The source is becoming more shallow, including a smaller energy effect as well as a smaller mass, see Table 6.23.

The comparison of $p \cdot r^3 = 0.2730 \cdot 10^{14}$ kg·m^2/sec^2 of this source model with the anticipated values between $0.624 - 0.832 \cdot 10^{14}$ kg·m^2/sec^2 which are derived from pressure and radius anticipations given by Körner (2000) results in a better fit of the energy form than former results. Nevertheless it has to be mentioned that the increase of fitness due to the elastic-gravitational model is very small but still significant. The significance of the final model is tested by applying F-test statistics and results in the acceptance of the H_0-hypothesis which states that the model fits the observed data with a significance level of 10% ($T_{combined(GA)} = 1.12200 < F(0.90, 66, 80) = 1.34953$).

Figure 6.56 displays the summit region of Merapi between $438.6 \cdot 10^3 \leq \xi \leq 439.3 \cdot 10^3$ m and $9166.1 \cdot 10^3 \leq \psi \leq 9166.7 \cdot 10^3$ m , whereby the topographic map according to Beauducel *et al.* (2000) is taken as a basis. The modeled upper ridge of the fault is shown as a straight line. It can be seen, that the fault coincides very well with the fault zone which had been previously determined. The elastic-gravitational source is in the vicinity of the fumarole fields Woro and Gendol as well as near the shown ash platform in Figure 6.56. Due to the small mass change of the determined source, a magmatic source is still very unlikely. Therefore, the explanation of the source model with the fumarole field seems to be more appropriate. The source model might reflect changes in the fumaroles like the increase in the amount of

magma source model	**parameter**
ξ [10^3 m]	439.183
ψ [10^3 m]	9166.453
ζ [10^3 m]	0.020
p [10^5 Pa]	51.831045
r [10^3 m]	0.174
m [10^{12} kg]	0.003326
$p \cdot r^3$ [10^{14} kg$\cdot$m^2/sec^2]	0.2730
reliability	43.70
degrees of freedom	74
$1/\chi(comp)^2$	0.04145
$T_{source(GA)}(72{,}80)$	3.57157
dip-slip/strike-slip fault model	
east of midpoint [10^3 m]	438.847
north of midpoint [10^3 m]	9166.437
min. depth from the top [10^3 m]	0
max. depth from the top [10^3 m]	0.398
semi length [10^3 m]	0.142
dip angle [rad]	1.552944
strike angle [rad]	4.748854
normal slip [m]	-0.588
strike slip [m]	0.993
degrees of freedom	72
$1/\chi(comp)^2$	0.03249
$T_{fault(GA)}(72{,}80)$	1.15919
combined model	
degrees of freedom	66
$1/\chi(comp)^2$	0.03800
$T_{combined(GA)}(66{,}80)$	1.12200

Table 6.25: Parameters of the final model.

fluids and also an anticipated increase of the gas pressure in the field.

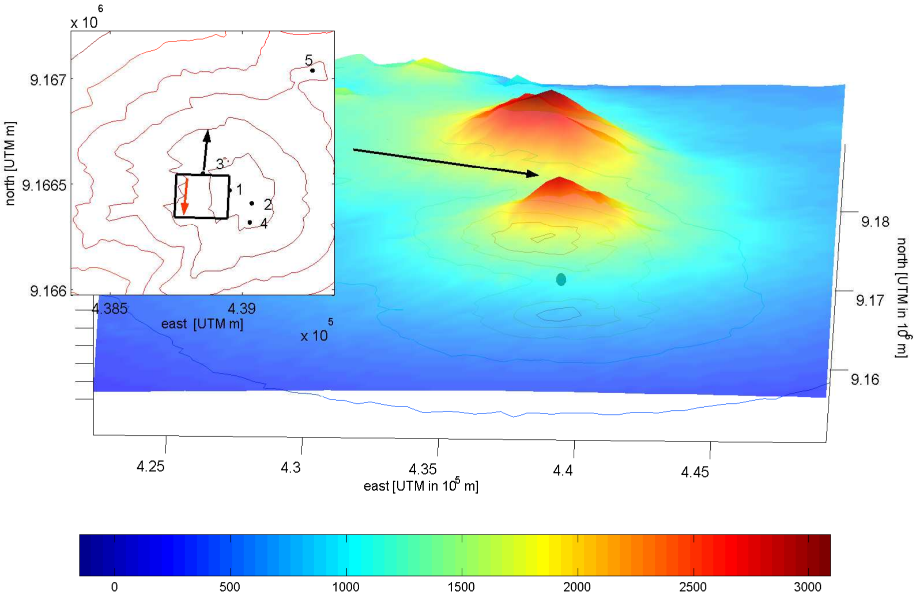

Figure 6.55: Three-dimensional view of Merapi showing the final model including an elastic-gravitational source (black sphere) as well as a normal fault (red arrow) extensional (black arrow).

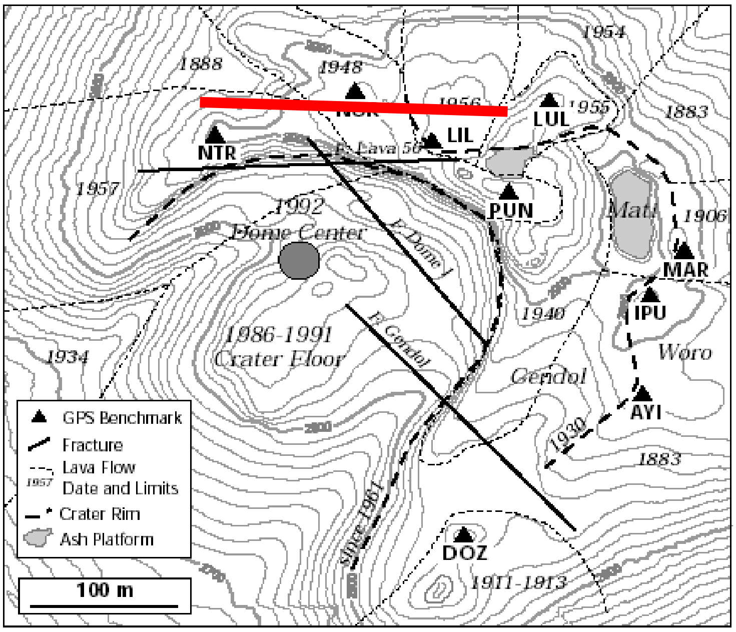

Figure 6.56: Final model showing the modeled fault zone as a red line and the map of the summit region from BEAUDUCEL *et al.* (2000) with fracture zone as dark lines.

Chapter 7

Results and Conclusions

The thesis presented improvement approaches for optimization attempts applied to geodetic data from Merapi volcano, Java, Indonesia. The flow chart given in Figure 7.1 summarizes the general procedure of the investigated optimization approaches.

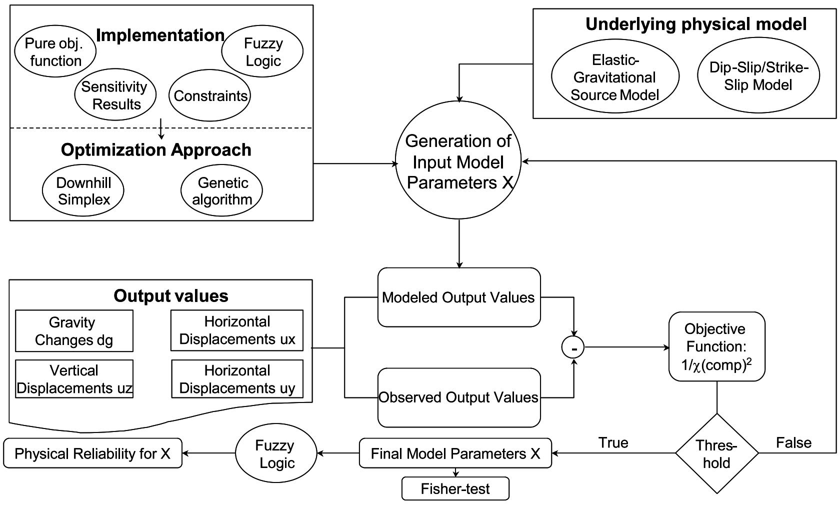

Figure 7.1: Flow chart summarizing the investigated optimization approaches

The study concentrates on the following three aspects:

- Evaluation of improvement techniques for the applied downhill simplex as well as the GA optimization approach.
- Comparison of downhill simplex and GA optimization results with the definition of a recommended optimization approach.
- Generation of a structural model for Merapi, determined from the geodetic observations observed in 2000 and 2002.

The modeling attempt is based on the generalized static Navier equations which couple elastic and gravitational effects in a homogeneous half-space. Due to the multimodality of the objective function and the poor knowledge about the relation between in- and output data of this system, extensive uncertainty and sensitivity analyses have been investigated in order to evaluate a deeper insight into the behavior between the unknown input parameters of the physical based mathematical model and the modeled output values. The computation of TSIs for each kind of output values and the information that some unknown parameters only could be computed with a large dispersion, an improvement of the optimization approach, including the sensitivity analysis results, has been investigated and proved. It can be stated that this attempt leads to an optimized sampling result with smaller dispersions for the unknown input parameters. Furthermore, the RSA shows that with increasing fitness, the sensitivity against the unknown parameters changes significantly, which reflects a further increase of complexity of the elastic-gravitational model.

A further improvement approach of the optimization concentrates on the definition of physical constraints, by anticipating a spherical elastic-gravitational source model. These constraints are implied into the optimization as penalty terms. This attempt does not cause any improvement in the determination of the unknown input parameters.

The last improvement attempt consists of a fuzzy logic model which fuses physical plausibility checks and other geophysical available data of Merapi. Configuration runs with the active implementation of the fuzzy logic controller into the optimization could not lead to any improvement of the optimization results. This information is recommended in its actual condition to implement passively by computing the physical reliability for the determined model which follows out of the optimization. Meaningful results are expected if more geophysical and chemical information are included in the fuzzy logic, especially information which can give a connection between the position and the pressure component of the source.

The comparison of the downhill simplex and the GA approach leads to the following conclusions: The downhill simplex optimization shows in all approaches a large dispersion of the unknown input parameters, which reflects the local property of the algorithm. By restarting the process several times the probability that the algorithm runs in a local optimum is reduced. On the other hand, the algorithm loses the appeal of being a fast optimization tool. The main advantage compared to the GA approach becomes negligible. Furthermore, the downhill simplex runs into local models with an adaption to single large signals, whereby this behavior can be avoided by applying a smaller norm in the optimization. The GA approach could determine models with small dispersions of the unknown parameters. Although the algorithm is very slow, the results are more reliable.

The source of the best model is located in the area of the Woro fumarole SE of the summit which can explain the very shallow source with only a small mass. Two possible explanations of the body are given, where the first one seems to be more likely: The body is describing the fumaroles, so the very small mass change is related to fluid changes in the fumaroles and the energy effect to building up of gas. The second possible explanation is given by a very small magmatic body which is situated in the area of the fumaroles.

Nevertheless, all optimization approaches also reflect that the considered source of the elastic-gravitational model does not explain the observed data properly. In addition to the bad fitness, the observed properties of the modeled source, determined by all optimization approaches, suggests an additional source that is responsible for the observed displacements. This additional effect is modeled as a fault zone, a combined strike-slip/dip-slip fault in the summit region. The final model consists of a superposition of the fault zone and an elastic-gravitational source. This combined model leads to a good fit to the observed data, where the location of the fault is also conform with previous results given in the literature. The source model, which only reflects a minor effect of the observed data, is characterized by a smaller mass and energy effect $p \cdot r^3$ than the previous models. Hereby, the value of $p \cdot r^3$ also conforms with computed energy values from the literature. The source is still located in the area of the fumarole field, so the final conclusion leads to the assumption that the small modeled effects are caused by the fumaroles and are not related to a magmatic source.

Finally, it has to be pointed out that the analytical modeling approaches cannot be refined in more detail due to the limited number of significant observations. The splitting of the faults in the summit area would lead to the modeling of very local effects which might be represented by only one observation (e.g. observation point no.3 north deformation, observation point no.1 height deformation).

Summarizing, the main benefit of this study is the fusion of optimization approaches with the results which follow from the uncertainty and global sensitivity analysis. This fusion ends up in an improved modeling approach with decreased dispersions of the unknown input parameters. Moreover, the evaluation of the improvement technique can be applied to all optimization approaches, in which different kind of output values with different sensitivities concerning the unknown input parameters of the model are used, and in which the unknown input parameters could not all be determined equally accurately with the optimization approach. The second advantage is given by the generation of the fuzzy logic system, which can be used in order to verify a certain anticipated source model for Merapi. At the moment the physical reliability computed by the fuzzy system is only related to the position of the source. But the model has the appeal that it can be easily enlarged by additional available information in order to increase the reliability of the system. Furthermore, by defining other output values, the system can give a reliability for a various number of different modeling approaches at Merapi.

Chapter 8

Further Need of Research

Further investigations should be started in the future work to refine the fuzzy logic with respect to input data which can give information about the pressure, radius and mass of the elastic-gravitational model but also about the unknown parameters of the fault model. The implementation of results which are given especially by chemical observations, Zimmer and Erzinger (2003) as well as magnetotellurics, Müller and Haak (2004) shall be implied into the fuzzy logic controller. In that way, the physical significance of the model can be enlarged and the fuzzy logic can be applied actively with a higher weight factor into the optimization algorithm. This implementation will lead to a model approach which results in physically more reliable models.

The computation of TSIs via a global sensitivity analysis concerning both models, the elastic-gravitational as well as the strike-slip/dip-slip fault model, can give important results. Because of the fact that a combined optimization approach failed, the possibility is given that the two models are coupled. This coupling can be determined by applying a global sensitivity analysis.

Due to the results of the RSA the investigation of an adaptive improvement of the GA approach with respect to the varying sensitivities with increasing fitness could lead to very interesting results and should be tested.

Furthermore, the study showed that the underlying physical model, which is based on an elastic-gravitational source located in a homogeneous half-space, could not explain the measured changes in position and gravity properly. Because the magmatic source is described by only small masses accompanied by a shallow depth and dominating energy values of the source, the shape of the magmatic source should be changed from a point source into a plate source in next modeling attempts. Such a source would be described by a more realistic shape, especially due to the anticipation that the modeled effects are related to the fumarolic fields and not to a single magma chamber.

Finally, a combined optimization approach should be tested in which the results of the combined sensitivity analysis as well as the enlarged fuzzy logic model and the Fisher-test statistics are implemented actively. With this approach it should be possible to compute statistically significant and also physically reliable model parameters.

Bibliography

Aggarwal, C., A. Hinneburg and D. Keim (2001): *On the surprising behavior of distance metrics in high dimensional spaces*, Proceedings of the International Conference on Database Theory (ICDT), volume 1973 of Lecture Notes in Computer Science, 420–434.

Allard, P. (1982): *Stable isotope composition of hydrogen, carbon and sulphur in magmatic gases from rift and island arc volcanoes*, Bull. Volcanol., 45: 269–271.

An, P., W. Moon and A. Rencz (1991): *Integration of geological, geophysical and remote sensing data using fuzzy logic*, J.Can.Soc.Expl.Geophysics, 27: 1–11.

Bäck, T. (1996): *Evolutionary Algorithms in Theory and Practice*, Oxford University Press, New York.

Bäck, T., A. Eiben and N. van der Vaart (2000): *An empirical study on GAs without parameters*, in: *Parallel Problem Solving from Nature-PPSN VI International Conference, Paris, France*, 315–324, Springer.

Bäck, T., F. Hoffmeister and H.-P. Schwefel (1991): *A survey of evolution strategies*, in: *Proc. of the 4th International Conference on Genetic Algorithms, San Diego, CA*, 2–9.

Baker, J. E. (1987): *Reducing bias and inefficiency in the selection algorithm*, in: Grefenstette, J. J. (Ed.), *Genetic algorithms and their applications: Proc. of the Second Int. Conf. on Genetic Algorithms*, 14–21, Lawrence Erlbaum Assoc., Hillsdale, NJ.

Battaglia, M. and P. Segall (2004): *The interpretation of gravity changes and crustal deformation in active volcanic areas*, Pure Applied Geophysics-in press, 161(7).

Beauducel, F. and F. Cornet (1999): *Collection and three-dimensional modeling of GPS and tilt data at Merapi volcano, Java*, Journal of Geophysical Research, 104: 725–736.

Beauducel, F., F. Cornet, E. Suhanto, T. Duquesnoy and M. Kasser (2000): *Constraints on magma flux from displacements data at Merapi volcano, Java, Indonesia*, Journal of Geophysical Research, 105: 8193–8204.

Beck, M. (1987): *Water quality modelling: a review of the analysis of uncertainty*, Water Resources Research, 23: 1393–1442.

Bemmelen, R. V. (1949): *The Geology of Indonesia*, General geology, Government printing office, The Hague, Amsterdam.

Bemmelen, R. V. (1956): *The influence of geologic events on human history (an example from Central Java)*, Verh. Kon. Ned. Geol. Mijnb. Genoot. Geol., 16: 20–36.

Berrino, G., G. Corrado, G. Luongo and B.Toro (1984): *Ground deformation and gravity changes accompanying the 1982 Pozzuoli uplift*, Bull. Volcanol., 47(2): 187–200.

Berthommier, P. (1990): *Etude Volcanologique du Merapi (Central Java): Téphrostratigraphic et Chronologie-Produits Éruptifs*, Ph.D. thesis, Université Blaise Pascal, Clement-Ferrand.

Beven, K. and A. Binley (1992): *The future of distributed models: model calibration and uncertainty prediction*, Hydrological Processes, 6: 279–298.

Bonafede, M. and M. Mazzanti (1998): *Modelling gravity variations consistent with ground deformation in the Campi Flegrei Caldera (Italy)*, Journal of Volcanology and Geothermal Research, 81(1-2): 137–157.

Brodscholl, A., S. Kirbani and B. Voight (2000): *Sequential dome-collapse nuées ardentes analysed from broadband seismic data, Merapi Volcano, Indonesia*, Journal of Volcanology and Geothermal Research, 100: 363–369.

Cagnoli, B. (1998): *Fuzzy logic in volcanology*, Episodes, 21: 94–96.

Camacho, A., F. Montesinos and R. Vieira (2000): *Gravity inversion by means of growing bodies*, Geophysics, 65: 95–101.

Camacho, A., F. Montesinos and R. Vieira (2002): *A 3-D gravity inversion tool based on exploration of model possibilities*, Computer and Geosciences, 28: 191–204.

Camus, G., A. Gourgaud, P.-C. Mossand-Berthommier and P.-M. Vincent (2000): *Merapi (Central Java, Indonesia): An outline of the structural and magmatological evolution, with a special emphasis to the major pyroclastic events*, Journal of Volcanology and Geothermal Research, 100: 139–163.

Chan, K., A. Saltelli and S. Tarantola (1997): *Sensitivity analysis of model output: Variance-based methods make the difference*, in: S. Andradttir, D. H. W., K. J. Healy and B. L. Nelson (Eds.), *Proceedings of the 1997 Winter Simulation Conference*, Atlanta GA.

Charco, M., J. Fernandez, K. Tiampo, M. Battaglia, L. Kellogg, J. McClain and J. Rundle (2004): *Study of volcanic sources at Long Valley Caldera, California, using gravity data and a genetic algorithm inversion technique*, Pure and Applied Geophysics in press, 161(7).

Commer, M. (2003): *Three-dimensional inversion of transient electromagnetic data: A comparative study*, Ph.D. thesis, University of Cologne.

Commer, M., S. Helwig, A. Hördt and B. Tezkan (2005): *Interpretation of long-offset TEM data from Merapi (Indonesia) using a 3D optimization approach*, Journal of Geophysical Research, 110.

Darwin, C. (1859): *The Origin of Species, by Means of Natural Selection or the Preservation of Favored Races in the Struggle for Life*, The modern library, New York.

Davis, P. (1986): *Surface deformation due to inflation of an arbitrarily oriented triaxial ellipsoidal cavity in an elastic half-space, with reference to Kilauea volcano, Hawaii*, Journal of Geophysical Research, 91: 7429–7438.

EA (1999): *Expression of the Measurement in Calibration*, European co-operation for Accreditation, EA-4/02.

Fernández, J., M. Charco, K. Tiampo, G. Jentzsch and J. Rundle (2001a): *Joint interpretation of displacement and gravity data in volcanic areas. A test example: Long Valley Caldera, California*, Geophysical Research Letters, 28: 1063–1066.

Fernández, J. and J. Rundle (1994): *Gravity changes and deformation due to a magmatic intrusion in a two-layered crustel model*, Journal of Geophysical Research, 99(B2): 2737–2746.

Fernández, J. and J. Rundle (2004): *Postseismic viscoelastic-gravitational half space computations: Problems and solutions*, Geophysical Research Letters, 31.

Fernández, J., J. Rundle, R. Granell and T.-T. Yu (1997): *Programs to compute deformation due to a magma intrusion in elastic-gravitational layered earth models*, Computer and Geosciences, 23: 231–249.

Fernández, J., K. Tiampo, G. Jentzsch, M. Charco and J. Rundle (2001b): *Inflation or deflation? New results for Mayon volcano applying elastic-gravitational modeling*, Geophysical Research Letters, 28: 2349–2352.

Fernández, J., K. Tiampo and J. Rundle (2001c): *Viscoelastic displacement and gravity changes due to point magmatic intrusions in a gravitational layered solid earth*, Geophysical Journal International, 146: 155–170.

Forrest, S. (1993): *Genetic algorithms: Principles of natural selection applied to computation*, Science, 261: 872–878.

Friedel, S., I. Brunner, F. Jacobs and C. Rücker (2000): *New results from DC resistivity imaging along the flanks of Merapi volcano*, in: Zschau, J. and M. Westerhaus (Eds.), *Decade-Volcanoes under Investigation*, vol. 4, 2329, Dt. Geophys. Gesellschaft.

Friedel, S. and F. Jacobs (2004): *Blick in den Vulkan*, Physik Journal, 3(11): 62–63.

Gerstenecker, C. (1990): *Mikrogravimetrische Untersuchung bei Couiza-Los Brugos, Frankreich*, Institute of physical Geodesy, Darmstadt University of Technology, Germany.

Gertisser, R. (2002): *Gunung Merapi (Java, Indonesien): Eruptionsgeschichte und magmatische Evolution eines Hoch-Risikovulkans*, Ph.D. thesis, Geowissenschaftliche Fakultät, Albert-Ludwigs-Universität Freiburg i.Br., Germany.

Goldberg, D. (1989): *Genetic Algorithms in Search, Optimization, and Machine Learning*, Addison Wesley, Reading, MA.

Götz, C. (2003): *Auswertung und Deformationsanalyse von GPS-Messungen am Vulkan Merapi auf Java, Indonesien*, Master's thesis, Institute of Physical Geodesy, Darmstadt University of Technology, Germany.

Gray, P., W. Hart, L. Painton, C. Philips, M. Trahan and J. Wagner (1997): *A survey of global optimization methods*, Master's thesis, Sandia National Laboratories, Albuquerque.

Gvishiani, A. and J. Dubois (2002): *Artificial Intelligence and Dynamic Systems for Geophysical Applications*, Springer, Berlin.

Hamida, S. and M. Schoenauer (2000): *An adaptive algorithm for constrained optimization problems*, in: *Parallel Problem Solving from Nature-PPSN VI*, 315–324, Springer, Berlin.

Hansen, N. (2000): *Invariance, self-adaption and correlated mutations in evolution strategies*, in: *Parallel Problem Solving from Nature-PPSN VI*, 355–364, Springer, Berlin.

Herrera, F. and M. Lozano (2000): *Adaptive control of the mutation probability by fuzzy logic controllers*, in: *Parallel Problem Solving from Nature-PPSN VI*, Springer, Berlin.

Hoffmann-Rothe, A., A. Mller, O. Ritter and V. Haak (1998): *Magnetotelluric survey at Merapi volcano and across Java, Indonesia*, vol. 3 of *Decade-Volcanoes under Investigation*, 47–52, Dt. Geophys. Gesellschaft.

Holland, J. (1975): *Adaption in Natural and Artificial Systems*, University of Michigan Press, Ann Harbor, Michigan.

Hornberger, G. and R. Spear (1981): *An approach to the preliminary analysis of environmental systems*, Journal of Environmental Management, 12: 7–18.

http1 (2005): http://igscb.jpl.nasa.gov/, (date: 04/2005).

IAVCEI (1994): *IAVCEI subcommission on Decade Volcanoes, research at Decade Volcanoes aimed at disaster prevention*, EOS, 75.

Jentzsch, G., R. Punongbayan, U. Schreiber, G. Seeber, C. Völksen and A. Weise (2001): *Mayon Volcano, Philippines: Change of monitoring strategy after microgravity and GPS measurements from 1992 to 1996*, Journal of Volcanology and Geothermal Research, 109: 219–234.

Jentzsch, G., A. Weise, C. Rey and C. Gerstenecker (2004): *Gravity changes and internal processes: Some results obtained from observations at three volcanoes*, Pure and Applied Geophysics, 161: 1415–1431.

Jong, K. D. (1975): *An analysis of the behavior of a class of genetic adaptive systems*, Ph.D. thesis, University of Michigan, Ann Arbor.

Jousset, P., S. Dwipa, F. Beauducel, T. Duquesnoy and M. Diament (2000): *Temporal gravity at Merapi during the 1993-1995 crisis: An insight into the dynamical behaviour of volcanoes*, Journal of Volcanology and Geothermal Research, 100: 289–320.

Kalscheuer, T. (2004): *Die Auswertung der LOTEM-Daten vom Suedhang des Merapi*, Diploma thesis, University of Cologne, Germany.

Koch, K. (2000): *Einführung in die Bayes-Statistik*, Springer, Berlin, Heidelberg.

Koch, O. (2003): *Transientelektromagnetische Messungen zur Erkundung einer Leitfähigkeitsanomalie am Vulkan Merapi in Indonesien*, Diploma thesis, University of Cologne, Germany.

Körner, A. (2000): *Deformationsmodelle nach Auswertung von Tiltmeter- und GPS-Daten am Vulkan Merapi (Indonesien)*, Ph.D. thesis, University of Potsdam.

Koshel, R. (2002): *Enhancement of the downhill simplex method of optimization*, International Optical Design Conference Technical Digest.

Love, A. (1911): *Some Problems in Geodynamics*, Cambridge University Press, New York.

Mamdani, E. and S. Assilian (1975): *An experiment in linguistic synthesis with a fuzzy logic controller*, International Journal of Man-Machine Studies, 7: 1–13.

Mansinha, L., D. Smylie and D. Orphal (1971): *The displacement fields of inclined faults*, Bulletin of the Seismological Society of America, 61: 1433–1440.

Matthes, S. (1990): *Mineralogie*, Springer, Berlin.

Mautz, R. (2001): *Zur Lösung nichtlinearer Ausgleichungsprobleme bei der Bestimmung von Frequenzen in Zeitreihen*, Ph.D. thesis, Technische Universität Berlin.

McTigue, D. (1987): *Elastic stress and deformation near a finite spherical magma body: Resolution of the point source paradox*, Journal of Geophysical Research, 92: 12931–12940.

Mets, C. D., R. Gordon, D. Argus and S.Stein (1990): *Current plate motions*, Geophysical Journal International, 101: 425–478.

Michalewicz, Z. (1992): *Genetic Algorithms+Data Structure=Evolution Programs*, Springer, New York, NY.

Mitchell, M. (1996): *An Introduction to Genetic Algorithms*, MIT Press, Cambridge, Massachusetts, London, England.

Mogi, K. (1958): *Relations of eruptions of various volcanoes and the deformation of the ground surface around them*, Bull Earthquake Res. Inst., Tokyo Univ., 36: 99–134.

Moon, W. and P. An (2003): *Geophysical application of artificial neural networks and fuzzy logic*, chap. D, 269–286, Kluwer academic publishers.

Müller, A. (2000a): *3-D modeling of the conductivity structure of Merapi volcano (Central Java) from magnetotellurics*, Tech. rep., Geoforschungszentrum, Potsdam, Germany.

Müller, A. (2000b): *Identification of good electric conductors below Merapi volcano (Central Java) by magnetotellurics*, Deutsche Geophysikalische Gesellschaft e.V., Addendum to Sonderband, IV/2000.

Müller, A. and V. Haak (2004): *3-D modeling of the deep electrical conductivity of Merapi volcano (Central Java): Integrating magnetotellurics, induction vectors and the effects of steep topography*, Journal of Volcanology and Geothermal Research, 138(3-4): 205–222.

Müller, M., A. Hördt and F. Neubauer (2002): *Internal structure of Mount Merapi, Indonesia, derived from long-offset transient electromagnetic data*, Journal of Geophysical Research, 107(B9): 2187, eCV 2-1-ECV 2-14.

Nelder, J. A. and R. Mead (1965): *A simplex method for function minimization*, Computer Journal, 7: 308–313.

Newhall, C., S. Bronto, B. Alloway, N. Banks, I. Bahar and M. Marmol (2000): *10000 years of explosive eruptions of Merapi volcano, Central Java: Archaeological and modern implications*, Journal of Volcanological and Geothermal Research, 100: 9–50.

Ohrnberger, M., J. Wassermann, E. Budi and J. Gössler (2000): *Continous autiomatic monitoring of Mt. Merapi's seismicity*, 2. Merapi-Galeras Workshop 1999, Deutsche Geophysikalische Gesellschaft, 4/2000: 103–108.

Osidele, O. (2001): *Reachable futures, structural change, and the practical credibility of environmental simulation models*, Ph.D. thesis, University of Georgia, Athens.

Pelzer, H. (1985): *Geodätische Netze in der Landes- und Ingenieurvermessung*, 527–558, Konrad Wittwer Verlag, Stuttgart.

Press, W., S. Teukolsky, W. Vetterling and B. Flannery (2002): *Numerical Recipes in C: The Art of Scientific Computing*, Cambridge University Press, Cambridge.

Price, K. (1999): *New ideas in optimization*, chap. 6, 79–108, The McGraw-Hill Ltd., Maidenhead, UK.

Ramilien, G. (2001): *Genetic algorithms for geophysical parameter inversion from altimeter data*, Geophysical Journal International, 147: 393–402.

Ratdomopurbo, A. and G. Poupinet (1995): *Monitoring a temporal change of seismic velocity in a volcano: Application to the 1992 eruption of Mt. Merapi (Indonesia)*, Geophysical Research Letters, 22: 775–778.

Ratdomopurbo, A. and G. Poupinet (2000): *An overview of the seismicity of Merapi volcano (Java, Indonesia) 1983 - 1994*, Journal of Volcanology and Geothermal Research, 100: 193–214.

Ratto, M., S. Tarantola and A. Saltelli (2001): *Sensitivity analysis in model calibration: GSA-GLUE approach*, Computer Physics Communications, 136: 212–224.

Rebscher, D., M. Westerhaus, A. Körner, W. Welle, Subandriyo, A. Brodscholl, H.-J. Kmpel and J. Zschau (2000): *Indonesian - German multiparameter stations at Merapi volcano*, Decade-Volcanoes under Investigation, Dt. Geophys. Gesellschaft, IV/2000: 93–102.

Ritter, O., A. Hoffmann-Rothe, A. Müller, S. Dwipa, E. Arsadi, A. Mahfi, I. Nurnusanto, S. Byrdina, F. Echternacht and V. Haak (1998): *A magnetotelluric profile across Central Java, Indonesia*, Geophysical Research Letters, 25: 4265–4268.

Rundle, J. (1980): *Static elastic-gravitational deformation of a layered half-space by point couple sources*, Journal of Geophysical Research, 85: 5355–5363.

Rundle, J. (1982): *Deformation, gravity, and potential changes due to volcanic loading of the crust*, Journal of Geophysical Research, 88(10): 647–652.

Ryan, M. (1987): *Elasticity and contractancy of Hawaiian Olivine tholeiite and its role in the stability and structural evolution of subcaldera magma reservoirs and rift systems*, chap. US Geological Survey Professional Paper 1350, Volcanism in Hawaii, 1395–1447, Washington DC, US Government Printing Office.

Rymer, H. (1994): *Microgravity changes as a precurssor to volcanic activity*, Journal of Volcanology and Geothermal Research, 61: 311–328.

Saltelli, A., K. Chan and E. Scott (Eds.) (2000): *Sensitivity Analysis*, John Wiley and Sons, LTD, Chichester, New York, Weinheim, Brisbane, Singapore, Toronto.

Saltelli, A., S. Tarantola, F. Campolongo and M. Ratto (2004): *Sensitivity Analysis in Practice*, John Wiley & Sons, Ltd, Chichester, New York, Weinheim, Brisbane, Singapore, Toronto.

Schwarzkopf, L., H. Schmincke and S. Cronin (2005): *A conceptual model for block and ash flow basal avalanche transport and deposition, based on deposit architecture of 1994 and 1998 Merapi flows*, Journal of Volcanology and Geothermal Research, 139: 117–134.

Schwieger, V. (2004): *Variance-based sensitivity analysis for model evaluation in engineering survey*, INGEO 2004 and FIG Regional Central and Eastern European Conference on Engineering Surveying Bratislava, Slovakia, November 11-13, 2004.

Setiawan, A. (2002): *Modeling of gravity changes on Merapi volcano observed between 1997 - 2000*, Ph.D. thesis, Darmstadt University of Technology, Germany.

Sigurdsson, H. (Ed.) (2000): *Encyclopedia of Volcanoes*, Academic Press, San Diego San Francisco New York Boston London Sydney Tokyo.

Simkin, T. and L. Siebert (1994): *Volcanoes of the World*, Geoscience Press, Tucson, Arizona.

Sobol', I. (1993): *Sensitivity analysis for non linear mathematical models*, Math. Model. Comput. Exp., 1: 407–414.

Takagi, H. and M. Sugeno (1985): *Fuzzy identification of systems and its applications to modeling and control*, IEEE Transactions on System, Man, and Cybernetics, 15(1): 116–132.

Tarantola, A. (1987): *Inverse Problem Theory*, Elsevier Amsterdam-Oxford-New York-Tokyo.

Tiampo, K., J. Fernández, G. Jentzsch, M. Charco, J.B. and Rundle (2004a): *Inverting for the parameters of a volcanic source using a genetic algorithm and a model for magmatic intrusion in elastic-gravitational layered earth models*, Computers & Geosciences, 30(9-10): 985–1001.

Tiampo, K., J. Fernández, G. Jentzsch, M. Charco and J. Rundle (2004b): *New results at Mayon, Philippines, from a joint inversion of gravity and deformation measurements*, Pure and Applied Geophysiks (in press), 161(7).

Tiampo, K., J. Rundle, J. Fernández and J. Langbein (2000): *Spherical and ellipsoidal volcanic sources at Long Valley Caldera, California, using a genetic algorithm inversion technique*, Journal of Volcanology and Geothermal Research, 102: 189–206.

Tiede, C., A. Camacho, C. Gerstenecker, J. Fernández and I. Suyanto (2005a): *Modelling the crust at Merapi volcano area, Indonesia, via the inverse gravimetric problem*, submitted to Geochemistry, Geophysics, Geosystems (G3).

Tiede, C., K. Tiampo, J. Fernández and C. Gerstenecker (2004): *Initial inversion results for elastic gravitational modeling via genetic algorithms at Merapi volcano, Indonesia*, submitted to Journal of Volcanology and Geothermal Research.

Tiede, C., K. Tiampo, J. Fernández and C. Gerstenecker (2005b): *Deeper understanding of non-linear geodetic data inversion using a quantitative sensitivity analysis*, Nonlinear Processes in Geophysics, 12: 373–379.

Tiede, C., K. Tiampo and C. Gerstenecker (2005c): *Fuzzy logic model for the determination of physical reliability of volcanic sources*, submitted to Computational Geosciences.

UNTUNG, M. and Y. SATO (1978): *Gravity and Geological Studies in Jawa, Indonesia*, Geological Survey of Indonesia and Geological Survey of Japan.

VOIGHT, B., E. CONSTANTINE, S. SISWOWIDJOYO and R. TORLEY (2000): *Historical eruptions of Merapi volcano, Central Java, Indonesia, 1768-1998*, Journal of Volcanology and Geothermal Research, 100: 69–138.

VOSE, M. (1999): *The Simple Genetic Algorithm-Foundation and Theory*, MIT Press Cambridge, Massachusetts, London, England.

WANG, T. (2001): *Global optimization for constrained nonlinear programming*, Ph.D. thesis, University of Illinois.

WEGLER, U. and B.-G. LÜHR (2001): *Scattering behaviour at Merapi volcano (Java) revealed from an active seismic experiment*, Geophysical Journal International, 145: 579–592.

WELSCH, W. (Ed.) (1983): *Deformationsanalysen '83*, Schriftenreihe, Hochschule der Bundeswehr München.

YAGER, R. and D. FILEV (1994): *Essentials of Fuzzy Modeling and Control*, John Wiley-Interscience New York, NY, USA.

ZADEH, L. (1965): *Fuzzy sets*, Information and Control, 8: 335–353.

ZIMMER, M. and J. ERZINGER (2003): *Continous* H_2O*,* CO_2*,*^{222}Rn *and temperature measurements on Merapi volcano, Indonesia*, Journal of Geophysical Research, 125: 25–38.

ZSCHAU, J., R. SUKHYAR, M. PURBAWINATA, B. LÜHR and M. WESTERHAUS (1998): *Project MERAPI - Interdisciplinary research at a high-risk volcano in Decade Volcanoes under Investigation*, Dt. Geophys. Gesellschaft, 3: 3–8, edited by J. Zschau and M.Westerhaus Dt. Geophys. Gesellschaft.

Curriculum Vitae

Surname: Tiede
Given Names: Carola
Place of Birth: Bad Hersfeld
Date of Birth: June 1st, 1974

Educational Institutions Attended

1981-1985	Primary school, Bad Hersfeld
1985-1991	Comprehensive school Obersberg, Bad Hersfeld
1991-1994	Comprehensive secondary school, Modellschule Obersberg, Bad Hersfeld
1994-1996	Education as surveying technician at land registry office (Katasteramt), Bad Hersfeld
1996-2001	Study of Geodesy, Darmstadt University of Technology

Degrees Awarded

1994	General qualification for university entrance (Allgemeine Hochschulreife)
1996	Surveying technician (Vermessungstechnikerin)
2001	Diplom-Ingenieur (Geodesy)

Professional work

1998-2000	work as student at Institute of Physical Geodesy, Darmstadt University of Technology
2001-2002	research assistant at Institute of Flight Systems and Control, Darmstadt University of Technology
since 2002	research assistant at Institute of Physical Geodesy, Darmstadt University of Technology. Coorporation and research stay with Prof. Dr. Kristy Tiampo, University of Western Ontario and Prof. Dr. Jose Fernandez, University of Mathematicas and Sciences, Madrid.